

University of Nebraska - Lincoln

DigitalCommons@University of Nebraska - Lincoln

---

Theses, Dissertations, and Student Research:  
Department of Physics and Astronomy

Physics and Astronomy, Department of

---

11-2009

## Finite temperature effects in magnetic materials: Model and ab initio studies

Aleksander L. Wysocki

University of Nebraska-Lincoln, awysocki@iastate.edu

Follow this and additional works at: <https://digitalcommons.unl.edu/physicsdiss>



Part of the [Condensed Matter Physics Commons](#)

---

Wysocki, Aleksander L., "Finite temperature effects in magnetic materials: Model and ab initio studies" (2009). *Theses, Dissertations, and Student Research: Department of Physics and Astronomy*. 8. <https://digitalcommons.unl.edu/physicsdiss/8>

This Article is brought to you for free and open access by the Physics and Astronomy, Department of at DigitalCommons@University of Nebraska - Lincoln. It has been accepted for inclusion in Theses, Dissertations, and Student Research: Department of Physics and Astronomy by an authorized administrator of DigitalCommons@University of Nebraska - Lincoln.

FINITE TEMPERATURE EFFECTS IN MAGNETIC MATERIALS: MODEL  
AND *AB INITIO* STUDIES

by

Aleksander L. Wysocki

A DISSERTATION

Presented to the Faculty of  
The Graduate College at the University of Nebraska  
In Partial Fulfillment of Requirements  
For the Degree of Doctor of Philosophy

Major: Physics and Astronomy

Under the Supervision of Professor Kirill Belashchenko

Lincoln, Nebraska

November, 2009

FINITE TEMPERATURE EFFECTS IN MAGNETIC MATERIALS: MODEL  
AND *AB INITIO* STUDIES

Aleksander L. Wysocki, Ph.D

University of Nebraska, 2009

Advisor: Kirill Belashchenko

The understanding of finite temperature behavior of magnetic materials is of vital importance for spintronic applications. In this dissertation different theoretical techniques for studying magnetic thermodynamics of various materials are discussed.

$\text{Cr}_2\text{O}_3$  is an antiferromagnetic insulator that was proposed to be a key component of new spintronic devices. The magnetic properties of  $\text{Cr}_2\text{O}_3$  were studied using the LDA+U method. Magnetism was found to be very well described by the Heisenberg model. Subsequently, magnetic thermodynamics was explored using quantum pair cluster approximation. Overall, very good agreement with experiment was found for the ground state and thermodynamics properties.

The magnetism at the (0001) surface of  $\text{Cr}_2\text{O}_3$  was investigated using first principles. The description of magnetic properties required a detailed knowledge of the surface structure that was found to be very nontrivial. In particular, an order-disorder structural phase transition was shown to exist at the surface. In addition, the existence of the reentrant phase transition due to a magneto-structural coupling was hypothesized. The magnetic properties of the  $\text{Cr}_2\text{O}_3$  (0001) surface were found to be very unique; an uncompensated magnetic moment exists at the surface and persists even with surface roughness. The finite temperature behavior of this surface magnetism was studied using the Heisenberg model and the mean-field approximation. The surface magnetization was found to exist up to almost room temperature. This

effect makes  $\text{Cr}_2\text{O}_3$  a very promising material for exchange bias applications.

In itinerant magnets both transverse and longitudinal spin fluctuations are very important for thermodynamics. A classical model containing both types of fluctuations was introduced with a single parameter controlling the degree of itinerancy, i.e., relative importance of longitudinal and transverse spin fluctuations. The thermodynamics was studied using the Monte Carlo method, mean-field approximation, and Onsager method. In general, magnetic short-range order was found to be weak even for strongly itinerant systems and Monte Carlo was in a good agreement with mean-field approximation. The Onsager cavity field method was extended to models with longitudinal spin fluctuations and was shown to be in excellent agreement with Monte Carlo. The ambiguity of the choice of the phase space measure for longitudinal spin fluctuations for classical models was emphasized.

In magnetic metals the resistivity has an additional contribution due to scattering on the thermally induced spin fluctuations. This spin-disorder resistivity was studied from first principles for Fe and Ni. Various models of thermal spin disorder were considered, including the mean-field approximation and the nearest-neighbor Heisenberg model. In general, spin-disorder resistivity was found to depend very weakly on magnetic short-range order. For local moments frozen to their zero-temperature values, a good agreement with experiment was obtained for Fe, but for Ni the resistivity at elevated temperatures was significantly overestimated. This overestimation of spin-disorder resistivity for Ni was attributed to the reduction of the local moment due to longitudinal spin fluctuations.

## ACKNOWLEDGEMENTS

There are many people I would like to thank for their support and guidance throughout my doctoral studies.

First and foremost, I would like to express my sincere gratitude to my supervisor Prof. Kirill Belashchenko. I have been extremely lucky to have such a knowledgeable and hands-on advisor. I would like to thank you Kirill for giving me an opportunity to be a graduate student of such an excellent scientist. I am grateful to you for all the time you spent explaining me various aspects of physics. During our long discussions you have introduced to really beautiful physics and showed me how scientist should think. I really appreciate your interest in my scientific development and your care about my future career. Your guidance made my graduate experience worthwhile and productive.

I would like to thank Professor Evgeny Tsymbal, Professor Peter Dowben, and Professor Xiao Cheng Zeng for serving on my supervisory committee. I am grateful to them for their careful and critical reading of this dissertation. Specifically, I would like to thank Professor Evgeny Tsymbal for many insightful comments he made to the work presented in this dissertation during our group meetings and for his continued support during my Ph. D. studies. I am indebted to Professor Renat Sabirianov from University of Nebraska-Omaha for many helpful discussions and for collaborating with me on the work presented in Chapter 5. In particular, I would like to thank Renat for helping me with the Monte Carlo simulations. I would also like to thank Professor Mark van Schilfhaarde from Arizona State University for help with his LMTO code and for collaborating with me on the work presented in Chapter 5. I am very grateful to Professor Siqi Shi from Zhejiang Sci-Tech University for many interesting discussions we had during his stay as a postdoc with Kirill as well as for collaborating with me on the work presented in Chapters 2 and 3. I would also like to thank Professor Julian Velez from University of Puerto Rico for introducing me to the VASP code and for collaborating with me on the work presented in Chapter 5. I would like to thank Mr. James Glasbrenner for collaborating with me on the work presented in Chapter 4 and for many interesting discussions we had. I would like to thank Dr. J. D. Burton for a help he provided to me during my doctoral studies. A lot of calculations presented in this work were performed using the Research Computing Facility of the University of Nebraska-Lincoln. I would like thank the staff there for an excellent support I received from them.

Finally, I would like to thank my wife for giving me a new life. *Karolina, nigdy nie zapomnę, że wyzwoliłaś mnie z mroku. Kocham cię moja czarodziejko.* I owe a special debt to my amazing son for providing me so important motivation for writing this dissertation. I love you Karol, I am looking forward to see you. I am also very grateful to my parents and parents-in-law for their great support during my doctoral studies.

To Karolina, the most beautiful and intelligent woman in the world and to my son  
Karol, the most energetic and lovable baby.

# Contents

<b>1</b>	<b>Introduction</b>	<b>13</b>
1.1	Finite temperature magnetism . . . . .	14
1.2	Monte Carlo . . . . .	18
1.3	<i>Ab initio</i> methods . . . . .	24
1.3.1	Density functional theory . . . . .	24
1.3.2	Solving Kohn-Sham equation . . . . .	28
1.3.3	Tight-binding linear muffin-tin orbitals . . . . .	29
	<b>Bibliography</b>	<b>31</b>
<b>2</b>	<b>Magnetism of Cr<sub>2</sub>O<sub>3</sub></b>	<b>34</b>
2.1	Introduction . . . . .	34
2.2	Computational details . . . . .	35
2.3	Results and discussion . . . . .	37
2.3.1	Exchange parameters . . . . .	39
2.3.2	Mechanism of magnetic interaction . . . . .	41
2.3.3	Néel temperature . . . . .	43
2.4	Conclusion . . . . .	44
2.A	Appendix . . . . .	44
	<b>Bibliography</b>	<b>46</b>
<b>3</b>	<b>Magnetism and structural phase transitions at the Cr<sub>2</sub>O<sub>3</sub> (0001) surface</b>	<b>48</b>
3.1	Introduction . . . . .	48
3.2	Method . . . . .	50
3.3	Surface structure . . . . .	51
3.4	Structural surface thermodynamics . . . . .	55
3.5	Surface electronic structure . . . . .	63
3.6	Surface magnetism . . . . .	64
3.7	Conclusions . . . . .	68
	<b>Bibliography</b>	<b>70</b>

<b>4</b>	<b>Thermodynamics of itinerant magnets in a classical spin fluctuation model</b>	<b>72</b>
4.1	Introduction . . . . .	72
4.2	Model . . . . .	74
4.3	Thermodynamic properties: Monte Carlo and mean-field results . . . . .	76
4.4	Generalized Onsager correction for itinerant systems . . . . .	80
4.5	Conclusions . . . . .	83
	<b>Bibliography</b>	<b>85</b>
<b>5</b>	<b>First principles analysis of spin-disorder resistivity</b>	<b>87</b>
5.1	Introduction . . . . .	87
5.2	General approach and methods . . . . .	89
5.3	The spin-disorder resistivity in the mean-field approximation . . . . .	90
5.3.1	The paramagnetic state . . . . .	90
5.3.2	The temperature dependence in the ferromagnetic state . . . . .	93
5.4	Effect of magnetic short-range order . . . . .	98
5.5	The effect of the local moment reduction . . . . .	102
5.6	Discussion and conclusions . . . . .	103
	<b>Bibliography</b>	<b>105</b>
	<b>Publications</b>	<b>108</b>

# List of Figures

2.1	Rhombohedral primitive cell of $\text{Cr}_2\text{O}_3$ (left) together with the hexagonal unit cell (right). Smaller gray spheres represent Cr atoms; larger red spheres display the O atoms. . . . .	37
2.2	Atomic volume (a), magnetic moment (b), band gap (c) and Néel temperature (d) as functions of the Coulomb $U$ parameter for the antiferromagnetic $+ - + -$ state. The value of $J$ is fixed at 0.58 eV. The horizontal lines denote experimental values; those in panel (b) are from both Refs. [22, 23]. . . . .	38
2.3	Orbital projected DOS for the antiferromagnetic $+ - + -$ ground state of bulk $\text{Cr}_2\text{O}_3$ , calculated within the LDA+U with $U = 4.0$ eV, $J = 0.58$ eV. (a) O-2p, (b) Cr- $e_g$ and (c) Cr- $t_{2g}$ . Majority and minority-spin DOS are plotted with different signs. . . . .	39
3.1	Bulk crystal structure of $\text{Cr}_2\text{O}_3$ . (a) Hexagonal unit cell. Gray and red spheres represent Cr and O ions, respectively. (b) Schematic sideview of the crystal structure along (0001) direction. Full and empty circles denote occupied and empty octahedral sites in the Cr double layer, respectively. . . . .	51
3.2	Slab geometries for four considered surface models with $(1 \times 1)$ structure. Gray and red spheres represent Cr and O atoms, respectively. . . . .	52
3.3	Different orderings of surface Cr. . . . .	54
3.4	The energy profile for hopping of surface Cr atom between site A and B along (0001) for AAB model. . . . .	56
3.5	The ground state phase diagram of the two-exchange model. Adapted from Refs. [33, 34]. . . . .	59
3.6	The phase diagram for the electrostatic model. The red line shows the reduced transition temperature ( $t_c = \frac{k_B T_C}{ J_1 }$ ) of the phase transition from the AAB ordering to the disordered structure for the electrostatic model as a function of $\alpha$ . The patterned rectangular shows schematically the values of $\alpha$ found by fitting. The dashed line shows schematically the boundary between AB structure and disordered state. . . . .	62

3.7	DOS for Cr $d$ states for $U = 3.5$ eV. (a) for surface Cr ion at position A, (b) for surface Cr ion at position B, (c) for bulk-like Cr ion in the middle of the slab. Majority and minority-spin DOS are plotted with different signs. . . . .	63
3.8	The comparison of magnetic structures of the (0001) surface of $\text{Cr}_2\text{O}_3$ and surfaces of most antiferromagnets. Full and empty back circles denote magnetic ions with spin up and down, respectively. . . . .	64
3.9	Reduced surface magnetization as a function of temperature for AAB surface model. Total magnetization (solid black line) and magnetizations of site A (solid blue line) and B (solid red line) are shown. In addition the bulk sublattice magnetization is plotted (dashed black line). . . . .	67
4.1	(a-b) Reduced magnetization $\langle x_z \rangle$ , (c-d) mean squared local moment $\langle x^2 \rangle$ , and (e-f) inverse paramagnetic susceptibility $\chi^{-1}$ as a function of the reduced temperature $t = T/(J_0 m_0^2)$ . Mean-field approximation with $g(x) = 1$ (solid blue (grey) lines) or with $g(x) = x^{-2}$ (dashed black lines), Monte Carlo with $g(x) = 1$ (black circles, filled for fcc and empty for bcc lattice), Monte Carlo with $g(x) = x^{-2}$ (red (grey) squares, filled for fcc and empty for bcc lattice). The inset in panel (e) highlights the region close to $t_c$ for the bcc lattice with $g(x) = 1$ and also shows the results of the generalized Onsager method (black line connecting the Monte Carlo points). . . . .	77
4.2	(a) Reduced Curie temperature $t_c$ and (b) magnetic short-range order parameter $\langle \cos \theta_{nn} \rangle$ at $T = 1.1T_c$ as a function of the itinerancy parameter $\alpha$ for the bcc lattice. Solid black line, red (grey) squares, and blue (grey) circles denote mean-field approximation, Monte Carlo, and the generalized Onsager method for $g(x) = 1$ , respectively. Dashed black line and empty black squares denote mean-field approximation and Monte Carlo for $g(x) = x^{-2}$ . Green (grey) triangles show the results of the incomplete Onsager reaction field correction with the on-site interaction left unrenormalized. The blue (grey) dash-dotted line in the upper panel: effective moment $x_{\text{eff}}^2$ found from the Curie constant for $g(x) = 1$ in mean-field approximation. Very similar results were obtained for the fcc lattice (not shown). . . . .	79
5.1	The schematic picture of the system used in the calculations. Vertical lines indicate the embedding planes. . . . .	90

5.2	The area-resistance product $AR$ of the FM(O)/FM(D)/FM(O) systems as a function of the FM(D) layer thickness for bcc Fe (black filled symbols) and fcc Ni (red empty symbols) obtained with $l_{max} = 2$ . Circles and squares correspond, respectively, to the paramagnetic state and to the lowest temperature for which the calculations were made ( $T = 0.27T_c$ for Fe and $T = 0.58T_c$ for Ni). $4 \times 4$ and $3 \times 3$ supercells were used for Fe and Ni, respectively, with edges along the $[100]$ directions. Straight lines show the linear fitting; error bars are smaller than the size of the symbols. . . . .	91
5.3	Distribution of the local magnetic moment in self-consistent fully spin-disordered bcc Fe. The Fermi temperature is equal to the experimental $T_c$ . The vertical line shows the local moment at $T = 0$ . The red (solid) curve shows the Gaussian fit to the data. . . . .	93
5.4	Spin-resolved density of states (solid lines) for bcc Fe averaged over random spin configurations with the mean-field distribution function (5.1); (a) $T = 0$ , (b) $T = 0.25T_c$ , (c) $T = 0.5T_c$ , (d) $T = 0.75T_c$ , and (e) $T = T_c$ . Dashed lines show the mean-square deviation of the DOS on a given site from its ensemble average. . . . .	94
5.5	Same as in Fig. 5.4 but for fcc Ni. . . . .	95
5.6	Dependence of spin-disorder resistivity on the magnetization for (a) Fe, and (b) Ni. Black circles denote experimental data combining Ref. [4] for $\rho_{mag}(T)$ and Ref. [40] for $M(T)$ . Blue squares show mean-field calculations, filled red triangles denote Monte Carlo results, and green diamonds show reverse Monte Carlo calculations. The empty red triangles show Monte Carlo results with larger cells: $6 \times 6$ for Fe and $4 \times 4$ for Ni. The upper axis shows temperatures corresponding to the given magnetization in mean-field approximation. The error bars a show statistical uncertainties where they exceed the size of the symbols. All results are for $l_{max} = 2$ . . . . .	96

# List of Tables

2.1	The exchange parameters $J_n$ fitted using the total energies of 12 magnetic configurations calculated for different values of $U$ with $J$ fixed at 0.58 eV. Each pair of sites contributes $J_{ij}\mathbf{e}_i\mathbf{e}_j$ to the total energy, where $\mathbf{e}_i$ is the unit vector parallel to the direction of the local moment at site $i$ . The last column $\Delta$ shows the mean-square misfit in the fitting of the total energy. $J_n$ and $\Delta$ are given in meV. . . . .	40
2.2	Energies of three simple magnetic configurations relative to the ground $+ - + -$ state (in meV per formula unit) as a function of the fictitious external potential $V$ applied to the oxygen $p$ orbitals (in eV). Reduced values of $U$ on Cr compensate for the increased band gap (see text for details). $\Delta$ is the distance from the oxygen band top to CBM in eV. .	43
3.1	Ground state and paramagnetic surface energies for different surface models. . . . .	53
3.2	Surface relaxation for surface models A and B. The relaxations for first seven atomic layers are given in % of the bulk interlayer distances. $M(n)$ denotes $n$ th layer from the surface with M being the type of atom in the layer. . . . .	54
3.3	Parameters for the two-exchange model obtained from the ground state paramagnetic surface energies. $\Delta$ is the mean-square misfit of the fitting. The estimate of the transition temperature for order-disorder transition is also given. . . . .	57
3.4	Parameters for the electrostatic model obtained from the ground state and paramagnetic surface energies. $\Delta$ is the mean-square misfit of the fitting. The estimate of the transition temperature for order-disorder transition is also given. . . . .	58
3.5	Magnetic moment per Cr atom for three closest the surface atomic layers of Cr for different surface models. $M(n)$ denotes $n$ th layer from the surface with M being the type of atom in the layer. The unit is $\mu_B$	65
3.6	Parameters of the Heisenberg Hamiltonian for models A and B. $\Delta$ is the mean-square misfit of the fitting. The last column shows corresponding parameters obtained from the values of the bulk exchange constants $J_i^b$ (see Section 2.3). The units are eV. . . . .	66

3.7	Parameters of the Heisenberg Hamiltonian for AAB model obtained from fitting to magnetic surface energies and from parameters of models A and B. The units are eV. . . . .	68
4.1	Reduced Curie temperature $t_c$ for bcc and fcc lattices for phase space measure with $g(x) = 1$ : Results of the mean-field approximation (MFA), Horwitz-Callen approximation (HC), generalized Onsager method (GO) and Monte Carlo (MC). . . . .	82
5.1	Spin-disorder resistivity in $\mu\Omega\cdot\text{cm}$ for paramagnetic bcc Fe and fcc Ni. The calculated values are given for basis sets with $l_{max} = 2$ and 3, as well as for different lateral cell sizes with edges along the [100] directions. SC denotes calculations with self-consistent potentials. Standard deviations of spin-disorder resistivity due to limited disorder sampling are included. . . . .	92
5.2	Spin-spin correlators $C_{0i}$ for the first three shells of nearest neighbors ( $i = 1, 2, 3$ ), the local correlator ( $i = 0$ ), and the effective temperature are shown for Fe and Ni for each considered temperature in Monte Carlo (MC) simulations and for reverse Monte Carlo (RMC) method. The values of spin-disorder resistivity are compared with mean-field approximation (MFA) results corresponding to the same $M^2$ . The listed uncertainties are due to the limited disorder sampling. . . . .	99
5.3	Spin-disorder resistivity in $\mu\Omega\cdot\text{cm}$ for paramagnetic Ni as a function of the fixed local moment. $2 \times 2$ supercells and basis sets with $l_{max} = 2$ and $l_{max} = 3$ were used. Standard deviations of spin-disorder resistivity due to limited disorder sampling are included. . . . .	103

# Chapter 1

## Introduction

Magnetic materials have been a subject of conspicuous interest and intensive research in the history of science. For one, this is due to tremendous challenge the description of magnetism has posed to theoretical physics. Secondly, the interest in magnetic systems has been recently boosted by the invention of the concept of spintronics. This new technology hopes to exploit the spin of the electron and the associated magnetic moment, in addition to its charge. Consequently, magnetic materials are key components of spintronic device architectures. Since these devices must work at or even above room temperature, the understanding of magnetic thermodynamics is crucial. However, the general description of the finite temperature magnetism is an extremely complex problem whose solution is still not complete. In fact, besides the existence of many models and techniques for description of magnetic thermodynamics, their applicability to particular magnetic systems is often not clear.

In this dissertation the behavior of different magnetic materials, particularly  $\text{Cr}_2\text{O}_3$ , at finite temperatures is studied. In Chapter 1, the basic background on finite temperature magnetism is provided and computational methods used in subsequent chapters are described. In Chapter 2, we use *ab initio* methods to investigate bulk  $\text{Cr}_2\text{O}_3$  with particular emphasis on its magnetism. We obtain a very good description of the magnetic thermodynamics which is in excellent agreement with experiment. In Chapter 3, we explore the (0001) surface of  $\text{Cr}_2\text{O}_3$  which has a very unusual property of having a surface magnetization that is stable against roughness. The finite temperature description of this surface magnetism is complicated due to nontrivial surface structure and existence of structural surface phase transitions. In fact, we found that the coupling between magnetism and structure is responsible for unusual features of these phase transitions. In Chapter 4, we study the thermodynamics of itinerant magnets by introducing a simple classical model with one parameter that characterizes the degree of itinerancy. We found that longitudinal spin fluctuations are of great importance in the finite temperature description of itinerant magnets. Nevertheless, the magnetic short-range order is always weak and the mean-field approximations works well. We also derive the generalization of the Onsager method to the itinerant magnets. Finally, in Chapter 5, we investigate the spin disorder resistiv-

ity of Fe and Ni using first principles electronic structure calculations. We show that if magnetic moments in the disordered state are kept to its zero temperature values, a very good agreement with experiment is obtained for Fe but for Ni the resistivity at elevated temperature is strongly overestimated. This overestimation is attributed to the significant reduction of local moment in the disordered Ni. We also find that magnetic short range order has a very mild effect on spin disorder resistivity.

## 1.1 Finite temperature magnetism

The modern theory of magnetism started with the concept of an atomic local magnetic moment. For a set of classical magnetic moments with a fixed magnitude  $\mu$  under external magnetic field  $H$  the magnetization (total magnetic moment per site) at temperature  $T$  is given by [1]

$$m = \mu L(x) \quad x = \frac{\mu H}{k_B T} \quad (1.1)$$

where  $L(x) = \coth(x) - \frac{1}{x}$  is the Langevin function. This model explains the observed Curie law for magnetic susceptibility of paramagnetic substances

$$\chi \equiv \left( \frac{dm}{dH} \right)_{H=0} = \frac{C}{T} \quad (1.2)$$

where  $C = \frac{\mu^2}{3k_B}$  is called Curie constant. Subsequently, Weiss [2] assumed that in ferromagnetic materials there is an interaction between atomic magnetic moments and approximated its effect by a mean molecular field proportional to the magnetization,  $H_W = \Gamma m$ . Adding this molecular field to the external field in Equation (1.1) we obtain

$$m = \mu L(y) \quad y = \frac{\mu(H + \Gamma m)}{k_B T} \quad (1.3)$$

It follows from Equation (1.3) that for temperatures below the Curie temperature  $T_C = \frac{\mu^2 \Gamma}{3k_B}$  there is a spontaneous magnetization even for zero magnetic field and above  $T_C$  the susceptibility follows the Curie-Weiss law

$$\chi = \frac{C}{T - T_C} \quad (1.4)$$

where  $C$  is the same Curie constant as in Equation (1.2). A similar theory can be also formulated for antiferromagnetic or ferrimagnetic materials (see for example Ref. [3]).

While the above phenomenological Langevin-Weiss theory has quite successfully explained the essential properties of magnetic materials, it cannot be justified by the classical theory of physics. In particular, it is difficult to justify the existence of atomic

local magnetic moments. On the contrary, there is the Bohr van Leeuwen theorem that showed that magnetism is not consistent with classical statistics [4]. Moreover, the classical physics has not been able to explain the nature of the Weiss molecular field. The magnetic dipole-dipole interaction gives the value of  $\Gamma$  which is about two or three orders of magnitude smaller than estimated from the observed values of  $T_C$ . Both these problems were resolved with the advent of quantum mechanics and are discussed below.

According to quantum mechanics electrons in atoms have quantized orbital and spin angular momenta  $\hbar\mathbf{l}$  and  $\hbar\mathbf{s}$ , and the associated magnetic moment  $(\mathbf{l} + 2\mathbf{s})\mu_B$ . The total angular momentum of an atom  $\mathbf{J}$  is a sum of the total orbital angular momentum  $\mathbf{L} = \sum_i \mathbf{l}_i$  and the total spin  $\mathbf{S} = \sum_i \mathbf{s}_i$ . Except for some heavy atoms, the Russell-Saunders scheme is valid and the eigenstates are specified by the quantum numbers  $S$ ,  $L$ , and  $J$ . The relative energies of the eigenstates satisfy Hund's rules, i.e., the lowest energy have the states with the largest  $S$  and among them the state with the largest  $L$  has the lowest energy. This lowest energy state has a degeneracy since  $J$  can take integral or half odd integral values between  $L + S$  and  $|L - S|$ . This degeneracy is lifted by spin orbit coupling  $\lambda\mathbf{L} \cdot \mathbf{S}$  where the coupling constant  $\lambda$  is positive when a given shell is less than half occupied and is negative when it is more than half occupied. Finally, each state with a given  $J$  has a  $(2J + 1)$ -fold degeneracy that can be lifted by an external magnetic field.

When the lowest energy state with given  $S$ ,  $L$ , and  $J$  is well separated from other states, i.e., the energy separation is much larger than  $k_B T$ , we can regard the atom as having a fixed magnitude magnetic moment  $\mu = g_J \mu_B \mathbf{J}$  where  $g_J = 1 + \frac{J(J+1) + S(S+1) - L(L+1)}{2J(J+1)}$  is the Lande  $g$ -factor. The paramagnetic response of a system of atoms can be therefore evaluated by generalizing Equation (1.1) to the case of discrete spectrum

$$m = g_J \mu_B J B_J(x) \quad x = \frac{g_J \mu_B J H}{k_B T} \quad (1.5)$$

where  $B_J(x) = (1 + \frac{1}{2}J) \coth(1 + \frac{1}{2}J)x - \frac{1}{2}J \coth(\frac{x}{2J})$  is the Brillouin function that reduces to the Langevin function in the classical limit  $J \rightarrow \infty$ . The susceptibility is still given by Equation (1.2) with  $C = \frac{g_J^2 \mu_B^2 J(J+1)}{3k_B T}$ .

When atoms form a solid the situation becomes more complicated since electronic states may significantly differ from atomic orbitals. Only in the case of ionic insulators and the  $f$  states of rare-earth metals the description in terms of atomic orbitals remains valid<sup>1</sup>. Still however, the crystal field may lead to the splitting of atomic shells into subshells. Moreover, for ionic compounds the charge transfer changes the occupation of atomic states. In particular, it may fill or empty originally partially occupied electronic shells or subshells destroying magnetic moment. The  $d$  and  $f$  shells or subshells however often remains partially filled and exhibit a local magnetic moment  $\mu = g\mu_B \mathbf{S}$ . This expression for the local magnetic moment emphasizes

---

<sup>1</sup>Only for empirical analysis; even in this case the atomic orbitals cannot be used for quantitative description.

the fact that the orbital angular momentum is usually quenched by the crystal field induced splitting and therefore magnetic moment is only associated with the total spin of the subshell (in this case  $g = 2$ ). Sometimes however, the orbital angular momentum is not totally quenched and in addition it can be partially restored by the spin-orbit coupling. In this case  $\mathbf{S}$  and  $g$  should be regarded as effective angular momentum and  $g$ -factor for a given shell or subshell.

Using the concept of the Weiss molecular field, the magnetization of a ferromagnet with atomic local moments is

$$m = g\mu_B S B_S(y); \quad y = \frac{g\mu_B S(H + \Gamma m)}{k_B T} \quad (1.6)$$

The spontaneous magnetization exist for temperatures below  $T_C = \frac{g^2\mu_B^2 S(S+1)\Gamma}{3k_B}$  and above  $T_C$  the susceptibility follows the Curie-Weiss law (1.4) with  $C = \frac{g^2\mu_B^2 S(S+1)}{3k_B T}$ . A similar formalism can be derived for antiferromagnetic and ferrimagnetic materials [3].

For solids with atomic magnetic moments the origin of the Weiss molecular field was attributed by Heisenberg [5] to the quantum-mechanical exchange interaction between neighboring atoms. Based on the Heitler-London model, Heisenberg expressed this interaction in terms of the spin or effective angular momentum operators

$$\hat{\mathcal{H}} = -\frac{1}{2} \sum_{i,j} J_{ij} \hat{\mathbf{S}}_i \cdot \hat{\mathbf{S}}_j \quad (1.7)$$

where  $i, j$  specify atomic sites in the crystal, and  $J_{ij}$  are the interatomic exchange constants. By applying the mean-field approximation to Hamiltonian (1.7) we can obtain the Weiss molecular field with  $\Gamma = (g\mu_B)^{-2} J_0$  where  $J_0 = \sum_{i,j} J_{ij}$ .

For magnetic insulators the exchange interaction is short ranged and its dominant mechanism is the kinetic exchange that involves hopping between neighboring atoms. We distinguish the direct kinetic exchange due to hopping between magnetic atoms and the indirect exchange, also called superexchange, involving hopping through non-magnetic atom, usually oxygen. In each case the sign of the exchange interaction can be easily found by analyzing the occupation of the atomic states and the geometry of the solid [6]. On the other hand, for the rare-earth metals the long-range indirect exchange interaction via conduction electrons dominates.

The exchange parameters can be calculated for specific materials from first principles. There are many available calculational schemes. The most straightforward method consists in total energy calculations for a set of collinear magnetic structures obtained by the reversal of directions of some magnetic moments and fitting them to Equation (1.7). Other techniques involve the spin spiral approach [7] and the method of Liechtenstein [8].

There are many magnetic metals, like  $3d$  transition metal magnets, for which the electronic states responsible for magnetism cannot be even qualitatively derived from

atomic orbitals and thus the concept of atomic magnetic moments is not adequate. These systems are called itinerant magnets. For itinerant magnets a completely different approach to magnetism based on the picture of electronic bands was proposed by Slater [9] and Stoner [10]. Consider a metal in the paramagnetic state, with the density of states (DOS) per spin  $N(E)$ , and analyze the stability of the system with respect to a small exchange splitting  $\Delta$  and the associated magnetization<sup>2</sup>,  $m = \Delta N(E_F)$  where  $E_F$  is the Fermi energy. The total energy of the system can be then written as

$$E_{tot}(m) = \frac{1}{2}\chi_P^{-1}m^2 - \frac{1}{4}Im^2 - Hm \quad (1.8)$$

The first term in the above equation represents the band energy and  $\chi_P = 2N(E_F)$  is the Pauli susceptibility; the second term describes the mean exchange interaction whose strength is described by the Stoner parameter  $I$ ; and the last term is due to the interaction with the external magnetic field  $H$ . Note that here  $H$  and  $I$  have units of energy and  $m$  is dimensionless. Minimizing Equation (1.8) with respect to  $m$  we can find the susceptibility of the system

$$\chi = \frac{\chi_P}{1 - IN(E_F)} \quad (1.9)$$

As seen, the exchange interaction enhances the noninteracting Pauli susceptibility by a factor  $(1 - IN(E_F))^{-1}$  and the system becomes unstable with respect to magnetization if the Stoner criterion is satisfied

$$IN(E_F) > 1 \quad (1.10)$$

The Stoner parameter is a quasi-atomic property with a very weak  $\mathbf{k}$ -vector dependence [12]. It was calculated from first principles for variety of materials [13, 14]. Using these values together with  $N(E_F)$  the Stoner model was very successful in prediction of magnetism in itinerant magnets.

The Stoner model can be also generalized to finite magnetizations which however requires a detailed knowledge of the band structure of a given material. Instead, one usually uses the spin polarized electronic structure methods that can be regarded as modern version of the Stoner theory. This approach not only provides correct values of ground state magnetic moment in magnetic metals [14] but is also able to describe the ground state of magnetic insulators.

While the Stoner theory gives usually an adequate description of the magnetic ground state, its straightforward generalization to finite temperatures fails miserably:  $T_C$  is too high by a factor of five, and there is no Curie-Weiss law above  $T_C$ , to mention but a few of its shortcomings. The reason is that this theory assumes that the magnetization in each unit cell points in the same direction and therefore the transverse spin fluctuations, that cause the direction of the magnetization to vary

---

<sup>2</sup>The Stoner model can be generalized to other than ferromagnetic orderings (see for example Ref. [11]).

from unit cell to unit cell, are neglected. Under these circumstances the magnetization can disappear only if the exchange splitting goes to zero. In most of magnets however the transverse spin fluctuations are of primary importance for magnetic thermodynamics since their excitation energy is much lower. For this reason the classical Heisenberg Hamiltonian (the spin operators in Equation (1.7) are replaced by classical unit vectors) is very often used as a phenomenological model for a finite temperature description of itinerant magnets. In fact, this approach in some cases, like for example in Fe, gives surprisingly good description of the magnetic thermodynamics. This unexpected agreement led to the idea that a local moment actually exists in itinerant magnets. Indeed, based on Anderson model [15] one may argue that the intra- and inter-atomic exchange can lead to creation of a well defined local magnetic moment in metals<sup>3</sup>. This local magnetic moment however doesn't have an origin in a atomic moment and consequently its magnitude is usually a noninteger multiple of  $\mu_B$ . Magnetic metals for which the inter-atomic exchange has a small contribution to formation of local moment are said to be close to the local moment limit since in this case the local moment can be regarded as almost fixed. Heisenberg model is then expected to provide a reasonable description of finite temperature properties. More general approach is based on adiabatic approximation [16] that involves the separation of fast and slow degrees of freedom corresponding to transverse and longitudinal spin fluctuations, respectively. In particular, the first principles single site disorder local moment method was proposed by Gyorffy *et. al.* [16]. Furthermore, Antropov *et. al.* [17] developed the *ab initio* spin dynamics method that doesn't use single site approximation and, in particular, allows to study the magnetic short range order in itinerant magnets.

The adiabatic approximation is valid only for materials close to the local moment limit, for example for Fe. However, for more itinerant systems where the inter-atomic exchange has significant contribution to the formation of the local moment, it is not justified and the longitudinal spin fluctuations must be treated on the same footing as the transverse spin fluctuations [11]. The effect of longitudinal spin fluctuations on magnetic thermodynamics of itinerant systems have been studied using classical Hamiltonians in which variable local moments play the role of dynamical variables and the parameters are found from first principles calculations [18, 19, 20].

## 1.2 Monte Carlo

The magnetic properties of materials can be very often described by lattice models with classical Hamiltonians. For example, the magnetism of local moment systems with strong uniaxial anisotropy can be well represented by the particularly simple

---

<sup>3</sup>In the magnetic insulators and rare-earth metals only the intra-atomic exchange, that leads to Hund rules, causes creation of a local moment.

Ising Hamiltonian

$$\mathcal{H} = -\frac{1}{2} \sum_{\mathbf{i}, \mathbf{j}} J_{\mathbf{i}-\mathbf{j}} s_{\mathbf{i}} s_{\mathbf{j}} - H \sum_{\mathbf{i}} s_{\mathbf{i}} \quad (1.11)$$

Here parameters  $J_{\mathbf{i}-\mathbf{j}}$  are called exchange constants and  $H$  is the magnetic field. The Ising variable,  $s_{\mathbf{i}}$ , can be either  $+1$  or  $-1$  and it describes the direction of the spin at the site  $\mathbf{i}$  of the lattice. The Ising model is also widely used to describe phase separation and ordering in binary alloys. A different model, appropriate for the magnetic metals close to the local moment limit, is the Heisenberg model

$$\mathcal{H} = -\frac{1}{2} \sum_{\mathbf{i}, \mathbf{j}} J_{\mathbf{i}-\mathbf{j}} \mathbf{S}_{\mathbf{i}} \cdot \mathbf{S}_{\mathbf{j}} - H \sum_{\mathbf{i}} S_{\mathbf{i}}^z \quad (1.12)$$

It has a similar form to the Ising Hamiltonian, but the Ising variables are replaced by classical unit vector  $\mathbf{S}_{\mathbf{i}}$  since in the absence of anisotropy the spins can point in any direction.

Monte Carlo method is a powerful tool to study thermodynamics of the above models. In fact, despite of the simplicity of the Hamiltonians, the analytic solution is usually not available while various approximation schemes necessarily introduce errors and often are not able to correctly describe physical phenomena especially for description of phase transitions. On the other hand, the Monte Carlo method can provide numerically exact answers of thermodynamic problems posed by above Hamiltonians. In this approach, instead on the original infinite lattice, we work on a finite system with some boundary conditions<sup>4</sup>. However, by performing the finite-size scaling analysis we can extrapolate results to the thermodynamic limit.

The usual goal in the thermodynamical description of the system is to calculate the expectation value  $\langle A \rangle$  of some observable quantity  $A$ , such as the energy or the magnetization. According to the statistical mechanics, such an expectation value can be found by averaging over all states  $\mu$  of the system weighted by the Boltzman factor

$$\langle A \rangle = \frac{\sum_{\mu} A_{\mu} e^{-\beta E_{\mu}}}{\sum_{\mu} e^{-\beta E_{\mu}}} \quad (1.13)$$

However, such direct evaluation of the expectation value is intractable for large systems due to huge number of terms in above summations. In fact, for the Ising system with  $N$  spins each summation has  $2^N$  terms. Since this number grows exponentially with the size of the system, it quickly becomes too large for even relatively small lattices. The situation is even worse for the Heisenberg model since we have infinite number of states for each spin. In the Monte Carlo method we go around this problem by choosing from all possible states of the system only a random subset with some specified probability distribution  $p_{\mu}$ . Suppose we choose  $n$  such states  $\mu_1, \dots, \mu_n$ . We

---

<sup>4</sup>Usually periodic boundary conditions are used.

then estimate  $\langle A \rangle$  by so called estimator given by

$$(A)_n = \frac{\sum_{i=1}^n A_{\mu_i} p_{\mu_i}^{-1} e^{-\beta E_{\mu_i}}}{\sum_{i=1}^n p_{\mu_i}^{-1} e^{-\beta E_{\mu_i}}} \quad (1.14)$$

$(A)_n$  has the property that as  $n$  increases, it becomes a more and more accurate estimate of  $\langle A \rangle$ . If the probability distribution  $p_{\mu}$  is chosen in such a way that only the states that make the largest contribution to the sums in Equation (1.14) are picked to the subset,  $(A)_n$  provides a good approximation for  $\langle A \rangle$  even for  $n$  much smaller than the total number of states. The states that make the largest contributions are those with the highest probability of occupation at a given temperature. Therefore, it is natural to choose  $p_{\mu}$  to be equal to the probability of occupation of state  $\mu$  in thermal equilibrium that is given by the Boltzman probability distribution

$$p_{\mu} \propto e^{-\beta E_{\mu}} \quad (1.15)$$

In this case the estimator becomes

$$(A)_n = \frac{1}{n} \sum_{i=1}^n A_{\mu_i} \quad (1.16)$$

A nontrivial part of Monte Carlo calculations is to generate an appropriate random set of states according to the Boltzman probability distribution. Note that we cannot simply choose states at random and accept or reject them with probability proportional to  $\propto e^{-\beta E_{\mu}}$ ; we would end up rejecting virtually all states because the probabilities for their acceptance would be exponentially small. Instead, almost all Monte Carlo schemes rely on Markov processes as the generating engine for the set of states used.

A Markov process is a mechanism that for a given state  $\mu$  generates another state  $\nu$  with probability  $P(\mu \rightarrow \nu)$  called transition probability. If Markov process is run repeatedly for some time, it generates a Markov chain of states. The transition probabilities are constant in time and depend only on properties of states  $\mu$  and  $\nu$ . They also satisfy normalization constraint  $\sum_{\nu} P(\mu \rightarrow \nu) = 1$  since Markov process must generate some state  $\mu$  when a handed a system in state  $\nu$ . Note however, that the transition probability  $P(\mu \rightarrow \mu)$  is in general nonzero so the system may just stay in the same state. In the Monte Carlo method the Markov process is chosen specially in such a way that if run for a sufficient amount of time starting from any state, it will eventually produce a succession of states that appear with Boltzman probability distribution. In order to achieve this we require Markov process to be ergodic i.e. it should be possible to reach any state of the system from any other state if we run Markov process long enough. This requirement is necessary since each state has nonzero probability in the Boltzman probability distribution. In addition, we put on

transition probabilities the detailed balance condition

$$p_\mu P(\mu \rightarrow \nu) = p_\nu P(\nu \rightarrow \mu) \quad (1.17)$$

As shown for example in Ref. [21] these conditions ensure that if Markov process is run for a sufficient amount of time it will eventually generate states with Boltzman probability distribution. It is convenient to break the transition probability down into two parts

$$P(\mu \rightarrow \nu) = g(\mu \rightarrow \nu)A(\mu \rightarrow \nu) \quad (1.18)$$

where  $g(\mu \rightarrow \nu)$  is called the selection probability, which is the probability that given initial state  $\mu$  the Markov process will generate a new target state  $\nu$ , and  $A(\mu \rightarrow \nu)$  is the acceptance ratio which is the probability that the target state  $\nu$  is accepted and the system moves to this state. Then using Equation (1.15) the detailed balance condition (1.17) becomes

$$\frac{g(\mu \rightarrow \nu)A(\mu \rightarrow \nu)}{g(\nu \rightarrow \mu)A(\nu \rightarrow \mu)} = e^{-\beta(E_\nu - E_\mu)} \quad (1.19)$$

Note that the ergodicity requirement and the above constraint still leave a lot of freedom for choosing selection probabilities and acceptance ratios. Different choices correspond to different Monte Carlo algorithms. In general, in order to have an efficient algorithm the acceptance ratios should be as close to unity as possible.

We focus now on a specific example of Ising or Heisenberg model. We consider an algorithm with a single-spin dynamics, i.e., we chooses transition probabilities to be nonzero only for states differing by direction of a single spin. The selection probabilities between all such states are assumed to be equal

$$g(\mu \rightarrow \nu) = \frac{1}{N} \quad (1.20)$$

where  $N$  is the number of spins in the lattice. From Equation (1.19) we then have

$$\frac{A(\mu \rightarrow \nu)}{A(\nu \rightarrow \mu)} = e^{-\beta(E_\nu - E_\mu)} \quad (1.21)$$

A very efficient choice of acceptance ratio that satisfy (1.21) is provided by the famous Metropolis algorithm [22]

$$A(\mu \rightarrow \nu) = \begin{cases} e^{-\beta(E_\nu - E_\mu)} & \text{if } E_\nu - E_\mu > 0 \\ 1 & \text{otherwise} \end{cases} \quad (1.22)$$

In the Monte Carlo calculations we start with the system in some initial state<sup>5</sup> and in

---

<sup>5</sup>Common initial states include the perfectly ordered state with all spins aligned and the totally disordered state with random directions of spin. There many possible types of the latter state

each Monte Carlo step we run the Markov process. The number of Monte Carlo steps after which the system is equilibrated (i.e., the Markov process produces states with Boltzman distribution) for any initial state of the system is called the equilibration time. Since the equilibration time increases with the lattices size, it is convenient to measure it in Monte Carlo steps per site. Usually the equilibration time for a given temperature can be estimated by calculating some quantities like energy or magnetization every some Monte Carlo steps and plotting them as a function of time (measured in Monte Carlo steps) from the beginning of the simulation. When these quantities reach approximately constant values, we then deduce that the system has equilibrated<sup>6</sup>.

After the system has equilibrated, different quantities of interest can be measured (calculated) every  $\Delta t$  Monte Carlo steps and their estimators can be found from Equation (1.16). Here  $\Delta t$  is some arbitrarily chosen interval; usually few Monte Carlo steps per site. The estimate of the deviation of the estimator from the true expectation value for the same lattice size is given by [23]

$$\sigma_A = \sqrt{\frac{1 + 2\tau/\Delta t}{n - 1}} (\Delta A^2)_n \quad (1.23)$$

where  $(\Delta A^2)_n = (A^2)_n - (A)_n^2$  is the estimator of the fluctuation of quantity  $A$  and  $\tau$  is the correlation time that is a measure of how long it takes the system to go from one state to another one which is significantly different from the first. The correlation time can be rigorously found from the time-displaced correlation function of some quantity (see for example Ref. [21]). In most cases however it is safe to assume that the correlation time is equal to the equilibration time.

While estimators of many quantities can be calculated directly from Equation (1.16), the response functions are most conveniently found from fluctuations of the corresponding quantities using the fluctuation-dissipation theorem. The estimation of the error of such calculated response functions cannot be done by straightforward generalization of Equation (1.23) and therefore different techniques like blocking, bootstrap, or jackknife methods are usually employed (see for example Ref. [21]).

In the Monte Carlo simulations of the ferromagnetic Ising or Heisenberg model without external field there is an ambiguity in calculation of magnetization<sup>7</sup>. Indeed, for the Ising case there are two degenerate ordered states differing by sign of the magnetization. Therefore, even below the Curie temperature, for a sufficiently long

---

corresponding to different choice of the seed for random number generator.

<sup>6</sup>In many cases it is possible for the system to get stuck in a metastable state producing roughly constant values of all the observed quantities and so appearing to reach equilibrium. In order to avoid this pitfall one should determine equilibration time starting from few different initial states and check whether they agree. Since for different initial states the system takes different paths to the equilibrium, it is very unlikely it will get stuck in the same metastable state.

<sup>7</sup>In general, the problem of vanishing order parameter in the ordered state appears whenever this state is degenerate. In this case one usually defines root mean square order parameter and its susceptibility.

Monte Carlo run, the system can switch from one ordered state to the other and the resulting estimator of the magnetization,  $(M)_n$  is zero. The situation is even worse for the Heisenberg case where we have continuum of degenerate ordered states differing by direction of magnetization and it costs no energy to go from one state to another. The usual solution of this problem is to calculate instead the magnitude of magnetization,  $(|M|)_n$  or its root mean square (rms) value,  $\sqrt{(M^2)_n}$  because they are the same for all degenerate states. Correspondingly, the magnetic susceptibility is defined as

$$\chi = \begin{cases} \frac{\beta}{N}((M^2)_n - (|M|)_n^2) & \text{for } T < T_C \\ \frac{\beta}{N}(M^2)_n & \text{for } T > T_C \end{cases} \quad (1.24)$$

While the magnitude or rms of magnetization differ from the actual magnetization and, in particular, they are always nonzero even in the paramagnetic state, for large large lattices and away from the critical point the error between all these quantities is of the order of  $1/N$ .

For all temperatures, except those close to the phase transition, the properties of the system quickly converge with the size of the lattice supercell. The reason is that in this case the correlations in the system are short range and can be well described by even relatively small supercells. On the other hand, close to the critical point the length scale of the fluctuations, called the correlation length, anomalously increases and diverges at the critical point itself. Because of this divergence it is impossible to represent the properties of the system at the critical temperature for any finite lattice. Fortunately, the scaling behavior for different quantities of interest in the critical region as the lattice increases is known (see for example Refs. [24]). This finite size scaling theory allows to find the critical properties of the system on the infinite lattice like for example critical exponents by considering different supercell sizes. The details of the finite size scaling methods on Monte Carlo calculations are described in many books, for example [21, 24]. Here we just mention the scaling behavior of the fourth order cumulant of magnetization

$$U_M = 1 - \frac{(M^4)_n}{3(M^2)_n^2} \quad (1.25)$$

As size of the lattice goes to  $\infty$  we have  $U_M \rightarrow 0$  for  $T > T_C$  and  $U_M \rightarrow 2/3$  for  $T < T_C$  [25]. For large enough lattices, curves of  $U_M$  as a function of temperature for different lattice sizes crosses at the critical temperature<sup>8</sup> [25]. This property allows for a simple determination of the critical temperature.

When the Hamiltonian has a long range interaction it may be unsuitable to solve the problem in the real space because it would require too large supercells. In this case one can treat the problem in the Fourier space. Consider for simplicity the Ising model with the Hamiltonian (1.11) defined on a hypercubic lattice<sup>9</sup> with side  $L$ . In

<sup>8</sup>The same properties have fourth order cumulants of other types of order parameters.

<sup>9</sup>The generalization of the results to the Heisenberg system or to different lattices is trivial.

each Monte Carlo step we evaluate the first term of the Hamiltonian (1.11) in the Fourier space. More specifically, we define the discrete Fourier transform of the Ising variables

$$s_{\mathbf{i}} = \frac{1}{L^d} \sum_{\mathbf{q}=0}^{L^d} s_{\mathbf{q}} e^{-2\pi i \mathbf{i} \cdot \mathbf{q} / L} \quad (1.26)$$

$$s_{\mathbf{q}} = \sum_{\mathbf{i}=0}^{L^d} s_{\mathbf{i}} e^{2\pi i \mathbf{i} \cdot \mathbf{q} / L} \quad (1.27)$$

where  $d$  is the number of dimensions. The first term of the Hamiltonian (1.11) can be then written as  $-\frac{1}{2} \frac{1}{L^d} \sum_{\mathbf{q}=0}^{L^d} J_{\mathbf{q}} |s_{\mathbf{q}}|^2$  where we defined the Fourier transform of the exchange constants

$$J_{\mathbf{q}} = \sum_{\mathbf{i}-\mathbf{j}=0}^{L^d} J_{\mathbf{i}-\mathbf{j}} e^{2\pi i (\mathbf{i}-\mathbf{j}) \cdot \mathbf{q} / L} \quad (1.28)$$

Note that  $J_{\mathbf{q}}$  can be calculated once and for all for each  $\mathbf{q}$  allowed by a supercell.

## 1.3 *Ab initio* methods

Material specific properties can be studied theoretically using first principles electronic structure calculations. These techniques are often called *ab initio* methods since they attempt to directly solve the Schrödinger equation for a given system with no free parameters.

### 1.3.1 Density functional theory

Density functional theory is a basis of a majority of first principles methods. It is based on two fundamental theorems [26]. Consider a system of  $N$  interacting electrons in the external potential<sup>10</sup>  $V_{ext}(\mathbf{r})$ .

$$\mathcal{H} = \sum_{i=1}^N \left[ -\frac{\hbar^2}{2m} \nabla_i^2 + \frac{1}{2} \sum_{j \neq i}^N \frac{e^2}{|\mathbf{r}_i - \mathbf{r}_j|} + V_{ext}(\mathbf{r}_i) \right] \quad (1.29)$$

The first theorem states that  $V_{ext}(\mathbf{r})$ , and therefore also the Hamiltonian, is implicitly determined by the ground state electron density  $\rho(\mathbf{r})$ . Consequently, the ground state energy, as any other property of the system, is a unique functional of the ground state

---

<sup>10</sup>The external potential usually represent the interaction of electrons with nuclei that are treated in the Born-Oppenheimer approximation.

density and can be written as

$$E[\rho] = T[\rho] + \int \int \frac{\rho(\mathbf{r})\rho(\mathbf{r}')}{|\mathbf{r} - \mathbf{r}'|} + W_{ee}[\rho] + \int V_{ext}(\mathbf{r})\rho(\mathbf{r})d^3\mathbf{r} \quad (1.30)$$

The first and the second terms are kinetic and Hartree energies, respectively.  $W_{ee}$  represents the remaining (nonclassical) part of the electron-electron interaction and the last term describes interaction of electrons with the external potential. According to the second theorem this energy functional is minimized by the ground state density.

Kohn and Sham [27] proposed an ansatz that there exists an auxiliary noninteracting system of electrons in an effective potential  $V_{eff}(\mathbf{r})$  that has exactly the same ground state density as the original interacting system<sup>11</sup>. In terms of eigenstates of the noninteracting system,  $\psi_i(\mathbf{r})$  we have

$$\rho(\mathbf{r}) = \sum_{i=1}^{occ} |\psi_i(\mathbf{r})|^2 \quad (1.31)$$

Minimizing the energy (1.30) with respect to the density (1.31), we obtain Kohn-Sham equation

$$\mathcal{H}_{KS}\psi_i(\mathbf{r}) = \left[ -\frac{\hbar^2}{2m}\nabla^2 + V_{eff}(\mathbf{r}) \right] \psi_i(\mathbf{r}) = \epsilon_i\psi_i(\mathbf{r}) \quad (1.32)$$

with the effective potential given by

$$V_{eff}(\mathbf{r}) = V_{ext}(\mathbf{r}) + \int \frac{2\rho(\mathbf{r}')}{|\mathbf{r} - \mathbf{r}'|}d^3\mathbf{r}' + V_{xc}(\mathbf{r}) \quad (1.33)$$

Here  $V_{xc}(\mathbf{r}) = \frac{\delta E_{xc}[\rho]}{\delta \rho(\mathbf{r})}$  is the exchange-correlation potential and  $E_{xc}[\rho]$  is the exchange-correlation energy that is formally defined as  $E_{xc} = W_{ee}[\rho] + T[\rho] - T_s[\rho]$  where  $T_s[\rho]$  is the kinetic energy of the noninteracting system. In principle, the eigenvalues  $\epsilon_i$  don't correspond to the elementary excitations of the interacting system. Nevertheless, in practice this correspondence is often assumed which basically has a meaning of the mean-field approximation that replaces the original interacting system by the noninteracting electrons in the effective potential.

The above equations can be easily generalized to the case of a collinear spin polarized systems if the total energy is considered to be the functional of separately spin up and down densities,  $\rho^\uparrow$  and  $\rho^\downarrow$ . From the Kohn-Sham ansatz  $\rho^\sigma = \sum_{i=1}^{occ} |\psi_i^\sigma(\mathbf{r})|^2$  where  $\psi_i^\sigma(\mathbf{r})$  are the solutions of the Kohn-Sham equation with spin dependent exchange-correlation potential  $V_{xc}^\sigma(\mathbf{r}) = \frac{\delta E_{xc}[\rho^\uparrow, \rho^\downarrow]}{\delta \rho^\sigma(\mathbf{r})}$ . For the noncollinear case the energy is a functional of the spin density matrix that from the Kohn-Sham ansatz is given by  $\rho^{\alpha\beta}(\mathbf{r}) = \sum_{i=1}^{occ} \psi_i^{\alpha*}(\mathbf{r})\psi_i^\beta(\mathbf{r})$  where  $\psi_i^\alpha$  is  $\alpha$  component of the spinor eigenstate of the spin matrix Kohn-Sham equation with the exchange-correlation potential  $V_{xc}^{\alpha\beta}(\mathbf{r}) =$

<sup>11</sup>This assumption can be actually lifted, see Ref. [28]

$$\frac{\delta E_{xc}[\{\rho^{\alpha\beta}\}]}{\delta \rho_{\alpha\beta}(\mathbf{r})}.$$

The exact functional form of  $E_{xc}[\{\rho^{\alpha\beta}\}]$  is unknown and approximations must be made to proceed. The most commonly used is the Local Density Approximation (LDA) [27]

$$E_{xc}[\{\rho^{\alpha\beta}\}] = \int \rho(\mathbf{r}) \epsilon_{xc}[\rho^\uparrow(\mathbf{r}), \rho^\downarrow(\mathbf{r})] d^3\mathbf{r} \quad (1.34)$$

Here  $\epsilon_{xc}[\rho^\uparrow, \rho^\downarrow]$  is the exchange-correlation energy per particle of the homogenous electron gas which was calculated to great accuracy with the Quantum Monte Carlo method [29] for different spin up and down densities. At each point  $\rho^\uparrow$  and  $\rho^\downarrow$  are found by diagonalizing the spin density matrix  $\rho^{\alpha\beta}$  and then  $\epsilon_{xc}[\rho^\uparrow, \rho^\downarrow]$  is obtained using some possible parameterizations of the Quantum Monte Carlo results [30, 31].

The LDA has been remarkably successful in describing the properties of many different materials. There are however a lot of well known failures of LDA such as underestimation of band gaps in semiconductors and insulators, or incorrect description of transition metal compounds and rare-earth systems. Number of different generalizations of LDA has been proposed (see for example Ref. [32]). Here we just describe the LDA+U method [33] that significantly improves the description of strongly correlated systems. In this approach we separate electrons into two subsystems: localized (usually  $d$  or  $f$ ) electrons for which Coulomb interaction is strong and cannot be described by LDA and delocalized electrons (usually  $s$  or  $p$ ) that are well described by LDA. The idea is to correct LDA errors by adding an additional orbital dependent Hubbard-like interaction between the localized electrons. More specifically, we define spheres around atomic cores for which the atomic characteristics of the localized electrons have largely survived. Within these atomic spheres we expand in a localized orthonormal basis  $|inlm\sigma\rangle$  ( $i$  denotes the site,  $n$  the main quantum number,  $l$  the orbital quantum number,  $m$  the magnetic quantum number, and  $\sigma$  the spin index<sup>12</sup>). Let us assume that the localized electrons belong to a single  $nl$ -shell. The  $m$ -resolved density matrix is  $n_{mm'}^\sigma = -\frac{1}{\pi} \int^{E_F} \Im G_{inlm, inlm'}^\sigma(E) dE$  where  $G_{inlm, inlm'}^\sigma(E)$  are the elements of the Green's function in the localized representation. The LDA+U energy functional is defined by

$$E^{LDA+U}[\{\rho^\sigma\}, \{n_{mm'}^\sigma\}] = E^{LDA}[\{\rho^\sigma\}] + E^U[\{n_{mm'}^\sigma\}] - E_{dc}[\{n_{mm'}^\sigma\}] \quad (1.35)$$

The first term is the LDA energy functional, the second term represents the additional Hubbard-like interaction between localized electrons, and the last term corrects for double-counting (it is the part of  $E^U$  that is already present in  $E^{LDA}$ ). In the full spherically symmetric form of LDA+U [34] we have

$$E^U[\{n_{mm'}^\sigma\}] = \frac{1}{2} \sum_{\sigma, \{m\}} \left[ U_{m'm''}^{mm''} n_{mm'}^\sigma n_{m''m''}^{-\sigma} - \left( U_{m'm''}^{mm''} - J_{m''m''}^{mm''} \right) n_{mm'}^\sigma n_{m''m''}^\sigma \right] \quad (1.36)$$

---

<sup>12</sup>For simplicity we assume here collinear system; the generalization to the noncollinear case can be done in the spirit of above discussion.

Here  $U_{m'm''}^{mm''} = \langle m, m'' | V_{ee} | m', m''' \rangle$  and  $J_{m''m'}^{mm''} = \langle m, m'' | V_{ee} | m''', m' \rangle$  ( $V_{ee}$  is the screened Coulomb interaction among  $nl$ -electrons) can be expressed in terms of renormalized Coulomb and exchange parameters  $U$  and  $J$  [34]. In the fully localized (atomic) limit<sup>13</sup> the double counting term is given by

$$E_{dc}[\{n_{mm'}^\sigma\}] = \frac{1}{2}UN(N-1) - \frac{1}{2}J \sum_{\sigma} N^{\sigma}(N^{\sigma}-1) \quad (1.37)$$

where  $N^{\sigma} = \text{Tr}(n_{mm'}^{\sigma})$  and  $N = \sum_{\sigma} N^{\sigma}$ . By minimizing the energy functional (1.35) with respect to  $\{\rho^{\sigma}\}$  and  $\{n_{mm'}^{\sigma}\}$  we obtain a generalized Kohn-Sham Hamiltonian with additional orbital dependent nonlocal potential

$$\mathcal{H}_{KS}^{LDA+U} = \mathcal{H}_{KS}^{LDA} + \sum_{mm'} |inlm\sigma\rangle V_{mm'}^{\sigma} \langle inlm'\sigma| \quad (1.38)$$

with

$$V_{mm'}^{\sigma} = \sum_{m'',m'''} \left[ U_{m'm''}^{mm''} n_{m''m'''}^{-\sigma} - \left( U_{m'm''}^{mm''} - J_{m''m'}^{mm''} \right) n_{m''m'''}^{\sigma} \right] - U(N - \frac{1}{2}) + J(N^{\sigma} - \frac{1}{2}) \quad (1.39)$$

The above formalism can be simplified if we perform a spherical averaging of Equation (1.36). The energy functional in this spherically averaged LDA+U method is [37]

$$E^{LDA+U}[\{\rho^{\sigma}\}, \{n_{mm'}^{\sigma}\}] = E^{LDA}[\{\rho^{\sigma}\}] + \frac{U-J}{2} \sum_{\sigma} \left[ \sum_m n_{mm}^{\sigma} - \sum_{mm'} n_{mm'}^{\sigma} n_{m'm}^{\sigma} \right] \quad (1.40)$$

The corresponding Kohn-Sham Hamiltonian is given by Equation (1.38) with

$$V_{mm'}^{\sigma} = (U-J) \left( \frac{1}{2} \delta_{mm'} - n_{mm'}^{\sigma} \right) \quad (1.41)$$

The LDA+U method involves two parameters  $U$  and  $J$  (the spherically averaged form has only one parameter  $U-J$ ) that can be found using the constrained occupation method [38] (see also Section 2.2). While this approach provide a good approximation for the value of  $J$ , the parameter  $U$  is not well defined [39]. For this reason  $U$  is often treated as an empirical parameter in the LDA+U calculations. Another ambiguity of the LDA+U method is that, as seen from Equation (1.38), the Hamiltonian depends on the choice of the localized basis. However, the experience in using LDA+U in various electronic structure calculations shows that results are not sensitive to the particular form of the localized orbitals [40].

<sup>13</sup>Alternative forms for the double counting term exist in literature, see Refs. [35, 36]

### 1.3.2 Solving Kohn-Sham equation

Solving the Kohn-Sham equation (1.32) can be greatly simplified if the external potential is due to a periodic lattice of nuclei, i.e. the effective potential (1.33) obeys the periodicity condition  $V_{eff}(\mathbf{r} + \mathbf{T}) = V_{eff}(\mathbf{r})$  where  $\mathbf{T}$  is an arbitrary translation vector of the lattice. In this case the Bloch theorem states that the solutions of the Kohn-Sham equation have the form

$$\psi_{\nu\mathbf{k}} = u_{\nu\mathbf{k}} \exp(i\mathbf{k} \cdot \mathbf{r}) \quad (1.42)$$

where  $\mathbf{k}$  is the wavevector from the first Brillouin zone of the lattice,  $\nu$  is a band index<sup>14</sup>, and the function  $u_{\nu\mathbf{k}}$  satisfies  $u_{\nu\mathbf{k}}(\mathbf{r} + \mathbf{T}) = u_{\nu\mathbf{k}}(\mathbf{r})$ . Bloch theorem allows us to consider each  $\mathbf{k}$  point separately that considerably simplifies the calculations. Unfortunately, there are many important situation for which the external potential is not periodic, such as surfaces or disordered systems. In this case however, one can artificially create periodicity by introducing a large supercell. In particular, for surfaces the supercell contains a finite slab several atomic layer thick and the vacuum region such that periodic images of the slab don't interact with each other. On the other hand, for disordered systems different disorder configurations can be simulated by large supercells.

Typically, we expand the solution of the Kohn-Sham equation in some complete basis of functions  $\chi_{i\mathbf{k}}$  that satisfy the Bloch condition (1.42).

$$\psi_{\nu\mathbf{k}}(\mathbf{r}) = \sum_i c_{i,\nu\mathbf{k}} \chi_{i\mathbf{k}}(\mathbf{r}) \quad (1.43)$$

From Equation (1.32) we then obtain

$$\sum_j [\mathcal{H}_{ij}(\mathbf{k}) - \epsilon_{\nu\mathbf{k}} O_{ij}(\mathbf{k})] c_{j,\nu\mathbf{k}} = 0 \quad (1.44)$$

where  $\mathcal{H}_{ij}(\mathbf{k}) = \int_{\Omega} \chi_{i\mathbf{k}}^*(\mathbf{r}) \mathcal{H}_{KS} \chi_{j\mathbf{k}}(\mathbf{r})$  and  $O_{ij}(\mathbf{k}) = \int_{\Omega} \chi_{i\mathbf{k}}^*(\mathbf{r}) \chi_{j\mathbf{k}}(\mathbf{r})$  with  $\Omega$  being the volume of the unit cell. The energies  $\epsilon_{\nu\mathbf{k}}$  can be found from the secular equation

$$\det [H_{ij}(\mathbf{k}) - \epsilon_{\nu\mathbf{k}} O_{ij}(\mathbf{k})] = 0 \quad (1.45)$$

There are many possible choices of basis functions that correspond to different electronic structure methods. The better we chose the basis functions, the smallest number of them is needed for a description of  $\psi_{\nu\mathbf{k}}$ . Plane waves provide a particularly simple basis. they are, however, not very suitable for description of strong oscillations of the wave function in the core region. For this reason plane wave expansion is only used together with the pseudo-potential method (see for example Refs. [41, 42]). An alternative approach is to construct an efficient basis from the solution of the radial

---

<sup>14</sup>For simplicity spin is neglected here; the generalization that includes spin is straightforward.

Schrödinger equation for each atomic sphere. Even though such constructed basis is energy dependent, it can be made energy independent by the linearization procedure [43]. A particular example of such approach is, described below, linear muffin-tin orbitals method [43].

### 1.3.3 Tight-binding linear muffin-tin orbitals

In this subsection we briefly describe the tight-binding linear muffin-tin orbitals (LMTO) method. The more detailed description may be found in Refs. [44, 45, 46].

For most of solids the effective potential has an approximate muffin-tin form, i.e. it is spherically symmetric in the spheres around atomic cores and constant in the interstitial region between the spheres. The TB-LMTO method is based on the atomic sphere approximation (ASA) in which the interstitial region is made volumeless by extending the atomic spheres radii such that they fill the whole space. Consequently, the kinetic energy can be neglected in the interstitial region and the Kohn-Sham equation reduces there to the Laplace equation. Note that ASA necessarily leads to the overlap between the spheres. For close packed systems, the overlap is relatively small and ASA is justified in this case. The general solution of the Laplace equation is a linear combination of the regular  $J_L(\mathbf{r})$  and irregular  $K_L(\mathbf{r})$  solution;  $L = (l, m)$  where  $l$  and  $m$  are orbital and magnetic quantum numbers, respectively. The regular and irregular solutions satisfy the following expansion theorem

$$K_L(\mathbf{r}_{\mathbf{R}}) = - \sum_{L'} S_{\mathbf{R}L, \mathbf{R}'L'} J_{L'}(\mathbf{r}_{\mathbf{R}'}) \quad (1.46)$$

Here  $\mathbf{r}_{\mathbf{R}}$  denotes the position vector with respect to origin at  $\mathbf{R}$  and  $S_{\mathbf{R}L, \mathbf{R}'L'}$  are called canonical structure constants [44] that decay with distance  $|\mathbf{R} - \mathbf{R}'|$  as an inverse power law.

In order to construct the LMTO basis, we first consider the Taylor expansion of the solution of the Kohn-Sham equation in the atomic sphere  $\mathbf{R}$  with the free atom boundary conditions,  $\phi_{\mathbf{R}L}(E, \mathbf{r})$ , up to first order around some arbitrarily chosen energy  $E_l$ . Linear muffin-tin orbitals (LMTO)  $\chi_{\mathbf{R}L}(\mathbf{r})$  are then obtained starting from  $K_L(\mathbf{r}_{\mathbf{R}})$  defined in the whole space and using Equation (1.46) for all spheres  $\mathbf{R}' \neq \mathbf{R}$ , and then replacing  $J_L(\mathbf{r})$  and  $K_L(\mathbf{r})$  in all atomic spheres by this Taylor expansion requiring simultaneously continuous matching across the spheres boundaries. The last condition fixes the energy in the first term of the Taylor expansion making  $\chi_{\mathbf{R}L}(\mathbf{r})$  energy independent.

$$\chi_{\mathbf{R}L}(\mathbf{r}) = \begin{cases} -\{K, \dot{\phi}\}_{\mathbf{R}L} \phi_{\mathbf{R}L}(\mathbf{r}_{\mathbf{R}}) + \{K, \phi\}_{\mathbf{R}L} \dot{\phi}_{\mathbf{R}L}(\mathbf{r}_{\mathbf{R}}) & r_{\mathbf{R}} \leq s_{\mathbf{R}} \\ \sum_{L'} S_{\mathbf{R}L, \mathbf{R}'L'} [\{J, \dot{\phi}\}_{\mathbf{R}'L'} \phi_{\mathbf{R}'L'}(\mathbf{r}_{\mathbf{R}'}) - \{J, \phi\}_{\mathbf{R}'L'} \dot{\phi}_{\mathbf{R}'L'}(\mathbf{r}_{\mathbf{R}'})] & r_{\mathbf{R}'} \leq s_{\mathbf{R}'} (\mathbf{R}' \neq \mathbf{R}) \\ K_L(\mathbf{r}_{\mathbf{R}}) & \mathbf{r} \in I \end{cases} \quad (1.47)$$

where  $s_{\mathbf{R}}$  is the sphere radius,  $\phi_{\mathbf{RL}} = \phi_{\mathbf{RL}}(E_l)$ ,  $\dot{\phi}_{\mathbf{RL}}$  denotes energy derivative of  $\phi_{\mathbf{RL}}(E, \mathbf{r})$  evaluated at  $E = E_l$ , and  $\{f, g\}_{\mathbf{RL}}$  is the Wronskian of functions  $f_{\mathbf{RL}}$  and  $g_{\mathbf{RL}}$ . The LMTO basis is obtained by taking the Bloch sum of LMTO orbitals. Note that due to its construction the error between solutions of Kohn-Sham equation and the LMTO basis functions is of the order of  $E - E_l$  and thus the eigenvalues obtained from variational method (1.45) are correct up to third order in  $E - E_l$ . Therefore, by the appropriate choice of  $E_l$  we can obtain a very accurate description of electronic structure with a minimal basis<sup>15</sup>.

From Equation (1.47), it is seen that  $\chi_{\mathbf{RL}}(\mathbf{r})$  are very extended due to long-range nature of  $S_{\mathbf{RL}, \mathbf{R}'L'}$ . This is inconvenient for many applications such as transport. However, it turns out that the choice of LMTO orbitals is not unique due to freedom in choosing the normalization of  $\phi_{\mathbf{RL}}(E)$  [45]. Different normalizations correspond to different representations of LMTO and lead to screening of  $S_{\mathbf{RL}, \mathbf{R}'L'}$ . In particular, for TB-LMTO representation the structure constants, and therefore  $\chi_{\mathbf{RL}}(\mathbf{r})$ , become short-range and usually extend only up to next nearest neighbors.

---

<sup>15</sup>Usually good results are obtained for the angular momentum cutoff  $l_{max} = 2$  except for the  $f$  systems for which  $l_{max} = 3$  should be used.

# Bibliography

- [1] P. Langevin, J. Phys. (Paris) **4**, 678 (1905); Ann. Chim. Phys. **5**, 70 (1905)
- [2] P. Weiss, J. Phys. Radium **6**, 661 (1907).
- [3] Ch. Kittel, *Introduction to Solid State Physics* (7th ed., John Willey & Sons, Inc., 1996).
- [4] J. H. Van Vleck, *Theory of Electric and Magnetic Susceptibilities* (Oxford University Press, Oxford, 1932).
- [5] W. Heisenberg, Z. Phys. **49**, 619 (1936).
- [6] P. W. Anderson, in *Solid State Physics* **14**, 99 (Academic, New York, 1963).
- [7] L. M. Sandratskii, Adv. Phys. **447**, 91 (1998).
- [8] A. I. Liechtenstein, *et. al.*, J. Magn. Magn. Mater. **67**, 65 (1987).
- [9] J. C. Slater, Phys. Rev. **49**, 537, 931 (1936).
- [10] E. C. Stoner, Proc. R. Soc. **165A**, 372 (1938).
- [11] T. Moriya, *Spin fluctuations in itinerant electron magnetism* (Springer, Berlin, 1985).
- [12] L. M. Sandratskii and J. Kübler, J. Phys.: Cond. Matter **4**, 6927 (1992).
- [13] J. F. Janak, Phys. rev. B, **16**, 255 (1977).
- [14] V. L. Moruzzi, J. F. Janak, and A. R. Williams, *Calculated Electronic Properties in Metals* (New York, Pergamon, 1978).
- [15] P. W. Anderson, Phys. Rev. **115**, 2 (1959).
- [16] B. L. Gyorffy, *et. al.*, J. Phys. F: Met. Phys. **15**, 1337 (1985).
- [17] V. P. Antropov, *et. al.*, **54**, 1019 (1996).
- [18] M. Uhl and J. Kübler, Phys. Rev. Lett. **77**, 334 (1996).

- [19] N. M. Rosengaard and B. Johansson, *Phys. Rev. B* **55**, 14975 (1997).
- [20] A. V. Ruban, *et. al.*, *Phys. Rev. B* **75**, 054402 (2007).
- [21] M. E. J. Newman, G. T. Barkema, *Monte Carlo Methods in Statistical Physics* (Clarendon Press, Oxford, 1999).
- [22] N. Metropolis, *et. al.*, *J. Chem. Phys.* **21**, 1087 (1953).
- [23] H. Müller-Krumbhaar and K. Binder, *J. Stat. Phys.* **8**, 1 (1973).
- [24] K. Binder and D. W. Heermann, *Monte Carlo Simulations in Statistical Physics* (Springer-Verlag, Berlin, 1992).
- [25] K. Binder, *Z. Phys. B* **43**, 119 (1981).
- [26] P. Hohenberg and W. Kohn, *Phys. Rev.* **136**, B864 (1964).
- [27] W. Kohn and L. J. Sham, *Phys. Rev.* **140**, A1133 (1965).
- [28] M. Levy and J. P. Perdew, in *Density Functional Methods in Physics*, ed. by R. M. Dreizler and J. da Providencia (Plenum Press, New York, 1985).
- [29] D. M. Ceperley and B. J. Alder, *Phys. Rev. Lett.* **45**, 566 (1980).
- [30] J. P. Perdew and A. Zunger, *Phys. Rev. B* **23**, 5048 (1981).
- [31] S. Vosko, L. Wilk, and M. Nusair, *Can. J. Phys.* **58**, 1200 (1983).
- [32] R. M. Martin, *Electronic Structure: Basic Theory and Applications* (Cambridge University Press, Cambridge, 2004).
- [33] V. I. Anisimov, J. Zaanen, and O. K. Andersen, *Phys. Rev. B* **44**, 943 (1991).
- [34] A. I. Liechtenstein, V. I. Anisimov, and J. Zaanen, *Phys. Rev. B* **52**, R5467 (1995).
- [35] M. T. Czyżyk and G. A. Sawatzky, *Phys. Rev. B* **49**, 14211 (1994).
- [36] A. G. Petukhov, *et. al.*, *Phys. Rev. B* **67**, 153106 (2003).
- [37] S. L. Dudarev, *et. al.*, *Phys. Rev. B* **57**, 1505 (1998).
- [38] V. I. Anisimov and O. Gunnarson, *Phys. Rev. B* **43**, 7570 (1991).
- [39] I. V. Solovyev, and P. H. Dederichs, *Phys. Rev. B* **49**, 6736 (1994).
- [40] V. I. Anisimov, F. Aryasetiawan, and A. I. Liechtenstein, *J. Phys.: Condens. Matter* **9**, 767 (1997).

- [41] M. C. Payne, *et. al.*, Rev. Mod. Phys. **64**, 1045 (1992).
- [42] D. Vanderbilt, Phys. Rev. B **41**, 7892 (1990).
- [43] O. K. Andersen, Phys. Rev. B **12**, 3060 (1975).
- [44] H. L. Skriver, *The LMTO method* (Springer-Verlag, Berlin, 1984).
- [45] O. K. Andersen, O. Jepsen, and D. Glötzl, in *Highlights of Condensed Matter Theory*, ed. by F. Bassani, F. Fumi, and M. P. Tsoi (North-Holland, New York, 1985).
- [46] I. Turek, V. Drchal, J. Kudrnovský, M. Šob, and P. Weinberger, *Electronic Structure of Disordered Alloys, Surfaces and Interfaces* (Kluwer, Boston, 1997).

## Chapter 2

# Magnetism of $\text{Cr}_2\text{O}_3$

Here we used first principles electronic structure calculations to study the magnetism of antiferromagnetic  $\text{Cr}_2\text{O}_3$ . The strong electronic correlations between the  $d$  electrons on Cr atoms are taken into account using LDA+U method. The band gap was found to be of the Mott-Hubbard type and a very good agreement with experiment was obtained for ground state properties for values of  $U$  and  $J$  close to those obtained from the constrained occupation method. Since  $\text{Cr}_2\text{O}_3$  is an antiferromagnetic insulator, its local magnetic moment is expected to be of atomic nature. Indeed, we found that the local moment is close to  $3\mu_B$  and is associated with the total spin  $S = 3/2$  that comes from the filled majority and empty minority  $t_{2g}$  orbitals. In addition, we found that magnetic energies can be very well fitted to the Heisenberg Hamiltonian with strong exchange interaction with two nearest neighbors and additional weak interaction up to the fifth neighbor shell. These energies are insensitive to the position of the oxygen states, indicating that the magnetism in  $\text{Cr}_2\text{O}_3$  is dominated by the direct kinetic exchange. The Néel temperature was calculated using the pair-cluster approximation applied to the spin-3/2 quantum Heisenberg model and was found to be in a very good agreement with experiment.

### 2.1 Introduction

Corundum-type  $\text{Cr}_2\text{O}_3$  is one of the antiferromagnetic transition-metal oxides which present a challenge for electronic band theory due to the correlated character of the partially filled, spin-polarized  $3d$  shell. It also has numerous applications in steel surface coatings [17] and heterogeneous catalysis [16]. It is therefore very desirable to establish whether electronic correlations can be reliably included in first-principles calculations in a way that would accurately predict structural, electronic, and magnetic properties.

As expected for a transition-metal oxide, conventional density-functional theory (DFT) studies of bulk  $\text{Cr}_2\text{O}_3$  [3, 4, 5] have shown that the local density approximation (LDA) or the generalized-gradient approximation (GGA) for the exchange-correlation

potential are unable to reproduce the electronic and magnetic properties of bulk  $\text{Cr}_2\text{O}_3$ . Rohrbach *et al.* [6] performed a GGA+U calculation for  $\text{Cr}_2\text{O}_3$  using the simplified (spherically averaged)  $U - J$  correction [7] and obtained more reasonable results for the band structure. However, this approach is inaccurate for structural and magnetic properties. First, as is typical for transition-metal compounds, both GGA and the LDA+U corrections reduce the LDA overbinding problem in  $\text{Cr}_2\text{O}_3$  and increase the equilibrium volume which becomes close to the experimental value. However, the use of *both* GGA and Hubbard  $U$  in the GGA+U method [6] results in an overcorrection, so that the equilibrium volume becomes 7% too large. Second, the magnetic energies found by Rohrbach *et al.* within this method are incompatible with the experimental Néel temperature of about 308 K; they are too small roughly by a factor of five. Mosey *et al.* [8] obtained better overall agreement with experiment for structural and spectral properties using the spherically averaged LDA+U method [7] with  $U - J = 3.2$  eV, but the magnetic properties were not considered.

Here we analyze the magnetic properties of  $\text{Cr}_2\text{O}_3$  using the LDA+U method. Computational techniques and the choice of the  $U$  and  $J$  parameters are explained in Section 2.2. The results are presented and discussed in Section 2.3. In particular, we calculate the exchange parameters, show that the magnetic interaction is dominated by direct exchange between Cr atoms, and find the Néel temperature using the pair cluster approximation for the quantum spin-3/2 Heisenberg model. Overall, the LDA+U method provides very good agreement with experiment for the structural and spectral properties and the Néel temperature. The results are briefly summarized in Section 2.4. Finally, the Appendix gives the technical details of the pair cluster approximation.

## 2.2 Computational details

The first-principles calculations were carried out using the projected augmented wave (PAW) method [9, 10] implemented within the Vienna *ab initio* simulation package (VASP) [11, 12]. The valence basis included  $3d$  and  $4s$  states on Cr and  $2s$  and  $2p$  states on O. We used the rhombohedral primitive cell for the corundum structure in all calculations except those involving complicated magnetic configurations (Section 2.3.1), where the hexagonal unit cell was adopted (see Fig. (2.1)). The Monkhorst-Pack scheme [13] based on the  $4 \times 4 \times 4$   $k$ -point grid was employed for the Brillouin zone integrals, which were calculated using the tetrahedron method with Blöchl corrections [14]. The cutoff energies for the plane-wave and augmentation charge were 520 and 676 eV, respectively. These parameters ensured the total energy convergence to 24 meV/atom. Densities of states (DOS) were calculated using the  $8 \times 8 \times 8$   $k$ -point grid.

We employ the LDA+U method in its full spherically symmetric form [15]. This extension is important for  $\text{Cr}_2\text{O}_3$  where correct representation of crystal field and exchange splittings within the partially filled  $3d$  shell is critical. The double-counting

term is taken in the fully localized limit. [15, 17] The underlying LDA functional of Perdew and Zunger [16] is used.

Reasonable values of  $U$  and  $J$  can usually be obtained within DFT using the constrained occupation method [18]. We calculated  $U$  and  $J$  using the full-potential linear augmented plane-wave (FLAPW) method implemented in the FLEUR package [19]. In these calculations the GGA approximation was used. We took the rhombohedral primitive cell of  $\text{Cr}_2\text{O}_3$  (see Fig. (2.1)) containing four Cr atoms and set all the structural parameters to their experimental values [20]. The  $3d$  electrons on one or two Cr sites in this cell were treated as “open core” shells, i.e. an integer occupation of these orbitals (for each spin projection) was enforced, and their hybridization with all other electrons was turned off. The  $U$  and  $J$  parameters were then found by comparing the LDA total energies for different charge and spin occupations of the  $3d$  orbital(s) with their Hartree-Fock expressions (the latter are equal to the “double-counting” terms in LDA+U).

The constrained occupation method is somewhat ambiguous because the  $U$  parameter depends on the charge state of the ion<sup>1</sup> [21]. Although the formal charge state of the chromium ion is  $\text{Cr}^{3+}$ , we find  $U$  and  $J$  with respect to the  $3d^4$  state. The reason is that the  $3d$  wave functions and the screening properties of the valence electrons depend primarily on the charge density distribution in the crystal, which is typically very close to the superposition of atomic charge densities. Indeed, the formal occupancy of the Cr  $3d$  orbital within the 2.5 a.u. muffin tin sphere is about 4.2 in FLAPW. The exchange parameter  $J = 0.58$  eV was found by treating  $3d$  electrons on one Cr atom as open core and considering the energy differences between the  $3d_{\uparrow}^2 3d_{\downarrow}^2$ ,  $3d_{\uparrow}^3 3d_{\downarrow}^1$  and  $3d_{\uparrow}^4 3d_{\downarrow}^0$  configurations. The Hubbard parameter  $U = 3.3$  eV was found by treating the  $3d$  shells on two Cr sites as open cores and considering the energy difference between the  $3d_A^4 3d_B^4$  and  $3d_A^5 3d_B^3$  configurations, where A and B refer to the two different sites<sup>2</sup>; the contribution of  $J$  to the energy differences was subtracted. Since the total number of electrons in the cell is the same for both configurations, there is no need to include the Fermi level correction. Using direct calculations of Coulomb and exchange integrals averaged over then filled molecular orbitals in the unrestricted Hartree-Fock method, Mosey *et al.* [8] obtained the values of  $U = 3.3$  eV and  $J = 0.1$  eV for  $\text{Cr}_2\text{O}_3$ . Their value of  $U - J$  is thus very close to ours, but the  $J$  value is much smaller. In the following calculations, we fixed  $J$  at its calculated value of 0.58 eV and varied  $U$  with the expectation that the optimal results should be found for  $U \sim 3 - 4$  eV.

---

<sup>1</sup>On the contrary, the  $J$  parameter is usually very well defined.

<sup>2</sup>These two sites are selected so that they are not nearest neighbors along the  $z$  axis, which makes the shortest distance between them in the crystal as large as possible.

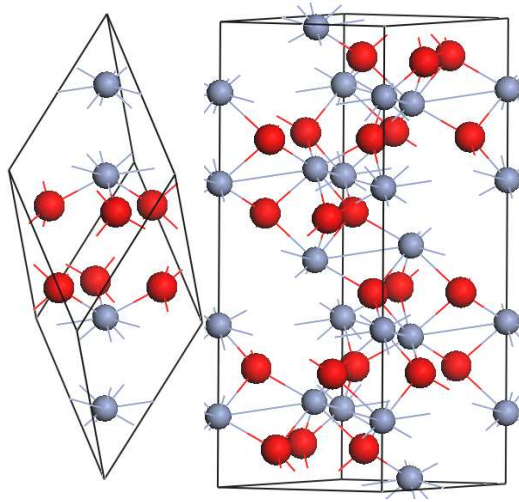


Figure 2.1: Rhombohedral primitive cell of  $\text{Cr}_2\text{O}_3$  (left) together with the hexagonal unit cell (right). Smaller gray spheres represent Cr atoms; larger red spheres display the O atoms.

## 2.3 Results and discussion

The dependence of the equilibrium volume, magnetic moment, and band gap on  $U$  for the ground antiferromagnetic state (denoted as  $+ - + -$ )<sup>3</sup> is shown in Figure 2.2. The electronic structure was calculated for relaxed structural parameters. We see that the volume and the band gap agree quite well with experimental data at  $U = 4$  eV. Other structural parameters also agree with experiment. The calculated angle between the rhombohedral unit vectors is  $55.11^\circ$  compared to the measured [20] angle of  $55.13^\circ$ . The shortest distance between Cr atoms along the  $[111]$  axis is  $2.646 \text{ \AA}$  vs the measured  $2.650 \text{ \AA}$ .

The magnetic moment at  $U = 4.0$  eV is  $2.86 \mu_B$ , i.e. it is somewhat reduced compared to the “ideal” ionic value<sup>4</sup> of  $3 \mu_B$  corresponding to a fully localized spin  $3/2$ . Experimentally, the most recent neutron polarimetry measurement gives the sublattice magnetization of  $2.48 \mu_B$  [22], which is notable lower compared to an older estimate of  $2.76 \mu_B$  [23]. The magnetic moment is smaller than  $3\mu_B$  due to two effects: (1) hybridization with oxygen, which is included in our calculation, and (2) the quantum “zero-point spin deviation”<sup>5</sup>, which is absent in DFT. The zero-point

<sup>3</sup>This notation indicates the direction of spins of the Cr atoms along the  $z$  axis (from the top to the bottom) of the rhombohedral unit cell shown in Figure 2.1a. The plus (minus) sign corresponds to spin up (down).

<sup>4</sup>Refs. [6] and [8] concluded that there is a large disagreement with experiment in the magnetic moment, but they used an incorrect experimental value of  $3.8\mu_B$ .

<sup>5</sup>This comes from the fact that the perfect antiferromagnetic order is not a ground state of the antiferromagnetic spin Hamiltonian (for example, of the Heisenberg Hamiltonian that is valid for  $\text{Cr}_2\text{O}_3$ , see below). In the real ground state there is a finite probability for direction of each

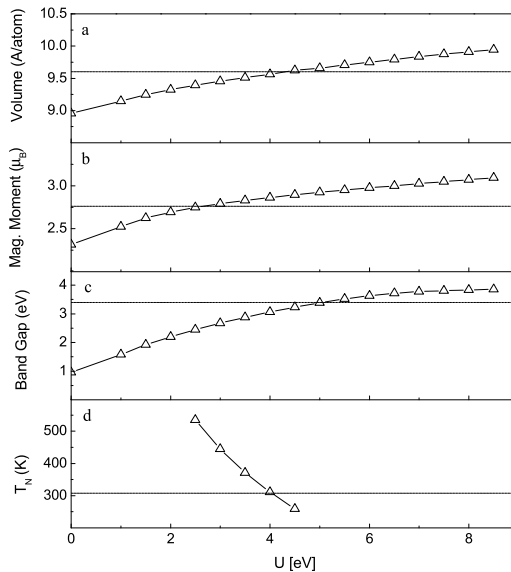


Figure 2.2: Atomic volume (a), magnetic moment (b), band gap (c) and Néel temperature (d) as functions of the Coulomb  $U$  parameter for the antiferromagnetic  $+ - + -$  state. The value of  $J$  is fixed at 0.58 eV. The horizontal lines denote experimental values; those in panel (b) are from both Refs. [22, 23].

deviation in  $\text{Cr}_2\text{O}_3$  was estimated [24] to be about 8%, which amounts to  $0.24 \mu_B$ . Thus, keeping in mind the uncertainties related to the *definition*, measurement, and calculation of the magnetic moment, its calculated value at  $U \approx 4.0$  eV is completely reasonable. Of course, the poorly defined reduction from  $3 \mu_B$  can not be used as an indicator of the quality of agreement with experiment. We also note that the local magnetic moment depends very weakly on the magnetic configuration of  $\text{Cr}_2\text{O}_3$ . In the ferromagnetic state the local moment within the muffin-tin sphere is  $2.94 \mu_B$ , while the *magnetization* is exactly equal to  $3 \mu_B$  per Cr site, as expected. The orbital moment in the calculation with spin-orbit coupling is small (about  $0.04 \mu_B$ ) and antiparallel to the spin moment, in agreement with the experimental [25]  $g$ -factor of 1.97 and with the general rule for atomic shells that are less than half filled.

The band gap of 3.07 eV is somewhat smaller than the experimental value of 3.4 eV, but greater than that found in Ref. [6] using GGA+U with  $U - J = 4$  eV. Underestimation of the addition energy is a common feature of the LDA+U method, which is well known, for example, for Gd and other  $4f$  elements. Further, the density of states shown in Figure 2.3 is in excellent agreement with X-ray photoemission data [26, 27]. Namely, the sharp and narrow peak at low binding energies separated by a (pseudo)gap from the rest of the valence band is very well reproduced. Figure 2.3 also shows the partial DOS decomposition into O and Cr contributions from  $t_{2g}$  and  $e_g$

---

spin to deviate from the perfect antiferromagnetic order even at zero temperature. These quantum fluctuations effectively reduce the value of measured local magnetic moment.

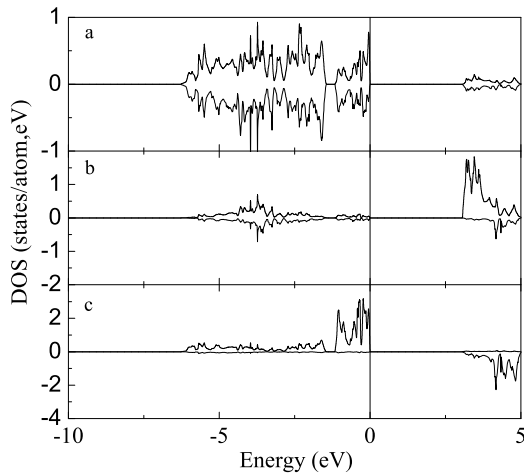


Figure 2.3: Orbital projected DOS for the antiferromagnetic  $+ - + -$  ground state of bulk  $\text{Cr}_2\text{O}_3$ , calculated within the LDA+U with  $U = 4.0$  eV,  $J = 0.58$  eV. (a) O-2p, (b) Cr- $e_g$  and (c) Cr- $t_{2g}$ . Majority and minority-spin DOS are plotted with different signs.

states<sup>6</sup>. As seen from Figure 2.3, the peak at low binding energies corresponds to the filled Cr  $t_{2g}$  spin subband with some admixture of oxygen  $p$  orbitals. At least some of this admixture is fictitious, because the Cr  $d$  orbitals extend into oxygen's projection spheres. (The same ambiguity is involved in the definition of the Cr magnetic moment.) Since non-magnetic  $\text{Cr}_2\text{O}_3$  is metallic with the Fermi level lying inside the  $t_{2g}$  subband which is separated by a gap from the oxygen  $p$  band, the insulating gap forms by the Mott-Hubbard mechanism.

Thus, the structural and spectral properties of  $\text{Cr}_2\text{O}_3$  are well reproduced by the spherically symmetric LDA+U method with  $U \approx 4.0$  eV and  $J = 0.58$  eV. This value of  $U$  is reasonably close to that given by the constrained occupation method.

### 2.3.1 Exchange parameters

We now focus on the magnetic energetics which provides another stringent test of the validity of the LDA+U method for  $\text{Cr}_2\text{O}_3$ . We calculated the total energies of 12 different magnetic configurations including the ferromagnetic state, three simple antiferromagnetic orderings ( $+ - + -$ ,  $+ + - -$ , and  $+ - - +$ ), and eight additional, arbitrarily chosen spin configurations in the hexagonal unit cell (see Figure 2.1) which contains six formula units. The ground antiferromagnetic state has  $+ - + -$  ordering in agreement with experiment; its relaxed structure was fixed for other magnetic orderings. The calculated total energies were well fitted by the conventional Heisenberg

<sup>6</sup>The  $t_{2g}$  and  $e_g$  subbands are well defined because the ligand field of the Cr site is approximately octahedral.

Table 2.1: The exchange parameters  $J_n$  fitted using the total energies of 12 magnetic configurations calculated for different values of  $U$  with  $J$  fixed at 0.58 eV. Each pair of sites contributes  $J_{ij}\mathbf{e}_i\mathbf{e}_j$  to the total energy, where  $\mathbf{e}_i$  is the unit vector parallel to the direction of the local moment at site  $i$ . The last column  $\Delta$  shows the mean-square misfit in the fitting of the total energy.  $J_n$  and  $\Delta$  are given in meV.

$U$	$J_1$	$J_2$	$J_3$	$J_4$	$J_5$	$\Delta$
2.5	-30.9	-21.9	0.60	1.83	-4.92	0.91
3.0	-23.9	-17.3	1.26	2.36	-3.72	0.62
3.5	-18.6	-13.8	1.74	2.72	-2.84	0.43
4.0	-14.6	-11.1	2.11	2.96	-2.16	0.30
4.5	-11.1	-9.04	2.41	3.11	-1.64	0.20

Hamiltonian with exchange interaction in five coordination spheres. The exchange parameters fitted by the least squares method for different values of  $U$  are listed in Table 2.1. The first, second and fifth nearest-neighbor interactions are antiferromagnetic, whereas the third and fourth ones are ferromagnetic. All exchange parameters, except the third exchange parameter, reinforce the ground state. Also, we see that the magnitudes of the first and second exchange parameters are significantly larger than those for more distant neighbors; this behavior is natural for an insulator. In  $\text{Cr}_2\text{O}_3$  the parameter  $J_1$  corresponds to the short bond along the  $z$  axis, and  $J_2$  to the nearest neighbor bond within the buckled Cr layer. Each Cr atom has one  $J_1$  neighbor and three  $J_2$  neighbors. As the value of  $U$  is increased, the magnitudes of all antiferromagnetic exchange parameters systematically decrease, while of the ferromagnetic parameters systematically increase.

Let us compare our results with those derived from the spin wave dispersion measured by inelastic neutron scattering [24]. The exchange parameters fitted to those dispersion curves are also dominated by antiferromagnetic  $J_1$  and  $J_2$ . However, more distant neighbors in that fitting [24] are much less important. For example,  $J_5/J_1 \approx 1/40$  in Ref. [24] *vs*  $1/7$  found here. Also, there is a notable disagreement in the  $J_2/J_1$  ratio: Ref. [24] found  $J_2/J_1 \approx 0.45$  versus 0.76 for  $U = 4$  eV in Table 2.1. We have verified that the anisotropy  $J_2/J_1$  is almost unchanged if only the lowest-lying spin configurations are included in the fitting.

We also considered the possibility that the exchange parameters may be affected by lattice distortions below the Néel temperature due to magneto-structural coupling. In order to study this possibility, we need to know how the exchange parameters depend on the structural parameters, and how the latter change between room temperature and liquid nitrogen temperature where the spin wave spectrum was measured. We found that the magnitudes of  $J_1$  and  $J_2$  are very sensitive to the lattice parameters; a 1% increase or decrease in the first or second neighbor bond length leads to a 25–50% decrease or increase of the magnitude of the corresponding exchange parameter (this was roughly established by varying the Bravais lattice parameters of the rhombohedral cell and fitting the four simple magnetic orderings to the Heisenberg model). Thus,

the  $J_2/J_1$  ratio is very sensitive to the  $c/a$  ratio (or any lattice distortion that changes the ratio of the first and second bond lengths  $R_2/R_1$ ).

To our knowledge, no experimental data are available on the thermal contraction of  $\text{Cr}_2\text{O}_3$  below room temperature. In order to assess the degree of magnetostructural coupling, we have fully relaxed the structure for all the 12 magnetic configurations that were included in the fitting of exchange parameters. The magnetostructural coupling is, in general, quite appreciable; the  $R_2/R_1$  ratio varies between the minimum of 1.072 in the  $+ - - +$  configuration (where the nearest-neighbor pairs are all parallel, and next-nearest antiparallel) and the maximum of 1.103 in the  $+ + --$  configuration (where the situation is reversed). The overall trend, as expected in general for antiferromagnetic coupling, is for each of these bonds to shorten when the corresponding spins are antiparallel and lengthen when they are parallel. Although this effect seems to be rather large, the actual  $+ - + -$  state has *both* first and second-neighbor pairs antiparallel, so that both should lengthen somewhat in the paramagnetic state. Among our 12 configurations, five have the same ratio  $N_P^{(i)}/N_{AP}^{(i)}$  of the number of parallel and antiparallel pairs in the  $i$ -th coordination sphere for  $i = 1$  and  $i = 2$ , i.e., these five configurations approximately represent the change of structure as a function of the antiferromagnetic order parameter. The  $R_2/R_1$  ratio for these five structures varies between 1.088 in the  $+ - + -$  state and 1.084 in the ferromagnetic state. The three intermediate states, all of which have twice as many parallel pairs than antiparallel ones, all have  $R_2/R_1 = 1.087$ . The bond lengths themselves change by about 0.7% between the  $+ - + -$  state and these three intermediate states. This variation is obviously too small to explain the disagreement with experiment in the  $J_2/J_1$  ratio.

Thus, in spite of the overall agreement with experiment for most properties, a discrepancy in the  $J_2/J_1$  ratio remains. It is possible that our Heisenberg model fitting is not fully applicable to small deviations from the ground state, for which the linear response technique should be a better fit. Further, spin waves are more sensitive to distant couplings compared to the energy fits or thermodynamic properties, which makes the fits from spin wave data and from the overall energetics statistically inequivalent. Finally, many-body effects beyond LDA+U may play a role in renormalizing the exchange parameters. We also note that impurities and thermal spin disorder should be more effective in destroying distant couplings compared to nearest-neighbor ones; this may explain the larger role of couplings beyond  $J_2$  in our fitting compared to experimental spin wave results.

### 2.3.2 Mechanism of magnetic interaction

The mechanisms of exchange interaction in  $\text{Cr}_2\text{O}_3$  are not well understood. Complicated crystal structure with the presence of many electronic orbitals of different symmetry and many Cr-O-Cr links at different angles greatly complicates the empirical analysis. Both superexchange and direct exchange interactions have been invoked to explain the magnetic structure of  $\text{Cr}_2\text{O}_3$  [28, 29, 30, 31]. Direct exchange interac-

tion may be interpreted in terms of hopping of electrons from one Cr ion to another across the insulating gap; the energy denominator involved in this process is the Mott-Hubbard splitting. The hopping can only be effective between the orbitals that are able to hybridize. From the DOS decomposition shown in Figure 2.3 it is clear that the  $t_{2g}$  orbitals very weakly hybridize with  $e_g$  orbitals on the neighboring Cr atoms. Therefore, the contribution of  $e_g$  orbitals to direct exchange can be neglected. The  $t_{2g}$  subband is split off by crystal field and exactly half-filled, therefore direct exchange should be antiferromagnetic. The superexchange involves hopping between Cr and O ions; the energy denominator involves the gap between the oxygen  $p$  states and the unoccupied Cr states.

In order to reveal the mechanism responsible for exchange interaction in  $\text{Cr}_2\text{O}_3$ , we use the following procedure. A fictitious external potential  $V$  is coupled to the oxygen  $p$  orbitals, which adds the term  $E_V = V \text{Tr} n_{mm'}^\sigma$  to the total energy, where the trace is taken over orbital and spin indices, and  $n_{mm'}^\sigma$  is the density matrix of the oxygen  $p$  states defined inside the muffin tin sphere of 1.2 a.u. This density matrix is calculated using the standard LDA+U machinery. When  $V$  is set to a negative value, the filled oxygen  $p$  states are pushed down to lower energies, which suppresses superexchange, but not direct exchange. Weak hybridization between the filled  $t_{2g}$  states and the oxygen  $p$  states pushes them apart at  $V = 0$ . When the  $p$  states are pushed down by increasing the magnitude of  $V$ , this repulsion is reduced and the  $t_{2g}$  states also move down, thereby increasing the band gap. Since direct exchange is sensitive to the band gap, for better comparison we compensate this increased band gap by reducing  $U$  on Cr. This is done in such a way that the distance between the center of mass of the filled  $t_{2g}$  band and the conduction band minimum (CBM) remains the same as at  $V = 0$ .

Starting from the state with  $U = 3.5$  eV, we added  $V$  of  $-12$  eV and  $-24$  eV and calculated the energies of four magnetic states in the rhombohedral primitive cell of  $\text{Cr}_2\text{O}_3$ . These calculations were performed using the FLAPW method [19]; the results are listed in Table 2.2<sup>7</sup>. The self-consistent downward shift of the  $p$  states is much smaller than  $Vn_{mm}$  because  $V$  is strongly screened. The distance  $\Delta$  from the oxygen  $p$  band maximum to CBM is also listed in the table.

The results listed in Table 2.2 clearly show that the magnetic energies are insensitive to the position of the oxygen  $p$  band. The reduction of magnetic energies produced by adding negative  $V$  at constant  $U$  is due to the fact that the  $t_{2g}$  band gap increases due to dehybridization from oxygen. Once  $U$  was decreased to bring the band gap to its original value, the magnetic energies were essentially unchanged compared to their values at  $V = 0$ ; in fact, they even increase somewhat. On the other hand, we've seen above that the magnetic energies are very sensitive to the value of  $U$  which is responsible for the band gap. This behavior leads us to a striking conclusion that, contrary to the common belief, superexchange plays no role in magnetism of  $\text{Cr}_2\text{O}_3$ . Antiferromagnetism is exclusively due to direct exchange, which, as

---

<sup>7</sup>Those for  $V = 0$  are within 10% of VASP results.

Table 2.2: Energies of three simple magnetic configurations relative to the ground  $+ - + -$  state (in meV per formula unit) as a function of the fictitious external potential  $V$  applied to the oxygen  $p$  orbitals (in eV). Reduced values of  $U$  on Cr compensate for the increased band gap (see text for details).  $\Delta$  is the distance from the oxygen band top to CBM in eV.

$V$	$U$	$\Delta$	++++	++--	+-+-
0	3.5	4.5	130	124	66
-12	3.5	5.8	115	102	59
-12	2.5	5.6	154	128	74
-24	3.5	7.9	102	80	51
-24	2.15	7.7	145	110	71

mentioned above, is antiferromagnetic because the magnetically active  $t_{2g}$  subband is half-filled. It is likely that superexchange in  $\text{Cr}_2\text{O}_3$  is highly ineffective because the Cr-O-Cr angles are close to  $90^\circ$ , while the overlap between O states and Cr  $t_{2g}$  states is small. On the other hand, the overlaps between  $t_{2g}$  states on neighboring Cr atoms are quite large; the  $t_{2g}$  bandwidth in the ferromagnetic state at  $V = -24$  eV is approximately 1.5 eV.

### 2.3.3 Néel temperature

We calculated the Néel temperature  $T_N$ . We saw above that the local moments on Cr atoms are well localized, and the energies of spin configurations are well represented by the Heisenberg spin Hamiltonian. We therefore adopted the quantum Heisenberg model for localized spins of magnitude  $3/2$  with the exchange parameters listed in Table 2.1. Since each spin is strongly coupled only to four neighbors (one with  $J_1$  and three with  $J_2$ ), the mean-field approximation can not be reliably used. However, the antiferromagnetic interaction is not frustrated. The important spin correlations should be generated by the dominant exchange interaction with four nearest neighbors. The network of bonds corresponding to  $J_1$  and  $J_2$  is very weakly connected; the shortest closed path on this network is 6 bonds long. Therefore, it is sufficient to capture the pairwise spin correlations. In this situation, the pair cluster approximation appears to be an obvious choice. This approach is a special case of the cluster variation method when the set of clusters includes only pairs of sites. Here we follow the formulation of Ref. [32] which can be directly applied to our case. The details of this technique are described in the Appendix.

The calculated  $T_N$  is shown in Figure 2.2 as a function of  $U$ . We see that the best agreement with experiment for  $T_N$  is obtained at the same value of  $U \approx 4$  eV as for the structural and spectral properties explored above. This overall agreement is a strong indication that the essential details of the electronic structure of  $\text{Cr}_2\text{O}_3$  are very well captured by the LDA+U approximation. Physically, this success of LDA+U is explained by the presence of fully filled and empty subbands which are

strongly split by crystal and exchange fields; LDA+U usually reproduces such closed atomic-like subshells very well.

## 2.4 Conclusion

In conclusion, we found that the spherically symmetric LDA+U method provides a very good description of structural, spectral, and magnetic properties of chromia with  $J = 0.58$  eV found from the constrained occupation method and  $U \approx 4$  eV, which is also close to the calculated value. We found that the magnetic energies are well represented by the Heisenberg model with strong exchange interaction with nearest neighbors both in the plane and along the  $z$  axis and much weaker interaction with more distant neighbors. The Néel temperature was subsequently calculated using the pair cluster approximation for the spin-3/2 quantum Heisenberg model resulting also in a very good agreement with experiment for above values of  $U$  and  $J$ . Furthermore, we found that the artificial downward shift of the filled oxygen  $p$  states has almost no effect on the magnetic energies, which proves that the direct exchange is the dominant mechanism of magnetic interaction.

## 2.A Appendix

Here we describe the application of the pair cluster approximation to  $\text{Cr}_2\text{O}_3$  following a similar formalism of Ref. [32]. The energy of a quantum Heisenberg magnet (per unit cell) can be written as

$$E = -\frac{1}{2} \sum_{i,j} m_i n_{ij} J_{ij} \langle \hat{\mathbf{S}}_i \cdot \hat{\mathbf{S}}_j \rangle - \sum_i m_i H_i \langle \hat{S}_i^z \rangle, \quad (2.1)$$

where the summations are over the inequivalent sites in the unit cell,  $\hat{\mathbf{S}}_i$  are quantum spin operators,  $m_i$  is the number of sites of type  $i$  in the unit cell,  $n_{ij}$  the number of neighbors of site  $i$  that are of type  $j$ , and  $H_i$  the external magnetic field applied to site type  $i$ . All the thermodynamic properties can be obtained from the free energy which may be calculated by integrating the Gibbs-Helmholtz relation:

$$F = \frac{1}{\beta} \int_0^\beta E(\beta') d\beta', \quad (2.2)$$

To proceed we need to find the expectation values appearing in Equation (2.1). In the pair-cluster approximation they are calculated by introducing one- and two-site clusters with the following cluster Hamiltonians:

$$\begin{aligned} \hat{\mathcal{H}}_1^i &= -h_i \hat{S}_i^z \\ \hat{\mathcal{H}}_2^{ij} &= -J_{ij} \hat{\mathbf{S}}_i \cdot \hat{\mathbf{S}}_j - h_i^{(j)} \hat{S}_i^z - h_j^{(i)} \hat{S}_j^z, \end{aligned} \quad (2.3)$$

where  $h_i = H_i + \phi_i$  is the one-site “cluster field,”  $h_i^{(j)} = h_i - \phi_i^{(j)}$  is the cluster field at site  $i$  for the pair cluster  $(i,j)$ . The one-site and two-site cluster fields are related through  $\phi_i = \sum_j n_{ij} \phi_i^{(j)}$ . The quantities  $\phi_i^{(j)}$  are treated as variational parameters and found by minimizing the free energy, i.e. requesting that  $\partial F / \partial \phi_i^{(j)} = 0$ . It can be shown that this variational condition ensures that the expectation value  $\langle \hat{S}_i^z \rangle$  is the same in all one-site and all two-site clusters containing site  $i$ . The expectation values  $\langle \hat{\mathbf{S}}_i \cdot \hat{\mathbf{S}}_j \rangle$  are calculated from the pair cluster  $(i,j)$ . Performing the integration in (2.2), we find

$$F = -\frac{1}{2\beta} \sum_{ij} m_i n_{ij} \ln Z_2^{ij} + \frac{1}{\beta} \sum_i m_i (n_i - 1) \ln Z_1^i, \quad (2.4)$$

where  $n_i = \sum_j n_{ij}$  is the total number of neighbors of site  $i$ , while  $Z_1^i = \text{Tr} \exp(-\beta \hat{\mathcal{H}}_1^i)$  and  $Z_2^{ij} = \text{Tr} \exp(-\beta \hat{\mathcal{H}}_2^{ij})$  are the one-site and two-site cluster partition sums. Evaluation of  $Z_1^i$  is trivial; to find  $Z_2^{ij}$  one first needs to diagonalize  $\hat{\mathcal{H}}_2^{ij}$ .

Our goal here is to find the transition temperature; therefore we may assume that all  $h_i^{(j)}$  are small. The free energy is developed in these parameters, and then the parameters  $\phi_i^{(j)}$  are found by requiring that the variation of the free energy  $F$  vanishes. (The resulting equations are too cumbersome to be included here.)

For  $\text{Cr}_2\text{O}_3$  we assumed the actual magnetic ordering  $+ - + -$ . All Cr sites are related by magnetic symmetry, which reduces the number of independent variational parameters. The transition temperature is found by setting  $S = 3/2$  and searching for the pole of the magnetic susceptibility which is found from the one-site cluster:

$$\chi_{ij} = \frac{\partial \langle S_i^z \rangle}{\partial H_j} = \frac{S(S+1)}{3} \beta \frac{\partial h_i}{\partial H_j}. \quad (2.5)$$

The resulting equation for the transition temperature has two solutions. The greater solution is  $T_N$ , while the lower one is the fictitious “anti-Néel point” below which  $\langle \hat{S}_i^z \rangle = 0$ . The existence of an anti-Néel point for antiferromagnets is a well-known shortcoming of the pair-cluster approximation, [33, 32] which fails at low temperatures. However, in our case the anti-Néel point is much smaller than  $T_N$  which indicates that the pair cluster approximation has a wide range of validity. Therefore, this method is expected to provide a very good approximation for  $T_N$ .

# Bibliography

- [1] P. Marcus and V. Maurice, in *Passivity of Metals and Alloys* ed. M. Schutze, Corrosion and Environmental Degradation Vol. 1 (Wiley-VCH, Weinheim, 1999).
- [2] G. C. Bond, *Heterogeneous Catalysis: Principles and Applications* (Oxford Chemistry Series, Clarendon Press, Oxford, 1974).
- [3] M. Catti, G. Sandrone, G. Valerio, and R. Dovesi, *J. Phys. Chem. Solids* **57**, 1735 (1996).
- [4] A. Y. Dobin, W. Duan, and R. M. Wentzcovitch, *Phys. Rev. B* **62**, 11997 (2000).
- [5] K. Wolter, D. Scarano, J. Fritsch, H. Kuhlenbeck, A. Zecchina, and H. -J. Freund, *Chem. Phys. Lett.* **320**, 206 (2000).
- [6] A. Rohrbach, J. Hafner, and G. Kresse, *Phys. Rev. B* **70**, 125426 (2004).
- [7] S. L. Dudarev, G. A. Botton, S. Y. Savrasov, C. J. Humphreys, and A. P. Sutton, *Phys. Rev. B* **57**, 1505 (1998).
- [8] N. J. Mosey, P. Liao, and E. A. Carter, *J. Chem. Phys.* **129**, 014103 (2008).
- [9] P. E. Blöchl, *Phys. Rev. B* **50**, 17953 (1994).
- [10] G. Kresse, and D. Joubert, *Phys. Rev. B* **59**, 1758 (1999).
- [11] G. Kresse, and J. Hafner, *Phys. Rev. B* **48**, 13115 (1993).
- [12] G. Kresse, and J. Furthmüller, *Phys. Rev. B* **54**, 11169 (1996).
- [13] H. Monkhorst, and J. D. Pack, *Phys. Rev. B* **13**, 5188 (1976).
- [14] P. E. Blöchl, O. Jepsen, and O. K. Andersen, *Phys. Rev. B* **49**, 16223 (1994).
- [15] A. I. Liechtenstein, V. I. Anisimov, and J. Zaanen, *Phys. Rev. B* **52**, R5467 (1995).
- [16] J. P. Perdew, and A. Zunger, *Phys. Rev. B* **23**, 5048 (1981)..

- [17] A. G. Petukhov, I. I. Mazin, L. Chioncel, and A. I. Lichtenstein, *Phys. Rev. B* **67**, 153106 (2003).
- [18] V. I. Anisimov and O. Gunnarsson, *Phys. Rev. B* **43**, 7570 (1991).
- [19] S. Blügel and G. Bihlmayer, in *Computational Nanoscience: Do It Yourself!*, edited by J. Grotendorst, S. Blügel, and D. Marx, John von Neumann Institute for Computing, Jülich, NIC Series, Vol. **31**, p. 85 (2006). See [www.flapw.de](http://www.flapw.de).
- [20] L. W. Finger and R. M. Hazen, *J. Appl. Phys.* **51**, 5362 (1980).
- [21] I. V. Solovyev, and P. H. Dederichs, *Phys. Rev. B* **49**, 6736 (1994).
- [22] P. J. Brown, J. B. Forsyth, E. Lelièvre-Berna, and F. Tasset, *J. Phys.: Condens. Matter* **14**, 1957 (2002).
- [23] L. M. Corliss, J. M. Hastings, R. Nathans, and G. Shirane, *J. Appl. Phys.* **36**, 1099 (1965).
- [24] E. J. Samuelsen, M. T. Hutchings, and G. Shirane, *Physica* **48**, 13 (1970).
- [25] S. Foner, *Phys. Rev.* **130**, 183 (1963).
- [26] R. Zimmermann, P. Steiner, and S. Hüfner, *J. Electron Spectrosc. Relat. Phenom.* **78**, 49 (1996).
- [27] T. Uozumi, K. Okada, A. Kotani, R. Zimmermann, P. Steiner, S. Hüfner, Y. Tezuka, and S. Shin, *J. Electron Spectrosc. Relat. Phenom.* **83**, 9 (1997).
- [28] Y. Y. Li, *Phys. Rev.* **102**, 1015 (1956).
- [29] S. Iida, *J. Phys. Soc. Japan* **11**, 1300 (1956).
- [30] J. B. Goodenough, *Phys. Rev.* **117**, 1442 (1960).
- [31] W. P. Osmond, *Proc. Phys. Soc.* **79**, 394 (1962).
- [32] V. G. Vaks and N. E. Zein, *Sov. Phys. JETP* **40**, 537, (1975).
- [33] P. W. Kasteleijn and J. van Kranendonk, *Physica* **22**, 317; 367 (1956).

## Chapter 3

# Magnetism and structural phase transitions at the $\text{Cr}_2\text{O}_3$ (0001) surface

In this chapter we continue to study the magnetism of  $\text{Cr}_2\text{O}_3$ . However here, instead of bulk as in the previous chapter, we focus on the surface. More specifically, we investigate the (0001) surface. This surface exhibits many interesting effects. In particular, the (0001) surface of  $\text{Cr}_2\text{O}_3$  has a very unique feature of having an uncompensated magnetic moment that is stable against surface roughness. This remarkable effect of  $\text{Cr}_2\text{O}_3$  is due to its special crystal and magnetic structure and makes it a very promising material for exchange bias applications. In addition, the (0001) surface of  $\text{Cr}_2\text{O}_3$  exhibits a very unusual series of structural phase transitions [1] whose nature is poorly understood. In this chapter, we use first principles electronic structure calculations to explore the thermodynamics of the surface magnetism of  $\text{Cr}_2\text{O}_3$  as well as the surface structural phase transitions. We find that there is a nontrivial coupling between these two effects that is responsible for the unusual features of the structural phase transitions.

### 3.1 Introduction

The (0001) surface of  $\text{Cr}_2\text{O}_3$  has been extensively studied both experimentally and theoretically [1-15] due to its applications as catalysts [?] and wear- and corrosion-resistant coatings [?]. It is well established that the  $\text{Cr}_2\text{O}_3$  (0001) surface is terminated with a semilayer of positively charged Cr ions [1, 2, 6, 9]. Even though this surface is polar, it doesn't lead to a divergence of the electrostatic potential. Consequently, the massive surface reconstruction, that appears for typical polar surfaces, in order to avoid the polar catastrophe (e.g. NiO [18]), is not needed here. Low-energy electron diffraction (LEED) measurements [2] together with theoretical studies [2, 9, 13] have shown that the top layer of Cr ions exhibits a significant inward relaxation. This

decreases the electrostatic energy of the polar surface and makes this termination stable.

A peculiar series of structural phase transitions on the (0001) surface of a thin film of  $\text{Cr}_2\text{O}_3$  grown on Cr substrate has been observed by means of temperature dependent LEED: at room temperature  $(1 \times 1)$  structure was observed; if the temperature is lowered, there is a phase transition to a  $(\sqrt{3} \times \sqrt{3})$  superstructure at about 150 K; if temperature is lowered further, at about 100 K we have another phase transition back to the  $(1 \times 1)$  structure [1]. Recent measurements by Takano *et. al.* [8] have shown that these transitions exist only for thin films of  $\text{Cr}_2\text{O}_3$  of about 5 nm and for films thicker than 10 nm the  $(\sqrt{3} \times \sqrt{3})$  phase is not seen. Despite some speculation [1, 5], the origin of these phase transitions remains unknown. While the first transition from  $(\sqrt{3} \times \sqrt{3})$  at 150 K to  $(1 \times 1)$  at room temperature might be, as suggested by the LEED data [1], an order-disorder transition, the second transition from the low- to the high-symmetry structure as temperature decreases is very unusual. In fact, from the ordinary knowledge of the phase transitions one usually expects a low-symmetry phase to appear at low temperatures. Clearly, the mechanism behind this transition is nontrivial.

Recently, new interesting applications of  $\text{Cr}_2\text{O}_3$  in spintronic devices have been proposed [19]. They utilize the fact that  $\text{Cr}_2\text{O}_3$  is an antiferromagnetic insulator exhibiting a magnetoelectric effect. The proposed device architectures involve magnetic tunnel junctions and spin valves in which  $\text{Cr}_2\text{O}_3$  plays a role of a tunneling barrier and a pinning layer, respectively [19]. The idea is that application of electric field leads to a net magnetization in the  $\text{Cr}_2\text{O}_3$  film that is proportional to the field. Since the magnetized  $\text{Cr}_2\text{O}_3$  film is exchange-coupled to the magnetization of the neighboring ferromagnetic layer, one can effectively control the direction of this magnetization, and therefore the magneto-resistance of the device, by applying an electric field [19]. Since the magnetoelectric effect in  $\text{Cr}_2\text{O}_3$  is rather small, very large electric fields are required to produce non-negligible effects. A different approach has been proposed by Borisov *et.al.* [20]. Here Co/Pt multilayer were grown on the (0001)  $\text{Cr}_2\text{O}_3$  and the hysteresis loop was measured after the sample was cooled down below the Néel temperature of  $\text{Cr}_2\text{O}_3$  in the simultaneous presence of electric and magnetic fields. They found that the sign of the exchange bias field depends on the direction of the electric field [20]. This effect is explained by the fact that cooling of  $\text{Cr}_2\text{O}_3$  in the presence of electric and magnetic fields favors the single antiferromagnetic domain whose structure depends on whether electric and magnetic fields are parallel or antiparallel to each other [21]. Therefore, by changing the direction of the electric field for the fixed magnetic field one chooses a particular antiferromagnetic domain. This allows for an efficient control of the antiferromagnetic interface magnetization whose sign is decisive for the exchange bias field [20]. The need of simultaneous annealing of the sample in order to switch the exchange bias field is unpractical for applications of this effect. However, recently the switching was achieved at room temperature without annealing [22].

Another interesting experiment that can trigger applications of  $\text{Cr}_2\text{O}_3$  in spintron-

ics has been recently reported by Sahoo and Binek [23]. They found that the thin film of (0001)  $\text{Cr}_2\text{O}_3$ , grown on  $\text{Al}_2\text{O}_3$  substrates, is ferromagnetic up to almost room temperature [23] but the origin of the ferromagnetism was unknown.

In this work we explored the (0001) surface of  $\text{Cr}_2\text{O}_3$  from first principles. We demonstrated that due to the unique combination of the crystal and magnetic structure of  $\text{Cr}_2\text{O}_3$  its (0001) surface possesses an uncompensated magnetic moment that persists even if the surface is rough. The magnetization was found to persist up to room temperature and is responsible for the observed ferromagnetism of the thin film of  $\text{Cr}_2\text{O}_3$  [23]. In addition, structural phase transitions at the  $\text{Cr}_2\text{O}_3$  (0001) surface were studied. We found that there was an order-disorder transition from  $(\sqrt{3} \times \sqrt{3})$  to  $(1 \times 1)$  as temperature increases due to dynamics of surface Cr atoms between two competing surface sites: above and below oxygen layer. In addition, we proposed an explanation for the low temperature phase transition observed in LEED [1, 8] as being a reentrant transition due to magneto-structural coupling.

## 3.2 Method

We investigated the (0001) surface of  $\text{Cr}_2\text{O}_3$  from first principles by means of the supercell method; we considered a symmetric slab of eight layers of  $\text{Cr}_2\text{O}_3$  that periodically repeats in the (0001) direction and is separated from its image by 15 Å of vacuum. The lateral dimensions of the supercell were fixed to the calculated bulk values [28] and ions allowed to relax. We considered the  $(1 \times 1)$ ,  $(1 \times 2)$ , and  $(\sqrt{3} \times \sqrt{3})$  surface supercells with respect to the hexagonal cell of  $\text{Cr}_2\text{O}_3$ . Electronic structure calculations are performed using the frozen-core all-electron projected augmented wave method [24], as implemented in the VASP code [25, 26]. We employed LDA+U method in its full spherically symmetric form [27] with  $J = 0.58$  eV as found from the constrained occupation calculations for bulk  $\text{Cr}_2\text{O}_3$  [28]. Two different values for the Hubbard parameter  $U$  were used:  $U = 3.5$  eV and  $U = 4$  eV. The former value is close to the  $U$  found from the constrained occupation calculations for bulk  $\text{Cr}_2\text{O}_3$  [28] while the latter value of  $U$  provides the best description of the bulk properties of  $\text{Cr}_2\text{O}_3$  [28]. The plane-wave energy cutoff was fixed to 520 eV and the Brillouin zone integration is performed using Monkhorst-Pack grids [29]. For relaxation we used a Gaussian smearing [30] of 0.2 eV and applied  $4 \times 4 \times 1$ ,  $4 \times 2 \times 1$ , and  $2 \times 2 \times 1$  k-point meshes for the  $(1 \times 1)$ ,  $(1 \times 2)$ , and  $(\sqrt{3} \times \sqrt{3})$  surface supercells, respectively. All the Hellmann-Feynman forces were converged to be less than 0.01 eV/Å. These parameters assured a total energy convergence of 0.01 meV per atom. For calculations of the density of states (DOS), we used the modified tetrahedron method [31] and  $8 \times 8 \times 1$ ,  $8 \times 4 \times 1$ , and  $4 \times 4 \times 1$  k-point meshes for the  $(1 \times 1)$ ,  $(1 \times 2)$ , and  $(\sqrt{3} \times \sqrt{3})$  surface supercells, respectively.

The energy barriers and paths for hopping of Cr ions between different surface sites were calculated using the nudged elastic band method [32]. In this approach a series of initial images between two potential minima was chosen, and each image

was only allowed to move into the direction perpendicular to the hypertangent, which was calculated as the normal vector between the two neighboring images. Hence the energy was minimized in all directions except for the direction of the reaction path. A quasi-Newton algorithm was used to relax ions until the forces in each image were less than  $0.01 \text{ eV/\AA}$

### 3.3 Surface structure

Bulk  $\text{Cr}_2\text{O}_3$  has a corundum crystal structure that is shown in the hexagonal lattice in Figure 3.1a. It can be viewed as a stacking of buckled double layers of Cr along the (0001) direction with quasi-hexagonally close-packed layers of O in between. In the Cr double layer there are three possible octahedral positions and two of them are occupied by Cr ions that form a (buckled) honeycomb lattice (see Figure 3.1b).

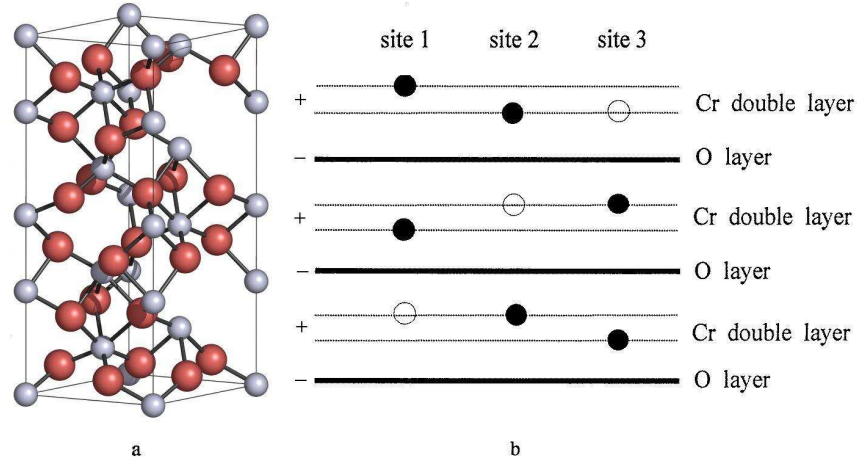


Figure 3.1: Bulk crystal structure of  $\text{Cr}_2\text{O}_3$ . (a) Hexagonal unit cell. Gray and red spheres represent Cr and O ions, respectively. (b) Schematic sideview of the crystal structure along (0001) direction. Full and empty circles denote occupied and empty octahedral sites in the Cr double layer, respectively.

Different (0001) surface terminations can be imagined. For example, the surface can be terminated with either O layer or Cr double layer. Such polar surfaces are, however, electrostatically unstable due to divergence of the electrostatic potential. In order to avoid this polar catastrophe, the surface must undergo a significant reconstruction that is however energetically expensive. From the Figure 3.1b one can envisage an alternative surface termination that cuts in the middle of double Cr layer such that only half of Cr ions from this layer remain at the surface. Even though this surface is also polar, for stoichiometric systems it doesn't lead to divergence of the electrostatic potential and thus is expected to be energetically favorable. Low energy electron diffraction (LEED) [2] and scanning tunneling microscope (STM) [6]

studies of the  $\text{Cr}_2\text{O}_3$  (0001) surface have shown that this is indeed the stable surface termination and therefore only this surface is considered here.

It is not at all clear that the surface Cr ions occupy the position corresponding to the bulk structure. In fact, the three nonequivalent sites on which surface Cr ions can reside correspond to the three different bulk octahedral sites from Figure 3.1b. The surface site corresponding to the bulk structure is denoted by A while two other surface sites are denoted by C and D (see Figure 3.2). Early quantum-chemical cluster calculations indicated that in the ground state site, C is occupied [1]. However, subsequent theoretical works showed that surface Cr ions occupy site A [2, 9]. The occupation of site A allows also for a better fit of LEED data as compared to the other two surface sites [2].

Gloege *et. al.* [5] has pointed out that there is another possible surface site in addition to A, C and D. Namely, the surface Cr ion can hop below the oxygen layer and occupy the empty octahedral site within the double layer of Cr. This interstitial site is directly underneath surface site A and we denote it by B (see Figure 3.2). It was found that the best fit of room temperature surface X-ray diffraction (SXRD) data can be obtained if we assume disordered arrangement of surface Cr ions with  $\frac{2}{3}$  probability of occupation of site A and  $\frac{1}{3}$  probability of occupation of site B [5]. This finding suggests the importance of site B in the structure of (0001) surface of  $\text{Cr}_2\text{O}_3$ .

In order to better understand the structure of the (0001) surface of  $\text{Cr}_2\text{O}_3$  we performed total energy calculations as described in Section 3.2. We focused on surface terminated with a half-layer of Cr and studied different surface models. At first, we assume that all surface Cr ions are in equivalent positions and consider occupations of sites A, B, C, and D. Figure 3.2 presents corresponding slab geometries. Note that these surface models have  $(1 \times 1)$  structure with respect to the hexagonal cell of  $\text{Cr}_2\text{O}_3$ .

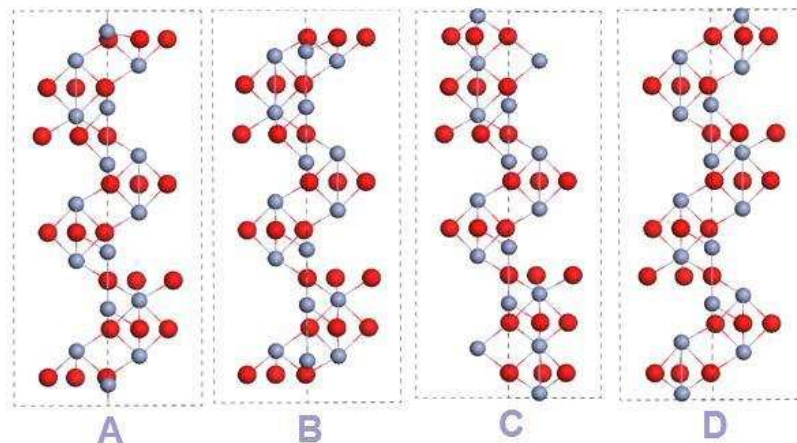


Figure 3.2: Slab geometries for four considered surface models with  $(1 \times 1)$  structure. Gray and red spheres represent Cr and O atoms, respectively.

Table 3.1: Ground state and paramagnetic surface energies for different surface models.

Model	$E_s$ [eV]		
	ground state		paramagnetic state
	$U = 3.5$ eV	$U = 4$ eV	$U = 3.5$ eV
A	2.8755	2.9065	2.9748
B	2.9793	3.0149	3.1203
C	5.7471	5.8434	
D	4.9507	4.9992	
AB	2.8177	2.8550	2.9161
AAB	2.8113	2.8431	2.9101
ABB	2.8387	2.8775	2.9368

A useful quantity for characterizing the surface stability is the surface energy that we define as

$$E_s = \frac{1}{2} \left( E_{slab} - \frac{N_{slab}}{N_{bulk}} E_{bulk} \right) / N \quad (3.1)$$

Here  $N$  is the number of surface Cr ions at one side of the slab,  $E_{slab}$  and  $E_{bulk}$  are the total energies of the slab and a bulk cell, respectively;  $N_{slab}$  and  $N_{bulk}$  are the number of atoms in the slab and the bulk cell, respectively. Surface energies calculated for ground state magnetic configuration for each surface model<sup>1</sup> are presented in Table 3.1. In general, surface energies for  $U = 4$  eV are slightly higher than for  $U = 3.5$  eV but the overall trend is the same for both values of  $U$ .

The lowest surface energy among  $(1 \times 1)$  structures is for model A. Models C and D have much higher surface energies so the corresponding surface sites can be excluded from subsequent analysis. This is in agreement with [2, 9]. However, we find that the surface energy of model B is only slightly higher than the one from model A. We have therefore two competing surface sites and it is natural to expect that surface energy can be lowered if some surface Cr atoms occupy site A and some B sites. Note that in this case surface Cr atoms form a triangular lattice and at each site of the lattice Cr ion can be either above (site A) or below (site B) the O layer. We consider different surface supercells containing more than one surface Cr ion. In particular, we calculated surface energies for AB, AAB, and ABB surface models (see Figure 3.3). The first model has two surface Cr ions in the surface supercell; one in position A and the other one in position B. This model has  $(2 \times 1)$  structure. The other two models have  $(\sqrt{3} \times \sqrt{3})$  structure and three surface Cr ions in the surface supercell; AAB model has two atoms at site A and one atom at site B while ABB model has one atom at site A and two atoms at site B. As seen from Table 3.1, surface superstructures have in general lower surface energies than model A. This can

<sup>1</sup>The bulk-like antiferromagnetic spin configuration was found to be the ground state for each surface model except for model B for which the lowest energy is for the ferromagnetic arrangement of three closest to the surface atomic layers of Cr (see Section 3.6).

Table 3.2: Surface relaxation for surface models A and B. The relaxations for first seven atomic layers are given in % of the bulk interlayer distances.  $M(n)$  denotes  $n$ th layer from the surface with M being the type of atom in the layer.

	A		B	
	$U = 3.5$ eV	$U = 4$ eV	$U = 3.5$ eV	$U = 4$ eV
Cr(1)-O(2)	-56.1	-56.3	-182.6	-190.0
O(2)-Cr(3)	+7.0	+7.3	-13.2	-13.0
Cr(3)-Cr(4)	-41.1	-41.3	-25.8	-25.9
Cr(4)-O(5)	+10.4	+10.8	+17.4	+17.5
O(5)-Cr(6)	+0.7	+0.7	+16.1	+16.6
Cr(6)-Cr(7)	-2.7	-2.2	-40.9	-42.2
Cr(7)-O(8)	+0.7	0.6	+9.0	+9.6

be understood from purely electrostatic considerations since putting some surface Cr ions below the oxygen layer partly deals with the energetically unfavorable situation of an array of positively charged Cr ions located at the surface. In particular, the Coulomb energy is minimized for the  $(\sqrt{3} \times \sqrt{3})$  ordering. Since from the total energy calculations of  $(1 \times 1)$  structures we found that locally site A is more favorable than B, we can expect that AAB is the most favorable ordering. As seen from Table 3.1, this is indeed the case and AAB model has the lowest surface energy. While it is in principle possible that some more complicated ordering of surface Cr atoms can have lower energy than AAB model, this situation is very unlikely since, as we know from the theory of ordering in alloys, the ground state is usually for high symmetry structures. Therefore, we conclude that AAB structure is the ground state.

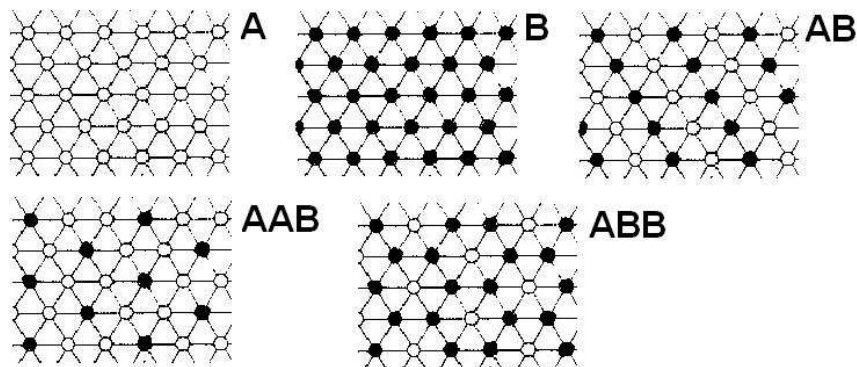


Figure 3.3: Different orderings of surface Cr.

The changes in the interlayer distances of the relaxed slabs for models A and B are presented in Table 3.2. For model A we observe a significant inward relaxation of the surface Cr ions in agreement with other theoretical predictions [2, 9, 13, 15]. This is an expected behavior because there is no negatively charged oxygen layer above

the surface so the surface Cr ions are electrostatically attracted into the surface. The strong inward relaxation of the surface Cr ions significantly decreases the Coulomb energy of the polar surface leading to the surface energy similar to that of nonpolar surfaces. As mentioned above, for the AAB model the Coulomb energy is already strongly decreased by putting  $\frac{1}{3}$  of surface Cr ions below the O layer and therefore one doesn't expect such strong relaxations of surface Cr ions being in position A. Indeed, for the two Cr ions occupying site A we found smaller inward relaxation of 49% and 47%. For model B the surface Cr ion is below the O layer. This reconstruction leads to the surface region extended up to the sixth atomic layer of Cr as opposed to model A where surface extends only up to the third atomic layer of Cr.

### 3.4 Structural surface thermodynamics

In the previous section we found that there are two competing surface sites: A and B. For the ground state surface model (AAB) we calculated the energy profile for hopping of the surface Cr ions between sites A and B along the (0001) direction using the method described in Section 3.2 (see Figure 3.4). We found a reasonable agreement between two values of  $U$ ; the energy barrier for the hopping,  $E_b$ , is 0.3 eV and 0.26 eV for  $U = 3.5$  eV and  $U = 4$  eV, respectively. This result can be used to estimate the frequency of thermally activated hopping between sites A and B

$$\gamma \sim \gamma_0 e^{-\frac{E_b}{k_B T}} \quad (3.2)$$

Here  $\gamma_0$  is the attempt frequency that is of the order of a typical phonon frequency ( $10^{13} \text{ s}^{-1}$ ). It follows that at the room temperature the characteristic hopping time is of the order of  $10^{-8}$  s. On the other hand, the blocking temperature, below which the hopping is essentially frozen, is about 100 K. For temperatures above the blocking temperature we can thus expect that the surface reaches the thermodynamic equilibrium with respect to the occupations of sites A and B on the time scale of typical experiments. In order to investigate the equilibrium surface structure at finite temperatures we introduce a configurational Hamiltonian

$$\mathcal{H} = V_{int}(\{s_i\}) - h \sum_i s_i \quad (3.3)$$

Here  $s_i$  is the Ising variable of the  $i$ th site of the triangular lattice. If the surface Cr ion at site  $i$  is at position A (B) then  $s_i$  is equal to +1 (-1). The first term is responsible for interaction between surface Cr ions and the second term describes the local preference for the occupation of surface sites. Since the surface energy for model A is lower than for model B, locally occupation of site A is preferable and  $h$  is positive. In order to proceed we need to assume some particular form of  $V_{int}(\{s_i\})$  and then fit the Hamiltonian to the surface energies of different surface supercells. Due to large size of the system the calculations are feasible only for relatively small supercells and

consequently we are restricted to rather simple (i.e. with not too many parameters) forms of  $V_{int}(\{s_i\})$ . We consider two alternative models. In the first model we simply assume that  $V_{int}(\{s_i\})$  contains only two-body interactions with first two shells of neighbors. From Equation (3.3) we then obtain Ising-like Hamiltonian

$$\mathcal{H} = -\frac{1}{2} \sum_{ij} J_{ij} s_i s_j - h \sum_i s_i \quad (3.4)$$

where exchange constants  $J_{ij}$  are equal to  $J_1$  for nearest neighbors,  $J_2$  for next nearest neighbors, and 0 otherwise. This two-exchange model contains three parameters ( $J_1, J_2, h$ ) that were found by fitting the surface energies from Table 3.1 to Hamiltonian (3.4). In order to analyze the effect of magnetic order on the structural thermodynamics, we used both ground state and paramagnetic (see Section 3.6) surface energies. The results are presented in Table 3.3. For the ground state a reasonable fit was obtained for both values of  $U$ . On the other hand, for the paramagnetic state the quality of fit is much worse resulting in large uncertainties of parameters. For both values of  $U$  the parameters are similar. The parameter  $h$  is positive which reflects the fact that model A has a lower surface energy than model B. Interestingly, in the paramagnetic state  $h$  is larger indicating that magnetism favors occupation of site B. The first exchange constant,  $J_1$  is strong and negative; it prefers nearest neighbors to occupy the opposite surface sites. Since the surface Cr ions lie on the triangular lattice, it leads to frustration. For the ground state the second exchange constant,  $J_2$  is also negative but it is significantly weaker than  $J_1$ ; for  $U = 3.5$  the magnitude of  $J_2$  is of the order of its uncertainty. For the paramagnetic state the fitted value of  $J_2$  is also negative but its magnitude is smaller than its uncertainty. The large relative uncertainty of  $J_2$  introduces a problem in studying the thermodynamics since, as shown below, the results are very sensitive to  $J_2$  despite its smallness.

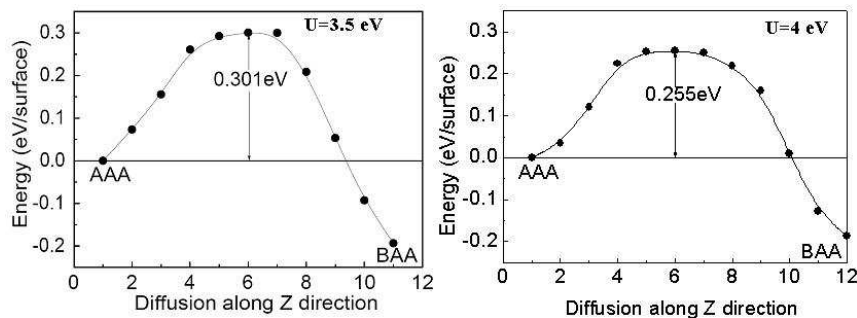


Figure 3.4: The energy profile for hopping of surface Cr atom between site A and B along (0001) for AAB model.

In the second model we found the specific form of  $V_{int}(\{s_i\})$  based on physical arguments. As discussed in the previous section, most of characteristics of the (0001)

Table 3.3: Parameters for the two-exchange model obtained from the ground state paramagnetic surface energies.  $\Delta$  is the mean-square misfit of the fitting. The estimate of the transition temperature for order-disorder transition is also given.

	ground state		paramagnetic state
	$U = 3.5$ eV	$U = 4$ eV	$U = 3.5$ eV
$h$ [eV]	$0.0509 \pm 0.0032$	$0.0539 \pm 0.0008$	$0.0695 \pm 0.0098$
$J_1$ [eV]	$-0.0256 \pm 0.0012$	$-0.0251 \pm 0.0003$	$-0.0310 \pm 0.0037$
$J_2$ [eV]	$-0.0018 \pm 0.0014$	$-0.0013 \pm 0.0004$	$-0.0018 \pm 0.0045$
$\Delta$ [eV]	0.0047	0.0012	0.0146
$J'_1$	$-0.5039 \pm 0.0388$	$-0.4653 \pm 0.0086$	$-0.4465 \pm 0.0821$
$J'_2$	$-0.0354 \pm 0.0284$	$-0.0246 \pm 0.0066$	$-0.0264 \pm 0.0646$
$T_c$ [K]	150 – 350	270 – 320	0 – 680

surface of  $\text{Cr}_2\text{O}_3$  can be explained just from electrostatics. It is therefore reasonable to assume that interaction between the surface Cr atoms is purely electrostatic in origin. In the electrostatic model, we consider an array of point charges  $q$  (measured in units of the proton charge  $e$ ) located at the sites of a triangular lattice with the same lattice parameter as for surface Cr ions. The vertical coordinate of the point charge at site  $i$  can be either 0 or  $-z$ . The corresponding Ising variable  $s_i$  takes value  $+1$  and  $-1$  in the former and latter case, respectively. The value of  $z$  is the difference in the vertical coordinate of sites A and B as found from relaxation data for surface model AAB. We then assume that  $V_{int}(\{s_i\})$  is equal to the Madelung energy of this system scaled by a dielectric constant  $\epsilon$  that represents the screening that is absent in the electrostatic model but is included in the *ab initio* calculations.

$$V_{int}(\{s_i\}) = \frac{E_{MAD}(\{s_i\})}{\epsilon} \quad (3.5)$$

The Madelung energy may be written as

$$E_{MAD}(\{s_i\}) = \frac{1}{2}q^2 \sum_{ij} \frac{1}{|\mathbf{R}_i(s_i) - \mathbf{R}_j(s_j)|} \equiv -\frac{1}{2}\epsilon \sum_{ij} J_{ij}s_i s_j + const \quad (3.6)$$

Here  $\mathbf{R}_i(s_i)$  is the position vector of the point charge at site  $i$ . Thus, Hamiltonian (3.3) again takes the Ising-like form of Equation (3.4). Here, however, exchange parameters  $J_{ij}$ 's are defined by Equation (3.6) and can be found by noting that  $|\mathbf{R}_i(s_i) - \mathbf{R}_j(s_j)| = d_{ij}$  for  $s_i = s_j$  and  $|\mathbf{R}_i(s_i) - \mathbf{R}_j(s_j)| = \sqrt{d_{ij}^2 + z^2}$  for  $s_i = -s_j$

Table 3.4: Parameters for the electrostatic model obtained from the ground state and paramagnetic surface energies.  $\Delta$  is the mean-square misfit of the fitting. The estimate of the transition temperature for order-disorder transition is also given.

	ground state		paramagnetic state
	$U = 3.5$ eV	$U = 4$ eV	$U = 3.5$ eV
$h$ [eV]	$0.0509 \pm 0.0032$	$0.0536 \pm 0.0008$	$0.0695 \pm 0.0098$
$\frac{q^2}{\epsilon}$ [e <sup>2</sup> ]	$0.3492 \pm 0.0146$	$0.3380 \pm 0.0082$	$0.4211 \pm 0.0450$
$\Delta$ [eV]	0.0048	0.0027	0.0148
$\alpha$	$0.1996 \pm 0.0152$	$0.2174 \pm 0.0090$	$0.2262 \pm 0.0404$
$T_c$ [K]	100 – 150	130 – 170	140 – 180

where  $d_{ij}$  is the in-plane distance between sites  $i$  and  $j$ . Thus we obtain

$$J_{ij} = -\frac{q^2}{4\epsilon} \frac{2}{d_{ij}} \left[ 1 - \frac{1}{\sqrt{1 + \left(\frac{z}{d_{ij}}\right)^2}} \right] \quad (3.7)$$

For distant neighbors for which  $d_{ij} \gg z$  we obtain an asymptotic dipolar form

$$J_{ij} = -\frac{q^2}{4\epsilon} \frac{z^2}{d_{ij}^3} \quad (3.8)$$

The electrostatic model contains just two parameters:  $h$  and  $\frac{q^2}{\epsilon}$ . Similarly as in the case of the two-exchange model the parameters can be found by fitting the ground state and paramagnetic surface energies to Equation (3.4). The values of fitted parameters are given in the Table 3.4. The quality of fit is comparable to the two-exchange model even though we have one parameter less. The parameter  $h$  is exactly the same as in the two-exchange model since it describes a local site preference and it doesn't depend on the form of the interaction between the surface Cr ions.

For each model by setting the convenient scale for the temperature we can effectively reduce the number of free parameters by one. For the two-exchange model we have then two parameters:  $J'_1 = J_1/h$  and  $J'_2 = J_2/h$ , while for the electrostatic model we have just one parameter which we define as  $\alpha = \frac{4a\epsilon h}{(qe)^2}$  where  $a$  is the in-plane lattice constant. The values of these parameters are given in Tables 3.3 and 3.4.

Before studying thermodynamics it is instructive to analyze the possible ground states for each model. In Refs. [33, 34] the ground state analysis for the two-exchange model was performed and the resulting phase diagram is shown in Figure 3.5. Among possible ground states for the two-exchange models we have A, AB, AAB surface models, the complex AAAB phase with  $(2 \times 2)$  structure, and two other orderings denoted as I and II [33, 34] that are not considered here. For  $J'_1$  and  $J'_2$  found from ground state surface energies we are in the AAB region but close to the boundaries

with AB and AAAB phases. However, for the paramagnetic state, due to large relative uncertainty of  $J'_2$ , in addition to AAAB we can be as well in AB or even in AAAB regions.

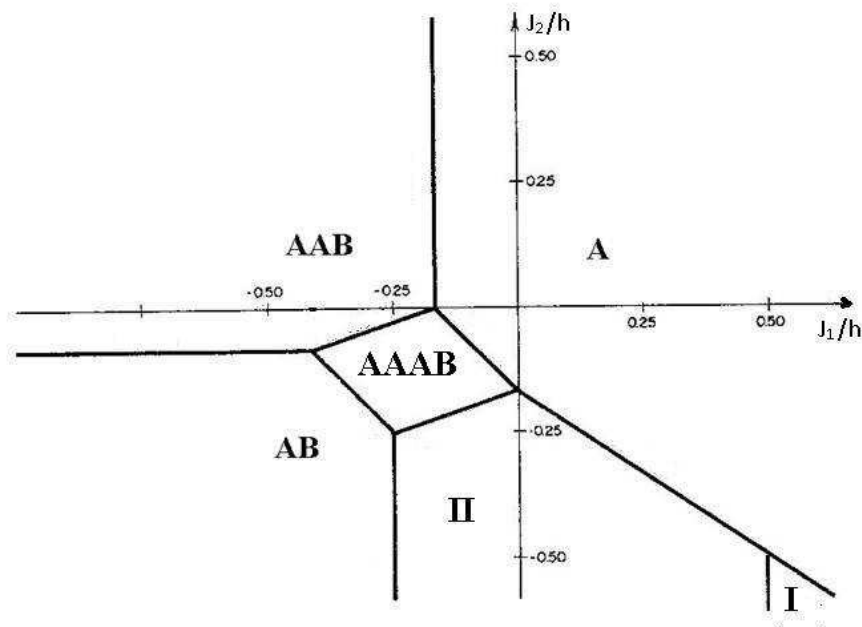


Figure 3.5: The ground state phase diagram of the two-exchange model. Adapted from Refs. [33, 34].

For the electrostatic model there is no available ground state phase diagram which, in fact, would be difficult to obtain due to long-range interaction of the model. However, it is reasonable to consider only the phases appearing in the two-exchange model as possible ground state structures. Making this assumption we found that the ground state was AB for  $\alpha$  smaller than 0.11, AAB for  $\alpha \in (0.11, 0.46)$ , AAAB for  $\alpha \in (0.46, 0.67)$ , and A for  $\alpha$  larger than 0.67. As seen from Table 3.4, the fitted values of  $\alpha$  correspond to the AAB ground state.

For both the two-exchange and electrostatic models, the configurational Hamiltonian has the Ising-like form (see Equation (3.4)). Since the lattice is triangular and in both cases the first exchange constant is negative, we expect strong frustration. Consequently, mean-field-like approaches are inapplicable and we studied the thermodynamics using the Monte Carlo method. In the two-exchange model the interaction has a finite range and therefore conventional Monte Carlo in real space can be used. On the other hand, for the electrostatic model we have a long range interaction decaying as a power law and it is not clear where it should be cutoff. Therefore, in this case we use Monte Carlo method in the Fourier space. The details of Monte Carlo simulations are described in Section 1.2.

In order to define the order parameter for the AAB model with  $(\sqrt{3} \times \sqrt{3})$  struc-

ture we decompose the original triangular lattice into three interpenetrating (also triangular) sublattices made of sites connected by next nearest neighbors bonds. We define the magnetization of sublattice  $\alpha$  by

$$M_\alpha = \frac{3}{N} \sum_{i \in \alpha} s_i \quad (3.9)$$

where  $N$  is the total number of sites. AAB ordering corresponds to negative magnetization of one sublattice and positive magnetization of two other sublattices. Since all three sublattices are equivalent, we have threefold degeneracy. For each of these three AAB orderings we can define order parameter that changes from 1 at zero temperature to 0 in the disordered state.

$$m_1 = \left( \frac{M_2 + M_3}{2} - M_1 \right) / 2 \quad (3.10)$$

$$m_2 = \left( \frac{M_1 + M_3}{2} - M_2 \right) / 2 \quad (3.11)$$

$$m_3 = \left( \frac{M_1 + M_2}{2} - M_3 \right) / 2 \quad (3.12)$$

During the Monte Carlo simulations the system can go from one AAB orderings to other. We therefore define a square root order parameter that remains the same as the system switches between degenerate orderings.

$$\eta = \frac{\sqrt{6}}{3} \sqrt{m_1^2 + m_2^2 + m_3^2} \quad (3.13)$$

Correspondingly, we define the susceptibility of the order parameter that has a peak at the transition temperature

$$\chi = \frac{1}{Nk_B T} (\langle \eta^2 \rangle - \langle \eta \rangle^2) \quad (3.14)$$

and the fourth order cumulant

$$U_\eta = 1 - \frac{\langle \eta^4 \rangle}{3 \langle \eta^2 \rangle^2} \quad (3.15)$$

From the Monte Carlo simulations for the two-exchange and electrostatic models we found that there is a second order phase transition from the ordered ( $\sqrt{3} \times \sqrt{3}$ ) superstructure of AAB model to disordered ( $1 \times 1$ ) structure in which Cr ions randomly occupy surface sites A or B. In the wide range of temperatures around the room temperature the probability of occupation of site B is 0.35 – 0.4. The disordered state is in a good agreement with the room temperature X-ray diffraction data [5] and was not seen in the scanning tunneling microscope studies [6] due to very short

hopping time at the room temperature. This phase transition was postulated earlier by Gloege *et. al.* [5] to explain the high-temperature phase transition observed in LEED [1].

The transition temperature was found using the fourth order cumulant method (see Section 1.2). For the two-exchange model the transition temperature decreases as the magnitude of either  $J'_1$  or  $J'_2$  increases. However, we found that the value of the transition temperature is very sensitive to even small changes in  $J'_2$ . In particular, the uncertainty of  $J'_2$  leads to huge uncertainties of the transition temperature, as seen in Tables 3.3. This strong dependence of the transition temperature on the value of  $J'_2$  is due to proximity of the phase boundaries to the AB and AAAB ground state ordering. Note that for the paramagnetic state this phase transition may even not occur since, as mentioned above due to uncertainty of  $J'_2$ , the AAB structure may not be a ground state.

Within the electrostatic model, the dependence of the transition temperature on  $\alpha$  is shown in Figure 3.6. As seen, in the region of fitted values of  $\alpha$ , the dependence is smooth. For lower values of  $\alpha$ , the transition temperature strongly decreases with  $\alpha$  since the system gets closer to the ground state phase boundary. In particular, for  $\alpha = 0.11$  the transition temperature is 0 and for even lower values of  $\alpha$  the AB ordering appears.

Transition temperatures for the electrostatic model for the ground and paramagnetic states are given in Table 3.4. The values of transition temperatures are similar to the transition temperature of the  $(\sqrt{3} \times \sqrt{3})$  to  $(1 \times 1)$  phase transition observed in LEED [1]. Note, however, that in Ref. [1] the measurements were done on the thin film of  $\text{Cr}_2\text{O}_3$  grown on Cr substrate. Thus, the value of  $\alpha$  and transition temperature may be different than for the surface of the single crystal of  $\text{Cr}_2\text{O}_3$  that is considered here. In particular, the fact that in the Ref. [8] the  $(\sqrt{3} \times \sqrt{3})$  structure was not seen for the 10 nm film of  $\text{Cr}_2\text{O}_3$  can be caused by the fact that in this case  $\alpha$  is smaller than for thinner films and therefore the transition temperature is below the considered range of temperatures.

Overall, the electrostatic model seems to be more appropriate for studying the structural thermodynamics of the (0001) surface of  $\text{Cr}_2\text{O}_3$ . Its main advantage lies in the fact that, on contrary to the two-exchange model, it was derived based on physical considerations. The assumption that electrostatics alone is responsible for the interaction between surface Cr atoms seems to be justified since a very good fit was obtained despite the fact that the model contains just two parameters. This last feature makes interpretation of thermodynamics for the electrostatic model much simpler. On the other hand, the instability of the transition temperature with respect to small changes of  $J'_2$  makes the two-exchange model unsuitable for determination of transition temperature.

Finally, let us discuss the possible mechanism for the low-temperature phase transition from  $(1 \times 1)$  to  $(\sqrt{3} \times \sqrt{3})$  observed in LEED [1]. As emphasized above, since the LEED measurements were made for the thin film of  $\text{Cr}_2\text{O}_3$  grown on Cr substrate [1] rather than on the surface of a single crystal of  $\text{Cr}_2\text{O}_3$ , the value of  $\alpha$  may be

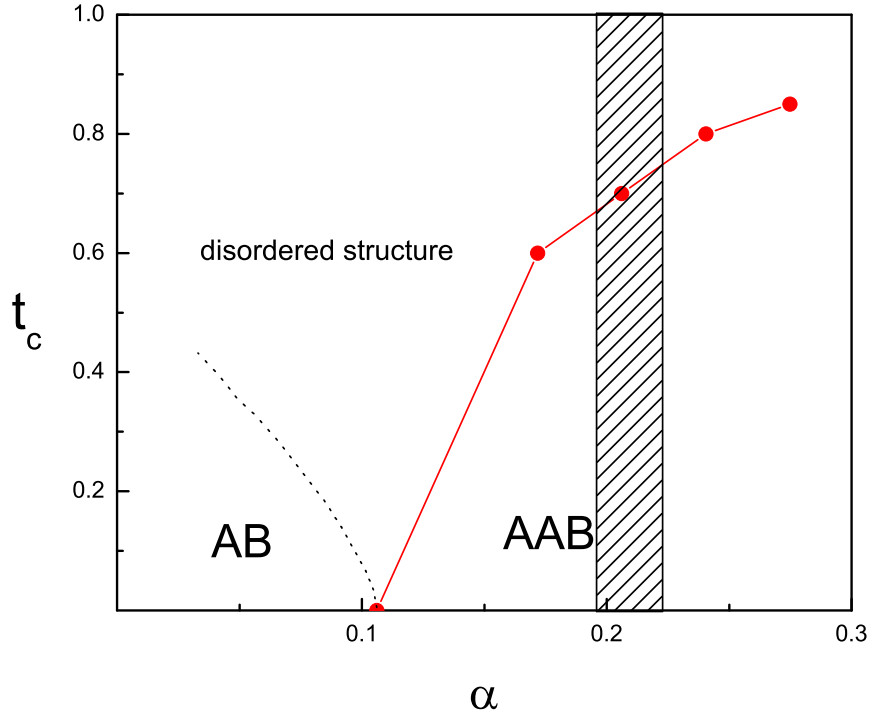


Figure 3.6: The phase diagram for the electrostatic model. The red line shows the reduced transition temperature ( $t_c = \frac{k_B T_c}{|J_1|}$ ) of the phase transition from the AAB ordering to the disordered structure for the electrostatic model as a function of  $\alpha$ . The patterned rectangular shows schematically the values of  $\alpha$  found by fitting. The dashed line shows schematically the boundary between AB structure and disordered state.

different. The existence of the low-temperature phase transition may be explained if we assume that  $\alpha$  for the thin film is slightly above 0.11. In this case even though the ground state is still AAB with  $(\sqrt{3} \times \sqrt{3})$  structure, it undergoes a phase transition to the disordered  $(1 \times 1)$  structure already for very small temperatures. As we increase the temperature further the magnetic disorder is introduced which, as seen from Table 3.4, increases the value of  $\alpha$ . We propose that this increase of  $\alpha$  causes a reentrant transition back to the  $(\sqrt{3} \times \sqrt{3})$  phase that is observed experimentally [1]. Note that similar mechanism may be formulated for the two-exchange model. If we assume that  $J'_2$  for the thin film is close to the phase boundary to AB or AAAB phase, then the disordered  $(1 \times 1)$  structure appears already for small temperatures. Further increase of temperature leads to magnetic disorder that decreases the magnitude of  $J'_2$  (see Table 3.3) and can cause reentrant transition to the  $(\sqrt{3} \times \sqrt{3})$  phase. Low temperature LEED measurement of the (0001) surface of the single crystal and thin films of  $\text{Cr}_2\text{O}_3$  are desirable to confirm this scenario.

### 3.5 Surface electronic structure

In order to analyze the electronic properties of the (0001) surface of  $\text{Cr}_2\text{O}_3$ , we calculated the partial density of states (DOS) for surface Cr ions for the AAB model. We found that all features of DOS are similar for both values of  $U$ . In Figure 3.7 we show DOS of the  $d$  orbitals for surface Cr ions in positions A<sup>2</sup> and B, as well as for Cr ion in the center of the slab for  $U = 3.5$  eV. The DOS for Cr ion in the middle of the slab agrees with the corresponding DOS for bulk  $\text{Cr}_2\text{O}_3$  (see Section 2.3). This confirms that in the middle of the slab the system is bulk-like. For both types of surface Cr ions valence and conduction majority  $d$  bands enter the bulk gap forming spin polarized surface states. This leads to decrease of the band gap at the surface to 1.70 eV and 1.85 eV for  $U = 3.5$  eV and  $U = 4$  eV, respectively. The bulk band gap is 2.80 eV and 3.04 eV for  $U = 3.5$  eV and  $U = 4$  eV, respectively (see Section 2.3). On the other hand, the exchange splitting at the surface is similar to the bulk case.

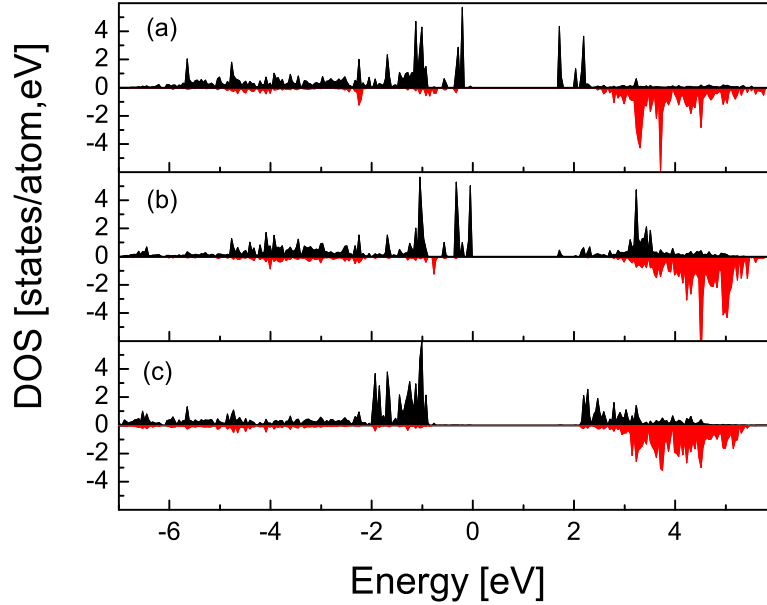


Figure 3.7: DOS for Cr  $d$  states for  $U = 3.5$  eV. (a) for surface Cr ion at position A, (b) for surface Cr ion at position B, (c) for bulk-like Cr ion in the middle of the slab. Majority and minority-spin DOS are plotted with different signs.

---

<sup>2</sup>For AAB model there are two different surface Cr ions in position A but their DOSs are very similar.

### 3.6 Surface magnetism

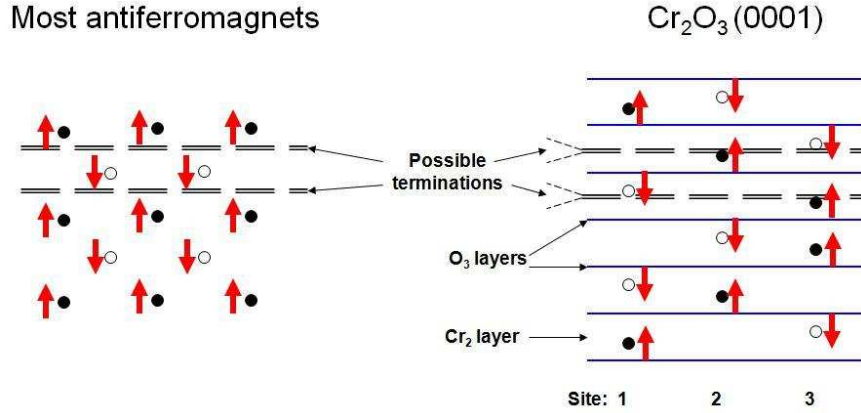


Figure 3.8: The comparison of magnetic structures of the (0001) surface of  $\text{Cr}_2\text{O}_3$  and surfaces of most antiferromagnets. Full and empty back circles denote magnetic ions with spin up and down, respectively.

As emphasized in the Introduction, the (0001) surface of  $\text{Cr}_2\text{O}_3$  has very unique magnetic properties. Namely,  $\text{Cr}_2\text{O}_3$  possesses an uncompensated magnetic moment that, unlike other known antiferromagnet surfaces, is stable against surface roughness. This feature is illustrated in Figure 3.8 where we compare magnetic structures at the (0001) surface of  $\text{Cr}_2\text{O}_3$  and at surfaces of most antiferromagnets. As seen in Figure 3.8, for most antiferromagnets (e.g. NiO) there are two possible equivalent surface terminations. Depending on the termination we have at the surface an uncompensated magnetic moment either up or down. In the ideal case we have thus a surface magnetization. However, in reality we have surface roughness and therefore there are areas of the surface with magnetic moments up and with magnetic moments down. Since both terminations are equally probable, on average surface magnetization disappears - it is destroyed by roughness. On the other hand, for the  $\text{Cr}_2\text{O}_3$  (0001) surface the stable surface terminations are in the middle of double Cr layer. Therefore, for a single domain  $\text{Cr}_2\text{O}_3$  (0001) surface, no matter where we terminate the surface, the direction of the magnetic moment is the same (see Figure 3.8). Consequently, we have a surface magnetism even for a rough surface.

The above discussion is based on the idealized picture in which we assume that surface atoms behave as for bulk. As discussed in the previous sections however, both atomic and electronic structure changes significantly at the surface. Therefore, in order to check the above prediction, we studied the surface magnetism of the (0001) surface of  $\text{Cr}_2\text{O}_3$  using first principles calculations. Since in the previous section we obtained similar results for two different choices of  $U$ , in this section we use only  $U = 3.5$  eV.

The magnitude of the local magnetic moment for three closest to the surface

Table 3.5: Magnetic moment per Cr atom for three closest the surface atomic layers of Cr for different surface models.  $M(n)$  denotes  $n$ th layer from the surface with M being the type of atom in the layer. The unit is  $\mu_B$

	A	B	AAB
Cr(1)	2.829	2.828	2.795
Cr(3)	2.772	2.848	2.743
Cr(4)	2.841	2.901	2.837

atomic layers of Cr for different surface models are shown in Table 3.5. As seen, moments are close to  $3\mu_B$  as expected from the ionic picture. We found that the bulk-like antiferromagnetic spin structure has the lowest energy for all surface models except for model B for which the lowest energy has the state with the ferromagnetic arrangement of three closest to the surface atomic layers of Cr. Therefore, for each surface model there is a surface magnetization that is stable against surface roughness and for model B the magnitude of the magnetization is about three times larger than expected. As discussed in Section 3.4, as temperature increases we have a phase transition from the ground state ( $\sqrt{3} \times \sqrt{3}$ ) phase to the disordered ( $1 \times 1$ ) structure where surface Cr ions sits either in the position A or B with approximate probabilities  $\frac{2}{3}$  and  $\frac{1}{3}$ , respectively. Based on the results for each surface model we expect that the lowest energy for this disordered structure is also for the bulk-like antiferromagnetic spin arrangement. Therefore, in agreement with above predictions, the (0001) surface of  $\text{Cr}_2\text{O}_3$  has a surface magnetization that is stable against roughness.

The knowledge of the temperature dependence of the surface magnetization is of great importance. In particular, if the surface Cr ions are only weakly magnetically coupled to the bulk, the thermal fluctuations can destroy the surface magnetism already at low temperatures. In order to study magnetic thermodynamics we calculated surface magnetic energies for surface models A and B for eight different spin configurations of three closest to the surface atomic layers of  $\text{Cr}^3$ . The magnetic energies were fitted to the Heisenberg Hamiltonian

$$\mathcal{H} = -\frac{1}{2} \sum_{i,j} J_{ij} \mathbf{S}_i \cdot \mathbf{S}_j - \sum_i H_i S_i^z + Nc \quad (3.16)$$

Here  $N$  is the number of surface Cr atoms and  $c$  is a constant that in the mean-field approximation has a meaning of the paramagnetic surface energy. The summation in Equation (3.16) runs over the Cr atoms in the three sites closest to the surface layer. For ( $1 \times 1$ ) structures (models A and B), we have three nonequivalent Cr atoms: the surface Cr atom, the upper, and the lower Cr atoms from the Cr double layer below the surface. They are denoted as 1, 2, and 3, respectively. We assume that each type of atom interacts by the exchange constants,  $J_{ij}$ , only with nearest neighbors atoms

---

<sup>3</sup>We found that changing the spin configuration also in the fourth Cr layer leads to much higher energy.

Table 3.6: Parameters of the Heisenberg Hamiltonian for models A and B.  $\Delta$  is the mean-square misfit of the fitting. The last column shows corresponding parameters obtained from the values of the bulk exchange constants  $J_i^b$  (see Section 2.3). The units are eV.

	A	B	bulk
$J_{12}$	0.0038	0.0118	$J_3^b = 0.0017$
$J_{13}$	0.0109	0.0040	$J_4^b = 0.0027$
$J_{23}$	-0.0115	-0.0012	$J_2^b = -0.0138$
$h_1$	0.0009	0.0895	$J_5^b = -0.0028$
$h_2$	-0.434	-0.0215	$J_1^b + 3J_4^b = -0.0105$
$h_3$	-0.0007	0.0061	$J_5^b + 3J_3^b + 3J_4^b = 0.0105$
$c$	2.9748	3.1203	
$\Delta$	0.0005	0.0004	

of the two other types. In addition, each atom interacts with magnetic field,  $H_i$ , that represents the interactions with the bulk. The values of the exchange constants and magnetic fields were found by fitting the surface magnetic energies to the Heisenberg Hamiltonian (3.16) and are presented in Table 3.6. As seen, they are different from the values derived from the bulk exchange constants  $J_i^b$  (see Section 2.3). The latter were calculated under the assumption that exchange interactions at the surface are exactly the same as in the bulk which was clearly an oversimplification. This is the expected behavior since magnetic interactions are very sensitive to interatomic distances which are different at the surface compared with the bulk. In fact, the deviations between values of fitted parameters and those obtained from the bulk exchange constants are correlated to the change of the interlayer distances from Table 3.2.

For analysis of magneto-structural effects described in Section 3.4 we need the paramagnetic surface energies for superstructures AB, AAB, and ABB. For these superstructures we have four nonequivalent Cr atoms in the three closest to the surface atomic layers of Cr: surface Cr atom in the position A, surface Cr atom in the position B, the upper, and the lower Cr atom from the double Cr layer below the surface<sup>4</sup>. These site positions are denoted as 1A, 1B, 2, and 3, respectively. Similarly, as in the case of  $(1 \times 1)$  structures, in addition to interactions with magnetic field, we include only nearest neighbor interactions between atoms 2 and 3 as well as interaction between surface Cr atoms with their nearest neighbors of type 2 and 3. We assumed that the parameters describing these interactions can be found from the corresponding parameters from models A and B<sup>5</sup>. This approximation was checked

<sup>4</sup>For model AB, there are actually two types of upper and lower Cr atoms from double Cr layer below the surface. However, it doesn't matter whether we treat them as equivalent or not as long as the exchange constants and magnetic field for this model are taken from models A and B.

<sup>5</sup> $J_{1A2}$ ,  $J_{1A3}$ ,  $H_{1A}$  ( $J_{1B2}$ ,  $J_{1B3}$ ,  $H_{1B}$ ) are equal to corresponding parameters for model A (B);  $J_{23}$ ,  $H_2$ ,  $H_3$  are equal to appropriately weighted average of the corresponding parameters for models A and B.

for the AAB model for which the exchange constants and magnetic fields were found by fitting the magnetic surface energies of all 16 spin configurations to the Heisenberg Hamiltonian (3.16). In the Table 3.7, we compare the values of the fitted parameters with those found from models A and B. While there are some differences, the overall trend is preserved so parameters derived from the A and B models provide a reasonable estimate of the actual parameters. The paramagnetic surface energies for superstructures AB, AAB, and ABB were obtained starting from ground state surface energies (for bulk-like antiferromagnetic spin structure) and subtracting the magnetic part by using found above parameters of Heisenberg Hamiltonian for these superstructures.

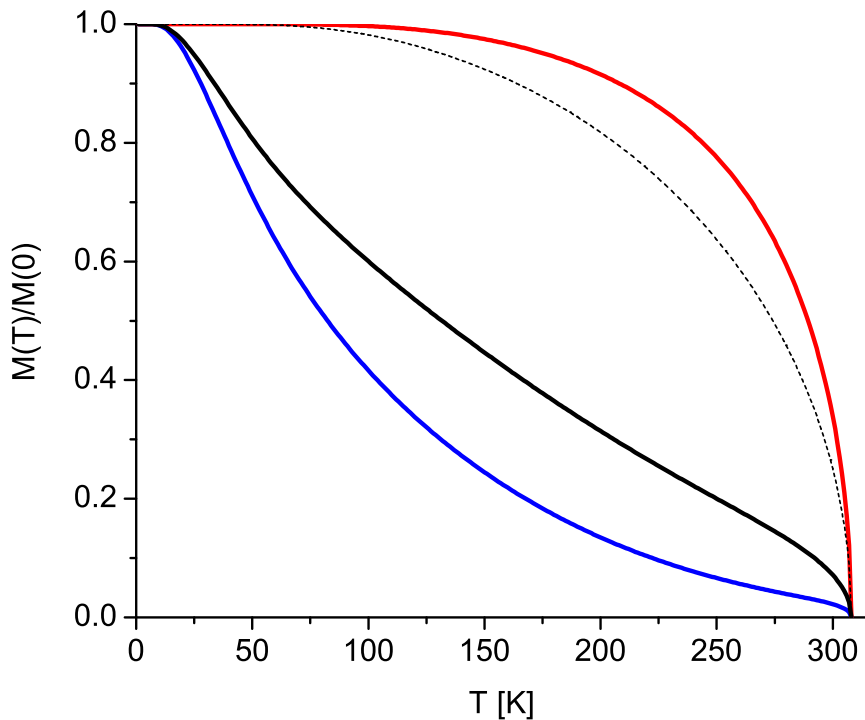


Figure 3.9: Reduced surface magnetization as a function of temperature for AAB surface model. Total magnetization (solid black line) and magnetizations of site A (solid blue line) and B (solid red line) are shown. In addition the bulk sublattice magnetization is plotted (dashed black line).

Having found the basic parameters of the Heisenberg Hamiltonian we can study the temperature dependence of the surface magnetization. We use the mean-field approximation for the quantum spin-3/2 Heisenberg Hamiltonian. Since the magnetic fields in Equation (3.16) represent the interactions with the magnetic structure of the bulk, they depend on temperature. In the spirit of mean-field approximation we assume that the magnetic fields are proportional to the bulk sublattice magnetization that is calculated from mean-field approximation and normalized to the experimental

Table 3.7: Parameters of the Heisenberg Hamiltonian for AAB model obtained from fitting to magnetic surface energies and from parameters of models A and B. The units are eV.

	fitted	from A and B
$J_{1A2}$	0.0072	0.0038
$J_{1B2}$	0.0042	0.0118
$J_{1A3}$	0.0095	0.0109
$J_{1B3}$	0.0027	0.0040
$J_{23}$	-0.0122	-0.0081
$h_{1A}$	0.0004	0.0009
$h_{1B}$	0.0746	0.0895
$h_2$	-0.0340	-0.0361
$h_3$	0.0013	0.0016

Néel temperature. The temperature dependence of surface magnetization for AAB surface model is shown in Figure 3.9. Even though at finite temperatures the surface magnetization is reduced as compared to the bulk sublattice magnetization, it remains appreciable up to room temperature. The reason for this reduction is that the site A is weakly coupled to the bulk (see Table 3.7) and therefore the magnetization of site A can be easily diminished by thermal fluctuations. On the other hand, site B is strongly coupled to the bulk and consequently as temperature rises the magnetization of site B remains large.

### 3.7 Conclusions

The (0001) surface of  $\text{Cr}_2\text{O}_3$  terminated with a single Cr layer was studied using first principles electronic structure calculations. We found two competing surface sites: site A corresponding to the continuation of the bulk and site B corresponding to the octahedral void below the O layer. By considering different surface supercells the ground state was identified for the AAB model with the  $(\sqrt{3} \times \sqrt{3})$  structure. The energy barrier for hopping between sites A and B was calculated to be 0.26 – 0.3 eV and therefore the hopping can be driven by thermal fluctuations. Two different configurational Ising-like Hamiltonians for occupation of the two surface sites were constructed. Parameters of the Hamiltonians were found by fitting energies of different surface supercells. Very good fit was achieved for the Hamiltonian derived under assumption that the interaction between surface Cr atoms is mainly of electrostatic nature. In this electrostatic model the interactions have a long-range dipolar form. The structural thermodynamics was studied using Monte Carlo method in Fourier space. With increasing temperature, we found a phase transition from  $(\sqrt{3} \times \sqrt{3})$  of AAB model to  $(1 \times 1)$  disordered structure with  $\sim 0.3$  probability of site B occupation. The transition temperature was found to be about 150 K in good agreement

with low energy electron diffraction (LEED) data [1]. We found that the parameters of the Hamiltonian depends on magnetic state making Hamiltonian temperature dependent. We proposed that this feature may cause reentrant phase transition that corresponds to low temperature phase transition from  $(1 \times 1)$  to  $(\sqrt{3} \times \sqrt{3})$  seen in LEED [1] when the  $\text{Cr}_2\text{O}_3$  (0001) lattice is strained (as may occur in the reported experiments [1, 8]).

We demonstrated that the single-domain (0001) surface of  $\text{Cr}_2\text{O}_3$  posses an uncompensated magnetic moment of about  $3\mu_B$  per surface Cr atom that is stable against surface roughness. This effect is unique for  $\text{Cr}_2\text{O}_3$  and it is a consequence of its special atomic and magnetic structure. The Heisenberg Hamiltonian describing this surface magnetism was found by fitting surface magnetic energies for AAB model. The temperature dependence of the surface magnetization was then studied using the mean-field approximation for this Heisenberg Hamiltonian and assuming spin  $3/2$ . We found that surface magnetism persists up to room temperature. This effect makes  $\text{Cr}_2\text{O}_3$  a promising material for exchange bias applications.

# Bibliography

- [1] M. Bender, D. Ehrlich, I. N. Yakovkin, F. Rohr, M. Bäumer, H. Kuhlenbeck, H. -J. Freund, and V. Staemmler, *J. Phys.: Condens. Matter* **7**, 5289 (1995).
- [2] F. Rohr, M. Bäumer, H. -J. Freund, J. A. Mejias, V. Staemmler, S. Müller, L. Hammer, and K. Heinz, *Surf. Sci.* **372**, L291 (1997); F. Rohr, M. Bäumer, H. -J. Freund, J. A. Mejias, V. Staemmler, S. Müller, L. Hammer, and K. Heinz, *Surf. Sci.* **389**, 391 (1997).
- [3] L. Zhang, M. Kuhn, and U. Diebold, *Surf. Sci.* **375**, 1 (1997).
- [4] P. Robbert, H. Geisler, C. Centrice, J. van Eck, S. Chaturvedi, J. Rodriguez, M. Kuhn, and U. Diebold, *J. Vac. Sci. Technol. A* **16**, 990 (1998).
- [5] Th. Gloege, H. L. Meyerheim, W. Moritz, and D. Wolf, *Surface Science* **441**, L917 (1999).
- [6] V. Maurice, S. Cadot, and P. Marcus, *Surf. Sci.* **458**, 195 (2000).
- [7] K. Wolter, D. Scarano, J. Fritsch, H. Kuhlenbeck, A. Zecchina, and H. -J. Freund, *Chem. Phys. Lett.* **320**, 206 (2000).
- [8] T. Takano, M. Wilde, M. Matsumoto, T. Okano, and K. Fukutani, *e-J. Surf. Sci. Nanotech.* **4**, 534 (2006).
- [9] Rehbein, N. M. Harrison, and A. Wander, *Phys. Rev. B* **54**, 14066 (1996).
- [10] J. A. Mejias, V. Staemmler, and H. -J. Freund, *J. Phys.: Condens. Matter* **11**, 7881 (1999).
- [11] J. A. Cline, A. A. Rigos, and T. A. Arias, *J. Phys. Chem. B* **104**, 6195 (2000).
- [12] X. -G. Wang and J. R. Smith, *Phys. Rev. B* **68**, 201402 (R) (2003).
- [13] A. Rohrbach, J. Hafner, and G. Kresse, *Phys. Rev. B* **70**, 125426 (2004).
- [14] J. Sun, T. Stirner, and A. Matthews, *Surf. Coat. Tech.* **201**, 4205 (2006).
- [15] N. J. Mosey, E. A. Carter, *J. Mech. Phys. Sol.* **57**, (2009).

- [16] G. C. Bond, *Heterogeneous Catalysis: Principles and Applications* (Oxford Chemistry Series, Clarendon Press, Oxford, 1974).
- [17] P. Marcus and V. Maurice, in *Passivity of Metals and Alloys* ed. M. Schutze, Corrosion and Environmental Degradation Vol. 1 (Wiley-VCH, Weinheim, 1999).
- [18] F. Rohr, *et. al.*, Surf. Sci. **315** L2977, (1994).
- [19] Ch. Binek and B. Doudin, J. Phys.: Condens. Matter **17**, L39 (2005).
- [20] P. Borisov *et. al.*, Phys. Rev. Lett. **94**, 117203 (2005).
- [21] P. J. Brown *et. al.*, J. Phys.:Condens. Matter **10**, 663 (1998).
- [22] Ch. Binek, private communication.
- [23] S. Sahoo and Ch. Binek, Phil. Mag. Lett. **87**, 259 (2007).
- [24] P. E. Blöchl, Phys. Rev. B **50**, 17953 (1994).
- [25] G. Kresse, and J. Hafner, Phys. Rev. B **48**, 13115 (1993).
- [26] G. Kresse, and J. Furthmüller, Phys. Rev. B **54**, 11169 (1996).
- [27] A. I. Liechtenstein, V. I. Anisimov, and J. Zaanen, Phys. Rev. B **52**, R5467 (1995).
- [28] Siqu Shi, A. L. Wysocki, and K. D. Belashchenko, Phys. Rev. B **79**, 104404 (2009).
- [29] H. Monkhorst, and J. D. Pack, Phys. Rev. B **13**, 5188 (1976).
- [30] M. Methfessel and A. T. Paxton, Phys. Rev. B **40**, 3616 (1989).
- [31] P. E. Blöchl, O. Jepsen, and O. K. Andersen, Phys. Rev. B **49**, 16223 (1994).
- [32] H. Jónsson, G. Mills, and K. M. Jacobsen, in Nudged Elastic Band Method for Finding Minimum Energy Paths of Transitions in Classical and Quantum Dynamics in Condensed Phase Simulations, edited by B. J. Berne, G. Ciccotti, and D. F. Coker (World Scientific, Singapore, 1998).
- [33] B. D. Metcalf, Phys. Lett. **46A**, 325 (1974).
- [34] Y. Tanaka and N. Uryû, J. Phys. Soc. Jpn. **39**, 825 (1975).

## Chapter 4

# Thermodynamics of itinerant magnets in a classical spin fluctuation model

In this chapter we describe the thermodynamics of itinerant magnets using a classical model that includes both transverse and longitudinal spin fluctuations. The Hamiltonian is described by a single parameter that characterizes the degree of itinerancy, i.e the relative importance of transverse and longitudinal fluctuations. Monte Carlo simulations for bcc and fcc lattices are compared with the mean-field approximation and with the Onsager cavity field approximation extended to itinerant systems. The qualitative features of thermodynamics are similar to the known results of the functional integral method. It is found that magnetic short-range order is weak and almost independent on the degree of itinerancy, and the mean-field approximation describes the thermodynamics reasonably well. Ambiguity of the phase space measure for classical models is emphasized. The Onsager cavity field method was extended to itinerant systems, which involves the renormalization of both the Weiss field and the on-site exchange interactions. The predictions of this approximation are in excellent agreement with Monte Carlo results.

### 4.1 Introduction

The thermodynamics of magnetic materials is often described using the Heisenberg model in which the spins are attached to lattice sites. Real magnets are much more complicated, because the magnetization is due to band electrons whose degree of localization varies between different materials. This so-called *itinerancy* manifests itself in the fluctuation of the magnitudes of the local moments, which may be defined in a muffin tin sphere or using a projection in an appropriate basis. Thus, the degree of itinerancy may be characterized by the relative importance of longitudinal and transverse (rotational) fluctuations of the local moments [1]. In the localized

(Heisenberg) limit the longitudinal spin fluctuations have a large energy scale and are suppressed. This limit is approached in some magnetic insulators. Metals, on the other hand, are often quite far from this limit, because the exchange splitting and the bandwidth are typically of the same order. Experimentally, itinerancy is most clearly revealed in the paramagnetic susceptibility by the deviation of the effective moment found from the Curie-Weiss constant from the true local moment, as well as by the deviations from the Curie-Weiss law.

A large amount of work has been devoted to the thermodynamics of itinerant magnets using phenomenological Ginzburg-Landau models for weak ferromagnets [2, 3, 1] or the Hubbard model and the functional integral methods [4, 5, 6, 1]. These studies have clarified the role of longitudinal spin fluctuations in thermodynamics and explained the observed behavior of the paramagnetic susceptibility. However, these methods are unsuitable for quantitative studies of realistic materials. Ginzburg-Landau expansions, as is well known, correctly describe only the contribution of long-wave fluctuations and must always be rigged with a wavevector cut-off. Such models are useful in the studies of critical phenomena, but they are irrelevant to the determination of the critical temperature itself, which is determined by *short-range* fluctuations [7]. An unsatisfactory signature of Ginzburg-Landau models is the absence of any information on the short-wave components of the exchange interaction in the resulting expressions for the Curie temperature [2, 3, 8]. In our opinion, the neglect of short-wave fluctuations in these models makes their predictions for magnetic short-range order also unreliable. The functional integral method, on the other hand, suffers from the necessity to make severe and ambiguous approximations [9].

Magnetic thermodynamics has also been studied using density functional theory (DFT) by treating spin fluctuations within the adiabatic approximation [10] assuming that the relevant fluctuations are well represented by constrained [11] noncollinear ground states. The most widespread approach is the disordered local moment approximation [12, 10] which relies on the single-site approximation and is designed to approximate the DFT ground state of a system with random directions of the local moments. The longitudinal spin fluctuations have been neglected in all implementations of this approach so far, restricting its application to magnets which are close to the localized limit. In particular, the disordered local moment method neglecting longitudinal spin fluctuations fails for (strongly itinerant) nickel where it finds vanishing local moment in the paramagnetic phase [13].

Other authors studied *itinerant* thermodynamics by mapping the results of first-principles energies for various spin configurations (including both transverse and longitudinal fluctuations) to a classical Hamiltonian in which variable local moments play the role of dynamical variables, and then exploring the thermodynamics of this Hamiltonian using either the variational principle in reciprocal space [14] or Monte Carlo simulations in real space [15, 16, 17]. These calculations clearly show that longitudinal spin fluctuations, as expected, are very important in nickel. Moreover, they revealed only weak magnetic short-range order above the Curie temperature  $T_c$  for both Fe and Ni, which is similar to the Heisenberg model. These results are consistent

with the fact that in any lattice model with no frustration all correlation corrections to the mean-field approximation (outside of the critical region) should be small in the parameter  $1/z$ , where  $z$  is the number of neighbors within the interaction range [18]. On the other hand, very strong magnetic short-range order above  $T_c$  was found [19] in Ni using the *ab initio* spin dynamics method, which, similar to disordered local moment, is based on the adiabatic approximation and neglects longitudinal spin fluctuations.

Classical models with variable local moments seem to capture the important qualitative features of the thermodynamics of itinerant magnets which are similar to the predictions of the functional integral method. However, these models have been built and studied only for a few particular materials, and a general study of their thermodynamic properties has not been undertaken. Such a study is useful as a step to more refined models with the advantage that numerically exact results for a classical model are easily accessible through Monte Carlo simulations. Therefore, in this chapter we explore the thermodynamics of a classical spin fluctuation model as a function of the degree of itinerancy using Monte Carlo simulations and simple analytic approximations. We emphasize that here we were not concerned with the “mapping” procedure (i.e., finding the magnetic Hamiltonian for specific materials) but rather focused on the other separate part of the program, i.e. on the determination of the magnetic thermodynamics once the Hamiltonian has been defined. We therefore restrict ourselves to the simplest possible realization of this model which includes only *one* free parameter characterizing the degree of itinerancy.

## 4.2 Model

Our model is a lattice version of the phenomenological model of Murata and Doniach [2] written with a vector order parameter [1]:

$$\begin{aligned}
 H &= \frac{1}{2} \sum_{\mathbf{q}} \chi^{-1}(\mathbf{q}) \mathbf{m}_{\mathbf{q}} \mathbf{m}_{-\mathbf{q}} + \frac{B}{4} \sum_i m_i^4 \\
 &= \sum_i \left[ \frac{1}{2} (\chi_{00}^{-1} - I) m_i^2 + \frac{B}{4} m_i^4 \right] - \frac{1}{2} \sum_{i \neq j} J_{ij} \mathbf{m}_i \mathbf{m}_j.
 \end{aligned} \tag{4.1}$$

Here  $\mathbf{m}_i$  denotes the magnetic moment at site  $i$  whose length is unrestricted, and  $I$  the Stoner exchange-correlation parameter. We have separately written the local  $\chi_{00}^{-1} = \partial B_i / \partial m_i$  and nonlocal  $J_{ij} = -\chi_{ij}^{-1}$  parts of the unenhanced inverse susceptibility. This model involves a number of simplifying assumptions: (1) It is classical in the sense that  $\mathbf{m}_i$  are dynamical variables and not operators. (2) Both local and nonlocal parts of the inverse susceptibility are considered to be independent of the magnetic state and *isotropic*. In general,  $\chi_{ij}^{-1}$  is a Cartesian tensor which depends on the magnetic state and reduces to a scalar only in the paramagnetic state. (3) Nonlinear effects are included only through a local fourth-order term, similar to the Murata-Doniach

model.

Model (4.1) is somewhat similar to that used to represent the unified spin fluctuation theory [4] classically (see Ref. [1], Ch. 7, and also Ref. [20]), with an important difference: the energy of the longitudinal spin fluctuations was included as a function of the local dynamical variables  $\mathbf{m}_i$ , rather than that of one global parameter  $\langle m_i^2 \rangle$ . This difference is similar to that between the Heisenberg model and the spherical approximation to it.

In the ground state all local moments are parallel and we recover the Stoner model which is ferromagnetic if  $IN(E_F) > 1$ , where  $N(E_F) = \chi(0)$  is the density of states at the Fermi level in the nonmagnetic state. This Stoner criterion can also be written as  $(I + J_0) > \chi_{00}^{-1}$  where  $J_0 = \sum_j J_{ij}$ . On the other hand, in the paramagnetic or non-magnetic matrix, local moments exist in the Anderson sense only if  $I > \chi_{00}^{-1}$  which is stricter than the Stoner criterion. We will call this the Anderson criterion. (Note that  $\chi_{00}^{-1} \neq 1/\chi_{00}$ .)

Introducing the reduced local moments  $\mathbf{x}_i = \mathbf{m}_i/m_0$ , where  $m_0$  is the value of all  $m_i$  at  $T = 0$ , the Hamiltonian (4.1) can be conveniently parameterized:

$$H' \equiv \frac{H}{J_0 m_0^2} = \sum_i E(x_i) - \frac{1}{2} \sum_{i \neq j} \frac{J_{ij}}{J_0} \mathbf{x}_i \cdot \mathbf{x}_j \quad (4.2)$$

where  $E(x) = [ax^2/2 + bx^4/4]/J_0$  with  $a = \chi_{00}^{-1} - I$  and  $b = Bm_0^2 = J_0 - a$ . For the nearest neighbor model with coordination number  $z$  we have  $J_{nn}/J_0 = 1/z$ , and for the given lattice  $H'$  contains only one parameter, which we define as  $\alpha = \arctan b/a$ . Note that  $b > 0$  is equivalent to the Stoner criterion, and  $a < 0$  is equivalent to the Anderson criterion.

To understand the meaning of the parameter  $\alpha$ , consider the ground state of Hamiltonian  $H$  with a single-site excitation, i.e. the state with  $\mathbf{m}_i = \mathbf{m}_0$  for all  $i$  except  $i = c$ . The energy of this state has a minimum at  $\mathbf{m}_c = \mathbf{m}_0$  and its curvature with respect to the longitudinal fluctuation of  $\mathbf{m}_c$  is  $K_{\parallel} = J_0 + 2b$ , while the curvature with respect to transverse fluctuations is  $K_{\perp} = J_0$ . Their ratio  $K_{\parallel}/K_{\perp} = 1 + (2b/J_0)$  characterizes the relative importance of longitudinal and transverse fluctuations. If  $b \gg J_0$ , the fluctuations are mainly transverse, and we have the localized (Heisenberg) limit for which  $a \approx -b$  and  $\alpha \approx 3\pi/4$ . If  $b \ll J_0$ , the transverse and longitudinal spin fluctuations are equally important; this limit corresponds to  $\alpha = 0$ . The Anderson criterion is equivalent to  $\alpha > \pi/2$ . Thus, the parameter  $\alpha$  characterizes the degree of itinerancy and is similar to those appearing in other theories [4, 1]. Note that we always have  $K_{\parallel}/K_{\perp} > 1$ , even though the *macroscopic* longitudinal stiffness is proportional to  $b$  and tends to zero at  $\alpha \rightarrow 0$ .

Evaluation of the thermodynamic properties involves taking a trace over the quantum states, or a functional integral over the classical degrees of freedom. To our knowledge, in all classical models reported so far and based on *ab initio* calculations, the uniform measure in the space of  $\mathbf{m}_i$  was used [14, 15, 16, 17]. However, our dynamical variables are not canonical, and therefore the phase space measure is not

known. In the case when longitudinal spin fluctuations are important, the phase space measure has to be supplied along with the Hamiltonian as an additional phenomenological ingredient. Strictly speaking, it is not possible to disentangle the measure from quantum statistics; for example, in the atomic limit only integer moments with atomic multiplet degeneracies should be present. Ambiguity of phase space measure is intrinsic to all microscopic classical spin fluctuation models including the classical version of the “unified theory” of Moriya and Takahashi (Ref. [1], Sec. 7) and its extensions, [20] as well as the functional integral approach combined with the static approximation which destroys the correct quantum operator properties. In the latter case, the Hubbard-Stratonovich transformation can be applied with the interaction term written in different ways, which produced different results after the static approximation was made [5, 9]. Two particular choices discussed by Hubbard [5] result in different measures in the space of fluctuating fields  $\mathbf{v}_i$ : uniform in one case, and involving the weighting factor  $\prod_i v_i^{-2}$  in another. To explore the influence of phase space measure on the thermodynamics, we considered these two measures in the space of the local moments  $\mathbf{m}_i$ .

### 4.3 Thermodynamic properties: Monte Carlo and mean-field results

Monte Carlo simulations for model (4.2) were performed using the Metropolis algorithm for bcc and fcc lattices with nearest neighbor exchange. At each step, a new random direction and magnitude of the moment on one site was applied, and sampling of the moment magnitude was performed according to the chosen phase space measure. We used supercells with up to 3456 or 6912 sites for bcc or fcc lattices ( $12 \times 12 \times 12$  unit cells with periodic boundary conditions). The reduced Curie temperature  $t_c = T_c/(J_0 m_0^2)$  was found using the fourth-order cumulant method [21], and the paramagnetic susceptibility was calculated using the fluctuation-dissipation theorem.

In the mean-field approximation the magnetization is found from the self-consistency condition  $\langle x_z \rangle = \partial \ln Z_1 / \partial (\beta H_W)$ , where

$$Z_1 = \int_0^\infty g(x) x \frac{2 \sinh(\beta H_W x)}{\beta H_W} e^{-\beta E(x)} dx \quad (4.3)$$

is the single-site partition sum,  $H_W = \langle x_z \rangle$  the reduced Weiss field, and  $g(x)$  is the weighting factor, which is either 1 or  $x^{-2}$  for the two chosen phase space measures.  $E(x)$  is defined after Equation (4.2), and  $\beta = 1/t$  is the inverse reduced temperature.

Figure 4.1 shows the temperature dependence of magnetization, the average square of the local moment and the paramagnetic susceptibility using the reduced variables according to Equation (4.2). Results are shown for two values of  $\alpha$ :  $0.48\pi$  and  $0.69\pi$ . In both cases, the agreement between Monte Carlo and mean-field approximation

results is very good for all properties (mean-field approximation overestimates  $T_c$  by 20% or less which is typical for the Heisenberg model). The results strongly depend on phase space measure, especially in the more itinerant case  $\alpha = 0.48\pi$ . In particular, for the uniform phase space measure a second-order phase transition occurs for both values of  $\alpha$ , but for the phase space measure with  $g(x) = x^{-2}$  the phase transition is of first order for  $\alpha = 0.48\pi$ , and  $T_c$  is nearly 2.8 times smaller compared to that for  $g(x) = 1$ .

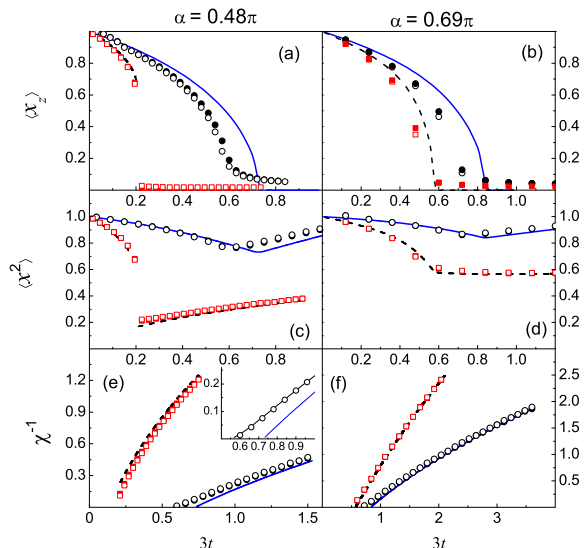


Figure 4.1: (a-b) Reduced magnetization  $\langle x_z \rangle$ , (c-d) mean squared local moment  $\langle x^2 \rangle$ , and (e-f) inverse paramagnetic susceptibility  $\chi^{-1}$  as a function of the reduced temperature  $t = T/(J_0 m_0^2)$ . Mean-field approximation with  $g(x) = 1$  (solid blue (grey) lines) or with  $g(x) = x^{-2}$  (dashed black lines), Monte Carlo with  $g(x) = 1$  (black circles, filled for fcc and empty for bcc lattice), Monte Carlo with  $g(x) = x^{-2}$  (red (grey) squares, filled for fcc and empty for bcc lattice). The inset in panel (e) highlights the region close to  $t_c$  for the bcc lattice with  $g(x) = 1$  and also shows the results of the generalized Onsager method (black line connecting the Monte Carlo points).

As seen in Figure 4.1, below  $T_c$  the average  $\langle x^2 \rangle$  declines with temperature due to the decrease of the Weiss field, which in turn causes the maximum of the distribution function to shift to smaller moments. This is in agreement with earlier results [1, 5, 6, 14, 15, 17]. The width of the distribution function increases with temperature, which counteracts the decrease of the local moment. The phase space measure with  $g(x) = x^{-2}$  puts less weight on the states with large moments, and hence  $\langle x^2 \rangle$  drops much faster compared to the uniform phase space measure. If the Anderson criterion is not satisfied ( $\alpha < \pi/2$ ) then the most probable moment in the paramagnetic state is zero. In this case,  $\langle x^2 \rangle$  increases with temperature above  $T_c$  as seen in Figure

4.1c. On the other hand, if the Anderson criterion is satisfied, the local moment may slightly decrease in a range of temperatures above  $T_c$ , as seen for  $g(x) = x^{-2}$  in Figure 4.1d.

The inverse paramagnetic susceptibility,  $\chi^{-1}$  is shown in Figures 4.1e,f. In Monte Carlo simulations it is calculated using fluctuation-dissipation theorem, while in mean-field approximation we directly consider the response of the system to the external magnetic field. Excellent agreement between mean-field approximation and Monte Carlo is observed except for the small error in  $T_c$ . In mean-field approximation, one obtains above  $T_c$

$$\chi_{\text{MFA}}^{-1} = \frac{\frac{1}{3}\langle x^2 \rangle}{t - \frac{1}{3}\langle x^2 \rangle} \quad (4.4)$$

This formula looks similar to the Curie-Weiss expression in the Heisenberg model, but here  $\langle x^2 \rangle$  depends on temperature, which leads to a renormalization of the Curie-Weiss constant and deviations from the Curie-Weiss law. The Curie-Weiss constant  $C = d\chi^{-1}/dt$  (for a second-order phase transition) is now given by

$$C = \frac{3}{\langle x^2(t_c) \rangle} \left[ 1 - \left. \frac{d \log \langle x^2 \rangle}{d \log t} \right|_{t_c} \right] \quad (4.5)$$

Thus, in addition to the usual Heisenberg term, the Curie constant has a contribution due to the temperature dependence of  $\langle x^2 \rangle$  (the second term in square brackets in (4.5)). As a result, the effective moment squared  $x_{\text{eff}}^2 = 3/C$  deviates from  $\langle x^2 \rangle$ . As discussed above,  $\langle x^2 \rangle$  usually increases with temperature above  $T_c$ , which, according to Equation (4.5), reduces  $C$  and increases  $x_{\text{eff}}^2$ . Moreover, for the uniform phase space measure,  $\langle x^2 \rangle$  increases faster with temperature compared to phase space measure with  $g(x) = x^{-2}$ , and hence the Curie-Weiss constant is much smaller (see Figure 4.1f and also 4.1e, where the transition is however of first order).

In Figure 4.2 some thermodynamic properties of the system are plotted as a function of the itinerancy parameter  $\alpha$ . From Equation (4.4) it follows that the mean-field approximation value of  $t_c$  for the second-order phase transition is found by solving the equation  $3t_c = \langle x^2(t_c) \rangle$ , where  $\langle x^2(t) \rangle$  is fully determined by  $E(x)$  in Equation (4.2). This is an easy way to estimate  $T_c$  for an itinerant system using first-principles data for  $E(x)$ ,  $J_0 m_0^2$ , and the assumed phase space measure. However, for phase space measure with  $g(x) = x^{-2}$  the transition is of first order except for a small region close to the local moment limit (in mean-field approximation the tricritical point where the order of the phase transition changes is at  $\alpha_{tr} = 0.632\pi$ ). Therefore, in general one must consider the minima of the free energy as a function of the magnetization, which can also be easily done in mean-field approximation. Note that the order of the phase transition depends on the details of the model and can change if, for example, the dependence of the exchange parameter on the magnetization is taken into account. In particular, the phase transition for the model of Ni is of first order in Ref. [14] (as seen from the abrupt drop of  $M(T)$  and  $M_s$  at  $T_c$  in their Fig. 2) and in Ref. [17] (as seen from the abrupt drop of  $\bar{m}$  in their Figure 6), even though

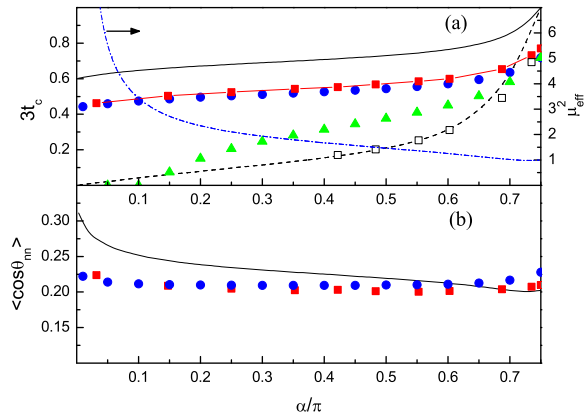


Figure 4.2: (a) Reduced Curie temperature  $t_c$  and (b) magnetic short-range order parameter  $\langle \cos \theta_{nn} \rangle$  at  $T = 1.1T_c$  as a function of the itinerancy parameter  $\alpha$  for the bcc lattice. Solid black line, red (grey) squares, and blue (grey) circles denote mean-field approximation, Monte Carlo, and the generalized Onsager method for  $g(x) = 1$ , respectively. Dashed black line and empty black squares denote mean-field approximation and Monte Carlo for  $g(x) = x^{-2}$ . Green (grey) triangles show the results of the incomplete Onsager reaction field correction with the on-site interaction left unrenormalized. The blue (grey) dash-dotted line in the upper panel: effective moment  $x_{\text{eff}}^2$  found from the Curie constant for  $g(x) = 1$  in mean-field approximation. Very similar results were obtained for the fcc lattice (not shown).

the uniform phase space measure was used in both of these models.

From Figure 4.2 we see that when the transition is of second order, mean-field approximation overestimates  $T_c$  by about 20%, which is typical for the Heisenberg model. When the transition is of first order, mean-field approximation gives an almost exact  $T_c$ . It is important that even for the second-order transition the overestimation of  $T_c$  in mean-field approximation does not depend on the degree of itinerancy. This is consistent with the fact that the degree of magnetic short-range order, which is shown in Figure 4.2b for  $T = 1.1T_c$ , is quite small and stays essentially constant in the whole range of  $\alpha$ . Thus, in our model itinerancy does not lead to strong short-range order. This result agrees with Refs. [15, 17] where weak short-range order was found for the models of Fe and Ni. Note that if the exchange interaction extends to more than one shell of neighbors and stays mainly ferromagnetic, the mean-field approximation validity criterion is satisfied even better, and the magnetic short-range order parameter should further decrease. Similar to the Heisenberg model, the strong magnetic short-range order may only be expected in low-coordination lattices or in the presence of frustration when for some pairs  $J_{ij}/kT_c$  are not small.

The square of the effective moment  $x_{\text{eff}}^2$  is also shown in Figure 4.2 for the uniform phase space measure (dash-dotted line). In the local limit  $x_{\text{eff}}$  naturally tends to 1. However, as  $\alpha$  decreased towards zero, the ratio  $x_{\text{eff}}^2/\langle x^2(t_c) \rangle$  increased and eventually

became much larger than 1. Similar behavior was found in functional integral theories [1].

## 4.4 Generalized Onsager correction for itinerant systems

Onsager introduced the concept of a *cavity field* in the theory of polar liquids, which was designed to go beyond the molecular field approximation by including short-range order effects [22]. The cavity field is the *effective* internal field which orients polar molecules in the ferroelectric phase. Onsager observed that each molecule polarizes the surrounding liquid and thereby generates a *reaction field* acting back on the molecule. However, this field is always parallel to the molecule's dipole moment and hence does not affect orientation. Therefore, for a liquid with *permanent* dipoles the reaction field must be subtracted from the mean molecular field, the result being the cavity field. Onsager also noted that the reaction field enhances the dipole moments of real molecules due to their polarizability.

The cavity field method was successfully applied to Ising [23] and Heisenberg [24] magnets which have permanent magnetic moments. Cyrot [25] noted that Moriya-Kawabata's self-consistent renormalization theory for the Hubbard model may be essentially reproduced by using Onsager-like arguments; more recently this method was implemented numerically [26]. However, the actual physics there is very different; Cyrot's approach seeks the correlation correction with respect to the Hartree-Fock solution, which is unrelated to short-range order. Onsager's method was also applied to itinerant nickel [13], but, as we will see below, correct generalization to itinerant systems with longitudinal spin fluctuations requires an additional ingredient which was missed in Ref. [13].

We generalized Onsager's method to magnets with longitudinal spin fluctuations, described by Hamiltonian (4.1). Consider model (4.1) above  $T_c$  in a small external collinear magnetic field  $H_i^{ext} \mathbf{e}_z$ . We pick site 0 and integrate out the degrees of freedom from all the other sites in the partition function to obtain the effective Hamiltonian in the form of a generating functional for the lattice with a cavity [18]. Expanding this functional around the atomic limit to order  $1/z$  we obtain

$$H_{\text{eff}}^0 = E(m_0) - \mathbf{m}_0 \left( \mathbf{H}_0^{ext} + \sum_i J_{0i} \langle \mathbf{m}_i^c \rangle \right) - \frac{m_0^2}{2} \sum_{ij} J_{0i} J_{0j} \chi_{ij}^c \quad (4.6)$$

where the superscript  $c$  refers to the lattice with a cavity, i.e. with site 0 removed, and we used the fluctuation-dissipation theorem to express the pair correlator through the susceptibility.

In order to find the magnetization and susceptibility of the lattice with a cavity, we need to solve the “impurity problem.” Using the linked-cluster expansion technique [27], the longitudinal susceptibility of the original lattice may be written as follows:

$$\hat{\chi} = \hat{\Pi} + \hat{\Pi}\hat{W}\hat{\Pi} \quad (4.7)$$

where  $\hat{W}$  is the effective interaction that satisfies the equation  $\hat{W} = \hat{J} + \hat{J}\hat{\Pi}\hat{W}$ , and  $\hat{\Pi}$  is the 1-bond-irreducible “polarization operator” which may be shown to be local to first order in  $1/z$  [28] (All quantities in Equation (4.7) are matrices in site indices). Removal of site 0 may be formally represented by a perturbation  $\Delta\hat{\Pi} = -\Pi_{00}\delta_{0i}\delta_{0j}$  to  $\hat{\Pi}$ . (The renormalization of  $\Pi_{jj}$  for  $j \neq 0$  due to removal of site 0 is at least of order  $1/z^2$ .) Thus, denoting the effective interaction matrix for the cavity lattice as  $\hat{W}_c$ , we may write  $\hat{W}_c^{-1} - \hat{W}^{-1} = -\Delta\hat{\Pi}$ . Using (4.7) and the fact that  $\hat{\Pi}$  is diagonal, we find

$$\chi_{ij}^c = \chi_{ij} - \frac{\chi_{i0}\chi_{0j}}{\chi_{00}}. \quad (4.8)$$

The average local moments  $\mathbf{M}_i^c = \langle \mathbf{m}_i^c \rangle$  for the lattice with a cavity are:

$$M_i^c = \sum_j \chi_{ij}^c H_j^{ext} = M_i - \frac{\chi_{i0}}{\chi_{00}} M_0, \quad (4.9)$$

where  $M_i$  are the average local moments of the complete lattice without the cavity. The value of  $\mathbf{H}_0^{ext}$  does not affect  $M_i^c$  (as expected), therefore in the right-hand side of (4.9) we may take  $M_i$  and  $M_0$  for the actual field distribution.

From the effective Hamiltonian (4.6) we can find the magnetization at site 0:

$$M_0 = \tilde{\chi}^0 \tilde{H}_W \quad (4.10)$$

where

$$\tilde{H}_W = H_0^{ext} + \sum_i J_{0i} \left( M_i - \frac{\chi_{i0}}{\chi_{00}} M_0 \right) \quad (4.11)$$

is the renormalized effective field (cavity field), and  $\tilde{\chi}^0$  is the *renormalized* bare (atomic-limit) susceptibility. The latter may be written as  $\tilde{\chi}^0 = \langle m^2 \rangle_\lambda / 3T$ , where the average paramagnetic squared local moment  $\langle m^2 \rangle_\lambda$  was calculated using a renormalized on-site exchange  $\tilde{I} = I + \lambda$  with  $\lambda = \sum_{ij} J_{0i} J_{0j} \chi_{ij}^c$ . This renormalization of the bare susceptibility is the essential ingredient needed to extend Onsager’s theory to itinerant magnets. It has no effect in the localized limit where  $m^2$  is constant.

As usual, we now obtain the Fourier transform of the susceptibility:

$$\chi_{\mathbf{q}} = \frac{\tilde{\chi}^0}{1 - \tilde{\chi}^0 (J_{\mathbf{q}} - \lambda)}, \quad (4.12)$$

where  $\lambda = \sum_{\mathbf{q}} J_{\mathbf{q}} \chi_{\mathbf{q}} / \chi_{00}$ . We used the same symbol  $\lambda$  as above in the definition

Table 4.1: Reduced Curie temperature  $t_c$  for bcc and fcc lattices for phase space measure with  $g(x) = 1$ : Results of the mean-field approximation (MFA), Horwitz-Callen approximation (HC), generalized Onsager method (GO) and Monte Carlo (MC).

$\alpha/\pi$	bcc				fcc			
	MFA	HC	GO	MC	MFA	HC	GO	MC
0.032	0.621	0.449	0.451	0.462(1)	0.621	0.465	0.466	0.480(2)
0.148	0.660	0.484	0.486	0.504(2)	0.660	0.501	0.502	0.520(5)
0.250	0.681	0.503	0.504	0.525(2)	0.681	0.519	0.520	0.540(5)
0.352	0.699	0.518	0.520	0.543(2)	0.699	0.535	0.536	0.562(2)
0.422	0.712	0.529	0.530	0.553(1)	0.712	0.546	0.547	0.570(5)
0.483	0.723	0.539	0.541	0.568(1)	0.723	0.557	0.558	0.584(2)
0.553	0.745	0.555	0.557	0.585(2)	0.745	0.572	0.574	0.600(1)
0.602	0.765	0.570	0.573	0.600(2)	0.765	0.589	0.590	0.617(2)
0.687	0.834	0.619	0.622	0.654(3)	0.834	0.640	0.642	0.672(6)
0.735	0.942	0.683	0.688	0.732(2)	0.942	0.708	0.711	0.753(6)
0.750	1	0.713	0.718	0.770[30]	1	0.740	0.743	0.788(3)

of  $\tilde{I}$ , because these expressions are identical, as can now be shown with the help of Equations (4.12) and (4.8). Equation (4.12) with the definitions of  $\lambda$ ,  $\tilde{\chi}^0$  and  $\tilde{I}$  form a closed set of equations for the paramagnetic susceptibility. Note that (4.12) *automatically* leads to a sum rule  $\chi_{00} = \tilde{\chi}^0$ , which agrees with the fluctuation-dissipation theorem.

At the Curie temperature,  $\chi_{\mathbf{q}}$  diverges at  $\mathbf{q} = 0$ . Therefore, from (4.12) we obtain  $T_c = \frac{1}{3}J_0\langle m^2(T_c)\rangle_\lambda/G$  where  $G = \sum_{\mathbf{q}}(1 - J_{\mathbf{q}}/J_0)^{-1}$  is the diagonal element of the lattice Green's function [24]. Note that the value of  $\lambda$  at  $T_c$  is equal to  $J_0(1 - G^{-1})$  and independent of the degree of itinerancy  $\alpha$ .

The reduced Curie temperature  $t_c$  and the magnetic short-range order parameter  $\langle \cos \theta_{mn} \rangle$  at  $T = 1.1T_c$  calculated in this way are shown in Figure 4.2 for the bcc lattice and the phase space measure with  $g(x) = 1$ . The agreement with the Monte Carlo results is excellent in the whole range of  $\alpha$ . We repeated these calculations for the fcc lattice and found excellent agreement with the Monte Carlo simulations as well. The accuracy of the predicted  $t_c$  may be seen from Table 4.1. Similar performance for bcc and fcc lattices suggests that this approximation is not very sensitive to the connectivity of the lattice. The paramagnetic susceptibility is also shown in Figure 4.1e for  $\alpha = 0.48\pi$ , bcc lattice, and uniform phase space measure. The agreement with Monte Carlo results is essentially perfect outside of the narrow critical region.

The first-order terms in the  $1/z$  expansion derived above introduce two corrections to mean-field approximation. The first one is the subtracted *mean* reaction field; this correction reduces the magnetization. This is the only correction in Onsager's method for systems with permanent moments. The second correction described by

the last term in Equation (4.6) adds back the *fluctuating* reaction field which is always parallel to the moment on the central site. For the Heisenberg (or Ising) model this second correction has no effect, but in itinerant systems it always increases the local moments and hence the Curie temperature. There is a strong cancelation between these two corrections in itinerant systems, and improvement compared to mean-field approximation may be achieved only if both of them are included. Indeed, if the renormalization of the Stoner parameter is not taken into account (i.e. if the last term in Equation (4.6) is dropped), we find a spurious strong suppression of  $T_c$  for itinerant systems, as shown in Figure 4.2a.

It is interesting to compare the generalized Onsager method with the Horwitz-Callen (HC) approximation which is based on the “ring subset” of diagrams for the generating functional  $\Phi$  in the linked-cluster technique [29, 27]. In this method, the second-order self-field  $G_2$  is found by differentiating  $\Phi$  with respect to the renormalized second cumulant  $M_2$ , while  $M_2$  is represented by an integral containing  $G_2$  as a parameter. This technique does not assume any particular form for the atomic limit, and therefore it can be used in our case including longitudinal spin fluctuations as well. In the HC method, the on-site correlator may be found as  $K_{00} = M_2 + 2M_2^2 G_2$ , and the sum rule  $K_{00} = 1$  is not satisfied in the paramagnetic Heisenberg magnet. However, it is easy to check that the value of  $K_{00}$  at  $T_c$  is smaller than 1 by less than a percent in bcc and fcc lattices. In Onsager’s method for the Heisenberg model, the sum rule  $K_{00} = 1$  is used to fix  $M_2$  instead of the integral representation as in the HC method. The results for  $T_c$  are therefore very close. We found that this close similarity remains in the entire range of  $\alpha$ , as seen from Table 4.1. The generalized Onsager’s method is, however, technically much simpler.

## 4.5 Conclusions

We have studied the thermodynamics of a simple classical spin fluctuation model allowing for a variable degree of itinerancy. This model was qualitatively similar to those used before to study the thermodynamics of Fe and Ni using first-principles data [14, 15, 17]. It is worth emphasizing that the main drawback of using classical spin models of this type is the ambiguity of the phase space measure. As we showed above, the thermodynamics is very sensitive to this measure for systems with even intermediate degree of itinerancy. While the energetics of constrained spin configurations may, at least in principle, be accurately mapped using DFT calculations, it is not known (to our knowledge) how and whether the phase space measure can be supplied in a realistic way.

In the present work, we focused on the general features of the model rather than on the determination of its parameters from principles. We found that the thermodynamic properties are similar to the results of the functional integral approach [1, 4, 5, 6]. Further, we found that the mean-field approximation is qualitatively valid, and short-range order is weak and almost independent on the degree of itinerancy up

to the strongly itinerant limit where the paramagnetic susceptibility is dominated by longitudinal fluctuations. This is in agreement with earlier results for the models of Fe and Ni [15, 17]; it is clear that this is a general feature of the classical model with no frustration.

Further, we generalized the Onsager cavity field method to itinerant systems using an expansion around the atomic limit to first order in  $1/z$ . Both the interatomic exchange constant and the Stoner parameter are renormalized by short-range order. When both these corrections are included, the Curie temperature is in excellent agreement with Monte Carlo results. However, simple subtraction of the Onsager reaction field is a very poor approximation.

# Bibliography

- [1] T. Moriya, *Spin fluctuations in itinerant electron magnetism* (Springer, Berlin, 1985).
- [2] K. K. Murata and S. Doniach, *Phys. Rev. Lett.* **29**, 285 (1972).
- [3] G. G. Lonzarich and L. Taillefer, *J. Phys. C* **18**, 4339 (1985).
- [4] T. Moriya and Y. Takahashi, *J. Phys. Soc. Japan* **45**, 397 (1978).
- [5] J. Hubbard, in: *Electron correlation and magnetism in narrow-band systems*, ed. by T. Moriya (Springer, Berlin, 1981), p. 29.
- [6] H. Hasegawa, *ibid.*, p. 38.
- [7] L. D. Landau and E. M. Lifshitz, *Statistical Physics* (Pergamon, Oxford, 1980), sec. 147.
- [8] P. Mohn and E. P. Wohlfarth, *J. Phys. F* **17**, 2421 (1986).
- [9] R. F. Hasing and D. M. Esterling, *Phys. Rev. B* **7**, 432 (1973).
- [10] B. L. Gyorffy, A. J. Pindor, J. Staunton, G. M. Stocks, and H. Winter, *J. Phys. F: Met. Phys.* **15**, 1337 (1985).
- [11] P. H. Dederichs, S. Blügel, R. Zeller, and H. Akai, *Phys. Rev. Lett.* **53**, 2512 (1984).
- [12] T. Oguchi, K. Terakura, and N. Hamada, *J. Phys. F* **13**, 145 (1983).
- [13] J. B. Staunton and B. L. Gyorffy, *Phys. Rev. Lett.* **69**, 371 (1992).
- [14] M. Uhl and J. Kübler, *Phys. Rev. Lett.* **77**, 334 (1996).
- [15] N. M. Rosengaard and B. Johansson, *Phys. Rev. B* **55**, 14975 (1997).
- [16] M. Lezaić, P. Mavropoulos, J. Enkovaara, G. Bihlmayer, and S. Blügel, *Phys. Rev. Lett.* **97**, 026404 (2006)

- [17] A. V. Ruban, S. Khmelevskiy, P. Mohn, and B. Johansson, *Phys. Rev. B* **75**, 054402 (2007).
- [18] A. Georges, G. Kotliar, W. Krauth, and M. J. Rozenberg, *Rev. Mod. Phys.* **68**, 13 (1996).
- [19] V. P. Antropov, *Phys. Rev. B* **72**, 140406(R) (2005).
- [20] J. Kübler, *J. Phys.: Condens. Matter* **18**, 9795 (2006).
- [21] D. P. Landau, K. Binder, *A guide to Monte Carlo simulations in Statistical Physics*, (Cambridge University Press, Cambridge, 2000).
- [22] L. Onsager, *J. Am. Chem. Soc.* **58**, 1486 (1936).
- [23] R. Brout and H. Thomas, *Physics* (Long Island City, N.Y.) **3**, 317 (1967).
- [24] D. E. Logan, Y. H. Szczech, and M. A. Tusch, *Europhys. Lett.* **30**, 307 (1995).
- [25] M. Cyrot, in: *Electron correlation and magnetism in narrow-band systems*, ed. by T. Moriya (Springer, Berlin, 1981); *J. Magn. Magn. Mater.* **45**, 9 (1984).
- [26] M. Cyrot and H. Kaga, *Phys. Rev. Lett.* **77**, 5134 (1996); H. Kaga and M. Cyrot, *Phys. Rev. B* **58**, 12267 (1998).
- [27] M. Wortis, in *Phase Transitions and Critical Phenomena*, Vol. 3, ed. by C. Domb and M. S. Green (Academic, London, 1974), p. 114.
- [28] V. G. Vaks, A. I. Larkin, and S. A. Pikin, *Sov. Phys. – JETP* **24**, 240 (1967) [*Zh. Eksp. Teor. Fiz.* **51**, 361 (1966)].
- [29] G. Horwitz, H. B. Callen, *Phys. Rev.* **124**, 1757 (1961).
- [30] K. Chen, A. M. Ferrenberg, D. P. Landau, *Phys. Rev. B* **48**, 3249 (1993).

## Chapter 5

# First principles analysis of spin-disorder resistivity

In this chapter spin-disorder resistivity of Fe and Ni and its temperature dependence are analyzed using noncollinear density functional calculations within the supercell method. Different models of thermal spin disorder are considered, including the mean-field approximation and the nearest-neighbor Heisenberg model. Spin-disorder resistivity is found to depend weakly on magnetic short-range order. If the local moments are kept frozen at their zero-temperature values, very good agreement with experiment is obtained for Fe, but for Ni the resistivity at elevated temperatures is significantly overestimated. Agreement with experiment for Fe is improved if the local moments are iterated to self-consistency. The overestimation of the resistivity for paramagnetic Ni is attributed to the reduction of the local moments down to  $0.35\mu_B$ . Overall, the results suggest that low-energy spin fluctuations in Fe and Ni are better viewed as classical rotations of local moments rather than quantized spin fluctuations that would require an  $(S + 1)/S$  correction.

### 5.1 Introduction

Electron scattering off of spin fluctuations in magnetic metals results in an “anomalous” contribution to electric resistivity [1, 2, 3]. The analysis of this spin-disorder resistivity is of interest because it can provide material-specific information on the character of spin fluctuations which is not easily accessible by other means. Scattering on spin disorder is also an important factor degrading the performance of magnetoresistive nanostructures in spintronic devices.

The magnitude of the spin-disorder contribution to resistivity is comparable to the phonon contribution near and above the Curie temperature  $T_c$  [1]. (The magnetic scattering amplitudes have no small parameter unless the local moments are small.) It is usually assumed that the spin-disorder resistivity is constant well above  $T_c$ . In this region, Matthiessen’s rule is valid, and the phonon contribution can be fitted

to the Bloch-Grüneisen formula. The excess resistivity in the whole temperature range may be attributed to spin disorder [4], although one may expect deviations from Matthiessen’s rule at low temperatures where transport is carried by weakly interacting spin channels [5]. In addition, it was argued that in some cases (such as Ni) spin disorder may change the character of states on the Fermi level and thereby appreciably change the phonon contribution itself [1, 2].

Many authors have studied spin-disorder resistivity theoretically using the  $s$ - $d$  model Hamiltonian [6, 7, 8, 9]. In this approach the  $3d$  shells in transition metals (or  $f$  shells in rare earth metallic magnets) are assumed to be localized at atomic sites and partially filled, forming magnetic moments  $\hat{\mathbf{S}}_i$  that are coupled to the current-carrying conduction electrons by exchange interaction  $H_{sd} = -J_{sd} \sum_i \hat{\mathbf{S}}_i \hat{\mathbf{s}}_i$ , where  $J_{sd}$  is the local  $s$ - $d$  exchange coupling constant and  $\hat{\mathbf{s}}_i$  the spin-density operator of the conduction electrons at site  $i$ . Thermal fluctuations of the  $d$ -electron spins generate an inhomogeneous exchange potential; in the Born approximation the spin-disorder resistivity is then determined by the conduction electron band structure and the spin-spin correlation functions of  $d$ -electron spins [9]. If the scattering is approximated as being elastic, only equal-time spin correlators have to be considered. Further, if the mean-field approximation is used for  $3d$  spin statistics, the spin-disorder resistivity behaves as  $\rho_{\text{mag}}(T) = \rho_0[1 - M^2(T)/S(S+1)]$ , where  $M(T) = \langle \mathbf{S}(T) \rangle$  is the magnetization at temperature  $T$  and  $\rho_0 \propto J_{sd}^2 S(S+1)$  [6]. Note that above  $T_c$  spin-disorder resistivity is constant and equal to  $\rho_0$ . The shape of the Fermi surface of conduction electrons is immaterial to this prediction as long as the scattering is elastic [9].

The effects of magnetic short-range order on the spin-disorder resistivity have also been investigated within the  $s$ - $d$  model [7,8,10-15]. This problem has attracted considerable attention in connection with a “bump” in the resistivity that is observed near  $T_c$  in some magnetic metals (although it is usually quite small) [1]. The analysis of critical magnetic short-range order effects showed that a cusp may appear near  $T_c$  due to long-wave critical fluctuations [7], although it should usually be strongly suppressed by finite mean-free path and cancelations due to Fermi surface integration [10]. It was also found that the effect of magnetic short-range order and even its sign are sensitive to such details of the model as the conduction band occupation and the form of the scattering (pseudo)potential [12, 13, 14].

Although the  $s$ - $d$  model provided physical insight into the mechanism of spin-disorder resistivity, it suffers from serious limitations. First, the distinction between localized and conduction electrons is not justified in transition metals where  $3d$  electrons are itinerant and form the Fermi surface. Even if the current is dominated by light  $s$ -like bands that can be distinguished from heavy  $d$ -like bands, the relaxation rate is dominated by interband ( $s$ - $d$ ) scattering [16]. Second, at elevated temperatures the scattering potential generated by spin disorder is of the order of the exchange splitting, which is not small compared to the bandwidth. This invalidates the Born approximation which is usually made in model calculations. Third, the  $s$ - $d$  model does not properly take into account the change of electronic structure due to disorder.

The first-principles approach to the spin-disorder resistivity is free from all these

limitations and can be used for quantitative calculations of spin-disorder resistivity. This is of particular interest for the theory of itinerant magnets, because, as mentioned above, spin-disorder resistivity depends on spin-spin correlation functions. Different theories of itinerant magnetism make conflicting predictions for such properties as the degree of magnetic short-range order, the mean-squared magnetic moment, and their temperature dependence [17-21]; these quantities are quite hard to measure directly. By calculating spin-disorder resistivity for a particular model of spin fluctuations and comparing the results with experiment, one can attempt to validate or rule out different spin-fluctuation models.

## 5.2 General approach and methods

Our approach is based on noncollinear density functional theory (DFT). All the valence electrons are treated on the same footing, while the scattering potentials are determined by the self-consistent electron charge and spin densities. We used the TB-LMTO method [23], which represents the electronic density of the crystal as a superposition of overlapping atomic spheres; the electronic density inside each sphere is spherically symmetric. This method is known to work very well in close-packed materials, and it allows us to introduce spin disorder in various ways. In this work we used the rigid spin approximation which assumes that the spin density in each atomic sphere remains collinear, while the spin densities of different atomic spheres become noncollinear at finite temperatures. In the simplest model the electron charge and spin densities in all atomic spheres were taken from the ground state and frozen, while the directions of the spin moments in different spheres are randomized with the angular distribution function taken from mean-field approximation at the given temperature. This model is expected to work reasonably well for Fe which has a fairly stable local moment [24]. In Section 5.3 we show that this is indeed the case; however, for Ni the paramagnetic spin-disorder resistivity calculated in this way is about twice too large. In order to explain this discrepancy, the dependence of the spin-disorder resistivity on the degree of magnetic short-range order and on the magnitude of the local moment is studied in Sections 5.4 and 5.5.

We use the supercell approach and calculate the areal conductance of a layer of spin-disordered metal FM(D) sandwiched between fully ordered semi-infinite leads FM(O) made of the same metal (see Figure 5.1). The resistivity is then proportional to the slope of the inverse conductance as a function of the disordered layer thickness, once the Ohmic limit is reached. For the given thickness of the FM(D) layer, the conductance of the system was averaged over several disorder configurations (typically 15). The planar system is represented by a laterally periodic prism with an axis along the [001] crystallographic direction, and care is taken to make sure that the conductance scales as the cross-section of the prism. To calculate the conductance, we used the principal-layer Green's function technique [25, 26] and the Landauer-Büttiker formalism [27] in the implementation allowing for noncollinearity

in the active region [28]. This technique was employed before to study the effects of substitutional disorder on transport in magnetic multilayers [29]; it is similar to the supercell Kubo-Greenwood method used to calculate the residual resistivity of binary alloys [30]. We used experimental lattice constant both for Fe ( $a = 2.8665\text{\AA}$ ) and Ni ( $a = 3.524\text{\AA}$ ). For  $N \times N$  lateral supercell we used  $60/N \times 60/N$  uniform k-point mesh for conductance calculations both for Fe and Ni.

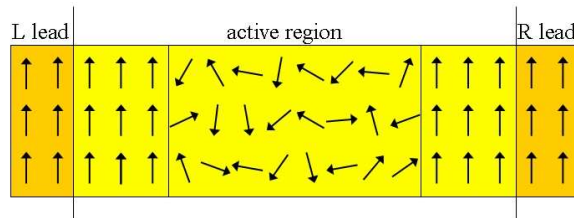


Figure 5.1: The schematic picture of the system used in the calculations. Vertical lines indicate the embedding planes.

If the atomic potentials in the supercell are not converged to self-consistency with the given spin disorder configuration, care needs to be taken to ensure local charge neutrality. Indeed, FM(D) and FM(O) materials have different Fermi levels that must normally be matched by the contact voltage. In order to enforce charge neutrality in the FM(D) region, a constant potential shift was introduced in this region so that the charge in the central part of FM(D) averaged over disorder realizations was zero. This potential shift plays the role of the contact voltage. Note that no matter how the FM(O)/FM(D) interfaces are treated (self-consistently or not), they add contact resistances to the circuit. However, since the *resistivity* of the FM(D) material is extracted from the thickness dependence of the resistance in the Ohmic limit, the simplified treatment of interfaces has no effect on the results.

## 5.3 The spin-disorder resistivity in the mean-field approximation

### 5.3.1 The paramagnetic state

In this section we analyze the temperature dependence of spin-disorder resistivity for iron and nickel using mean-field approximation for thermal spin disorder; the spin-spin correlator is purely local in this approximation. First we consider the paramagnetic state where the angular distribution function is isotropic, and the resulting spin-disorder resistivity is temperature-independent.

We needed to make a physically reasonable choice of atomic potentials for the conductance calculations. It is known that the local moments in Fe are quite stable [17]; in particular, the disordered local moment method, which employs the coherent

potential approximation for spin-disordered states, shows only a small reduction of the local moment in paramagnetic Fe compared to its ground-state value [24]. As shown below, the direct averaging of self-consistent local moments in the paramagnetic states gives a similar result. Therefore, for Fe it is reasonable to use frozen atomic potentials taken from the zero-temperature ground state in all calculations. We also checked the effect of self-consistency on spin-disorder resistivity in Fe and found it to be small (see below). The situation is entirely different for Ni, where the local moment depends on the magnetic state; in particular, it vanishes altogether in the paramagnetic disordered local moment approximation [34]. Since longitudinal spin fluctuations (that are absent in our approach) can at least partially restore the local moments [17], *a priori* it is not clear how the atomic potentials should be modified for Ni. In this section we use frozen atomic potentials; the necessary corrections are discussed later.

Figure 5.2 shows the inverse areal conductance for paramagnetic Fe and Ni as a function of the disordered FM(D) region thickness. Here, we used the frozen ground-state atomic potentials and the LMTO basis including  $s$ ,  $p$ , and  $d$  orbitals ( $l_{max} = 2$ ). The supercell cross-sections contained  $4 \times 4$  (for Fe) and  $3 \times 3$  (for Ni) cubic unit cells with edges oriented along the  $[100]$  directions. Almost perfect Ohmic behavior is apparent for both Fe and Ni, which establishes the validity of our approach.

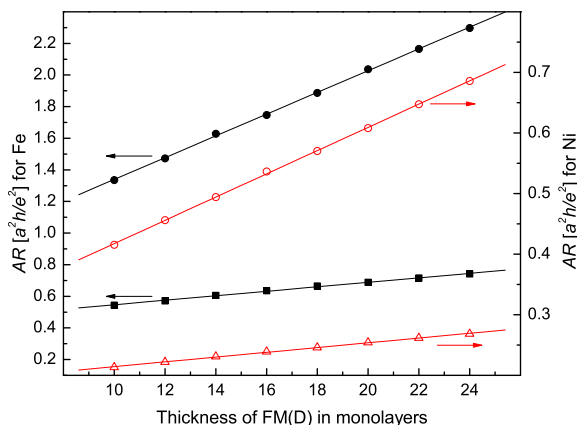


Figure 5.2: The area-resistance product  $AR$  of the FM(O)/FM(D)/FM(O) systems as a function of the FM(D) layer thickness for bcc Fe (black filled symbols) and fcc Ni (red empty symbols) obtained with  $l_{max} = 2$ . Circles and squares correspond, respectively, to the paramagnetic state and to the lowest temperature for which the calculations were made ( $T = 0.27T_c$  for Fe and  $T = 0.58T_c$  for Ni).  $4 \times 4$  and  $3 \times 3$  supercells were used for Fe and Ni, respectively, with edges along the  $[100]$  directions. Straight lines show the linear fitting; error bars are smaller than the size of the symbols.

Table 5.1 lists the values of spin-disorder resistivity found for paramagnetic Fe and Ni using different supercell cross-sections, LMTO bases truncated at  $l_{max} = 2$

Table 5.1: Spin-disorder resistivity in  $\mu\Omega\cdot\text{cm}$  for paramagnetic bcc Fe and fcc Ni. The calculated values are given for basis sets with  $l_{max} = 2$  and 3, as well as for different lateral cell sizes with edges along the [100] directions. SC denotes calculations with self-consistent potentials. Standard deviations of spin-disorder resistivity due to limited disorder sampling are included.

Metal and basis	$M, \mu_B$	$2 \times 2$	$3 \times 3$	$4 \times 4$	Exp.[4]
Fe: $l_{max} = 2$	2.29	$106 \pm 1.8$	$101 \pm 1.3$	$102 \pm 1.0$	80
Fe: $l_{max} = 3$	2.22	$86 \pm 1.6$	$87 \pm 7.1$	$85 \pm 7.4$	80
Fe: $l_{max} = 2$ , SC	2.21	$88 \pm 3.7$			80
Ni: $l_{max} = 2$	0.66	$34 \pm 0.6$	$35 \pm 0.4$		15
Ni: $l_{max} = 3$	0.63	$29 \pm 0.6$			15

and  $l_{max} = 3$  (the latter includes  $f$  orbitals), as well as the value found using self-consistent (rather than frozen) atomic potentials for Fe. It is seen that the results are well converged with respect to the supercell cross-section, and even  $2 \times 2$  supercells provide sufficient accuracy. This is reasonable because the mean-free path in the paramagnetic state is small.

The calculations with self-consistent atomic potentials were performed as follows. In order to reduce the statistical error, the averaging of the conductance was performed using the same sets of random spin disorder configurations as in the calculation with frozen potentials. For each individual spin configuration the atomic potentials were iterated to self-consistency using the Fermi distribution function corresponding to the experimental  $T_c$  of Fe. For a  $2 \times 2$  lateral cell for Fe, we used a  $6 \times 6 \times 1$  k-point grid. The resulting distribution of the sites over the magnitude of the local magnetic moment is shown in Figure 5.3; the distribution is Gaussian with a rather small width. The average local moment is only reduced by 3 – 4% from its ground state value. This small reduction appears to be similar to the disordered local moment calculations of Ref. [20], while Ref. [24] obtained a somewhat larger reduction. The self-consistent density of states (not shown) is very similar to the one generated by the frozen ground-state atomic potentials (see Figure 5.4e below).

The addition of  $f$  orbitals to the LMTO basis reduces the calculated spin-disorder resistivity by approximately 15% for both Fe and Ni. Self-consistency in the paramagnetic state of Fe results in a similar reduction. This similarity suggests that the main reason for this spin-disorder resistivity decrease is the reduction of the local moment, which is, incidentally, very similar in both cases. In order to check this, we performed additional calculations for Fe in which the  $f$  channel was added to the basis while the charge density was kept unchanged from the self-consistent one with  $l_{max} = 2$ . For the frozen potential case, spin-disorder resistivity reduced slightly from 106 to 100  $\mu\Omega\cdot\text{cm}$ ; for the self-consistent paramagnetic case, it only reduced from 88 to 86  $\mu\Omega\cdot\text{cm}$ , which is within the error bar. Thus, the effect of  $l_{max}$  *per se* on spin-disorder resistivity is very small for Fe. This is somewhat different from the binary alloy systems considered by other authors using both TB-LMTO and KKR

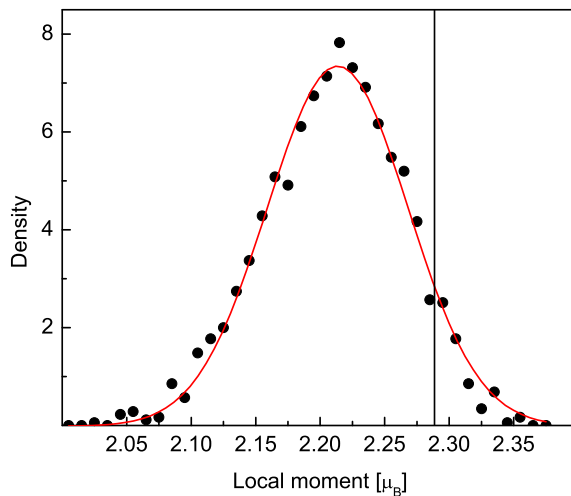


Figure 5.3: Distribution of the local magnetic moment in self-consistent fully spin-disordered bcc Fe. The Fermi temperature is equal to the experimental  $T_c$ . The vertical line shows the local moment at  $T = 0$ . The red (solid) curve shows the Gaussian fit to the data.

(Korringa-Kohn-Rostocker) methods, where a larger effect of adding  $f$  states was found [31, 32]. In view of the weak dependence of spin-disorder resistivity on  $l_{max}$ , below we use  $l_{max} = 2$  in all calculations for  $T < T_c$ .

The experimental estimates of the spin-disorder resistivity in the paramagnetic state [4] are listed in the last column of Table 5.1. The agreement with experiment for Fe is quite satisfactory, and it is in fact improved if the reduction of the local moment is included. In Ni the spin-disorder resistivity calculated with frozen atomic potentials is overestimated by a factor of 2. This is not surprising, because, as mentioned above, the use of frozen atomic potentials is not justified for Ni. In order to understand the origins of the disagreement with experiment for Ni, possible modifications of the statistical model for the paramagnetic state must be considered; this is done below in Sections 5.4 and 5.5.

Recently, Buruzs *et al.* [33] calculated the spin-disorder resistivity for Fe and Co using the disordered local moment approach within the Korringa-Kohn-Rostocker method and found that their method significantly overestimates the paramagnetic spin-disorder resistivity in these metals. The source of disagreement with our supercell method for Fe is unknown to us.

### 5.3.2 The temperature dependence in the ferromagnetic state

In this section we consider ferromagnetic state of Fe and Ni. We use frozen ground-state potentials and the basis with  $l_{max} = 2$ . As mentioned above, this approximation is reasonable for Fe, while for Ni it is not applicable at high temperatures; nevertheless,

comparison of these two systems will allow us to draw important conclusions. For the ferromagnetic state the spin configurations were generated using the mean-field distribution function

$$p(\theta) \propto e^{-\mathbf{H}_{\text{eff}} \cdot \boldsymbol{\mu} / T}, \quad H_{\text{eff}}(T) = \frac{3M(T)T_c}{\mu M(0)} \quad (5.1)$$

where  $\theta$  is the angle between the local moment  $\boldsymbol{\mu}$  and the magnetization axis,  $M(T)$  is the magnetization at temperature  $T$  in mean-field approximation, and  $\mathbf{H}_{\text{eff}}$  is the Weiss field. This distribution function depends only on  $T/T_c$ .

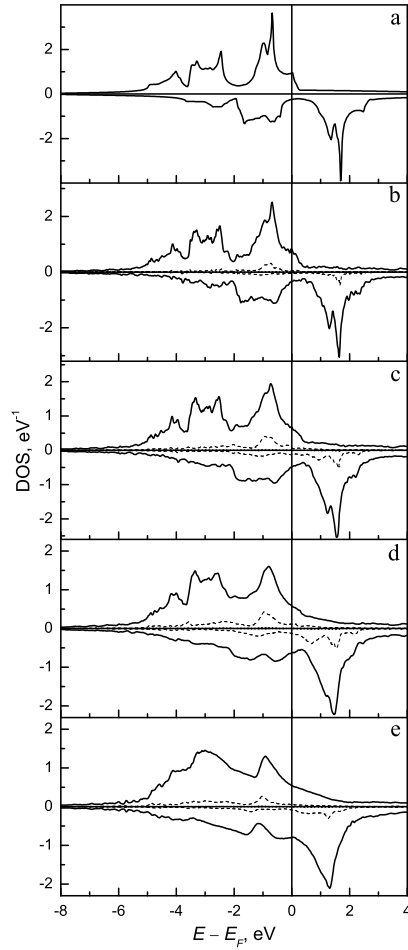


Figure 5.4: Spin-resolved density of states (solid lines) for bcc Fe averaged over random spin configurations with the mean-field distribution function (5.1); (a)  $T = 0$ , (b)  $T = 0.25T_c$ , (c)  $T = 0.5T_c$ , (d)  $T = 0.75T_c$ , and (e)  $T = T_c$ . Dashed lines show the mean-square deviation of the DOS on a given site from its ensemble average.

Before we turn to the temperature dependence of spin-disorder resistivity, let us look at the electronic structure of Fe and Ni with spin disorder. The spin-resolved

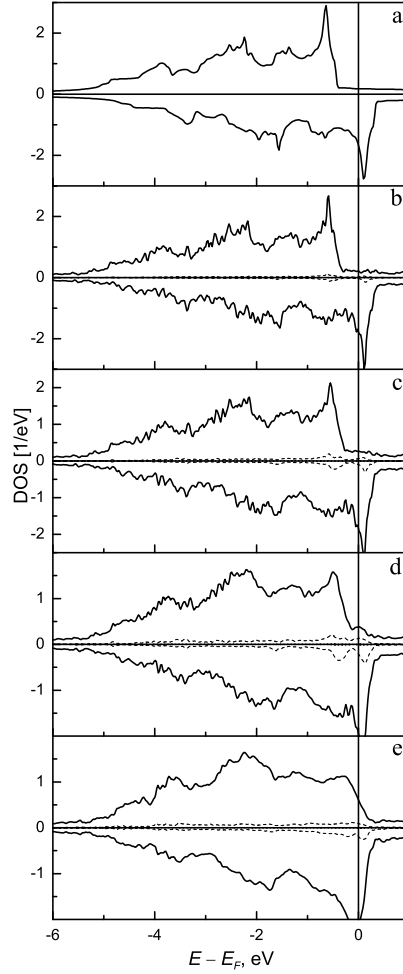


Figure 5.5: Same as in Fig. 5.4 but for fcc Ni.

DOS of Fe and Ni is shown in Figures 5.4 and 5.5 for several temperatures. These data were obtained by projecting the site-resolved DOS onto local spin-up and spin-down states (in the local reference frame where the  $z$  axis is parallel to the local moment) and subsequent averaging over bulk-like sites and spin disorder configurations generated according to Equation (5.1). The paramagnetic DOS of Fe is very similar to the KKR disordered local moment results [24]. As the temperature is increased from 0 to  $T_c$ , the spin-up and spin-down states randomly hybridize with each other, the peaks broaden, and the van Hove singularities are washed out. The mean-squared deviation of the DOS from its average (shown by dashed lines) is quite small, which is a direct consequence of the large coordination number. In Fe the spin splitting is almost independent on temperature, while in Ni it is much reduced as  $T$  gets close to  $T_c$ . Note that the frozen atomic potentials in Ni are very far from self-consistency at elevated temperatures, but a self-consistent treatment neglecting longitudinal spin

fluctuations would be meaningless. We will return to this issue in Section 5.5.

Let us now discuss the temperature dependence of the spin-disorder resistivity. While we found above that  $2 \times 2$  supercells were sufficiently large for the paramagnetic state, additional care needs to be taken at lower temperatures where the mean-free path becomes longer. We found that  $4 \times 4$  supercells for Fe and  $3 \times 3$  for Ni demonstrate linear dependence of the conductance on the length of the supercell for all temperatures down to about  $T_c/3$  (see Figure 5.2). This behavior agreed with a simple mean-free path estimate using the free-electron formula  $l = \frac{3}{4}AR_{\text{bal}}/\rho$ , where  $AR_{\text{bal}}$  is the ballistic area-resistance product;  $l$  does not exceed the lateral cell size in this temperature range. Another indication of the Ohmic behavior comes from the distribution of the current over the spin channels. The conductance of the FM(O)/FM(D)/FM(O) system is a sum of four partial conductances,  $G_{\uparrow\uparrow}$ ,  $G_{\downarrow\downarrow}$ ,  $G_{\uparrow\downarrow}$ ,  $G_{\downarrow\uparrow}$  (the latter two are equal). Spin-conserving and spin-flip scattering have similar rates in our spin-disorder problem (as long as the temperature is not too low), and therefore the electrons “forget” their spin over their mean-free path. Therefore, in the Ohmic limit the partial conductances must be proportional to the number of channels in the left and right leads for the corresponding spin channels:  $G_{\sigma\sigma'} \propto M_{\sigma}^L M_{\sigma'}^R$ . This implies that in this regime we should have  $G_{\uparrow\uparrow}G_{\downarrow\downarrow} = G_{\uparrow\downarrow}G_{\downarrow\uparrow}$ . This relation does indeed hold down to  $T \sim T_c/3$  unless the thicknesses of the FM(D) region is very small.

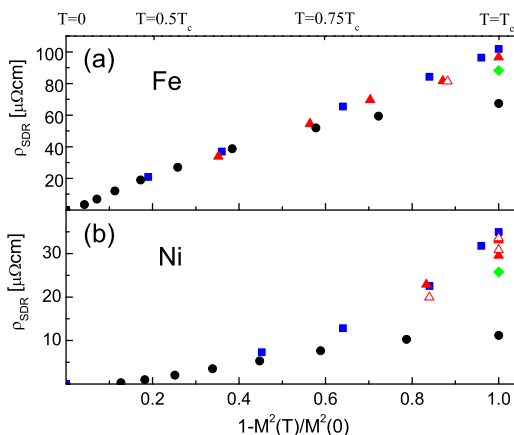


Figure 5.6: Dependence of spin-disorder resistivity on the magnetization for (a) Fe, and (b) Ni. Black circles denote experimental data combining Ref. [4] for  $\rho_{\text{mag}}(T)$  and Ref. [40] for  $M(T)$ . Blue squares show mean-field calculations, filled red triangles denote Monte Carlo results, and green diamonds show reverse Monte Carlo calculations. The empty red triangles show Monte Carlo results with larger cells:  $6 \times 6$  for Fe and  $4 \times 4$  for Ni. The upper axis shows temperatures corresponding to the given magnetization in mean-field approximation. The error bars show statistical uncertainties where they exceed the size of the symbols. All results are for  $l_{\text{max}} = 2$ .

The dependence of the calculated spin-disorder resistivity for Fe and Ni on the magnetization is plotted in Figure 5.6 along with the experimental data [4] (those plots for  $M(T)$  were taken from Ref. [40]). The results for Fe agree rather well with experiment (see also Table 5.1, especially at lower temperatures where the magnetic excitations are dominated by spin waves and our classical approach is, strictly speaking, invalid. This surprising finding is due to the fact that spin-disorder resistivity in Figure 5.6 is plotted as a function of the long-range order parameter and that, as we show below in Section 5.4, the spin-disorder resistivity in Fe is insensitive to magnetic short-range order. The calculated spin-disorder resistivity exhibits linear dependence on  $M^2(T)$  up to  $T_c$ , while the experimental data deviate downward from the straight line. This deviation may be attributed to a small reduction of the local moment at elevated temperatures, as discussed in the previous section.

For Ni the low-temperature region could not be accessed due to the increased mean-free path. Still, the agreement with experiment at lower temperatures is good, while at higher temperatures the calculated spin-disorder resistivity strongly deviates upwards from experimental data. This deviation indicates the inadequacy of our spin fluctuation model; its possible modifications are studied in the following sections.

The qualitative features of the *calculated* temperature dependence of spin-disorder resistivity (with frozen atomic potentials) are different for Fe and Ni. It is seen in Figure 5.6 that for Fe the spin-disorder resistivity is proportional to  $1 - M^2(T)/M^2(0)$  in agreement with the predictions of the *s-d* model if spin fluctuations are treated classically. On the other hand, for Ni this relation does not hold. As mentioned in the Introduction, the change of electronic structure due to spin disorder may lead to deviations from *s-d* model predictions.

As seen in Figures 5.4 and 5.5, the densities of states change quite appreciably with temperature for both Fe and Ni. Therefore, it may seem surprising that for Fe the temperature dependence of spin-disorder resistivity agrees with the *s-d* model. Still, one can understand the difference between Fe and Ni using the following considerations. First, as seen in Figure 5.5, the exchange splitting in Ni is strongly reduced at elevated temperatures, which results in the lifting of the heavy majority-spin  $3d$  bands up to the Fermi level. Scattering into these final states from the light bands becomes possible, which decreases the lifetime of the latter. This mechanism was invoked by Mott [2] to argue that the reduction of the spin splitting in Ni can result in an anomalous temperature dependence of the *phonon* resistivity. The same argument applies to spin-disorder resistivity considered here. According to Figure 5.5, this happens approximately at  $T = 0.75T_c$ , which roughly corresponds to the upturn of spin-disorder resistivity seen in Figure 5.6b. On the other hand, for Fe, as seen in Figure 5.4, the exchange splitting is constant and no new bands appear at the Fermi level. Consequently, no additional temperature dependence is introduced and spin-disorder resistivity scales as  $1 - M^2(T)/M^2(0)$ .

While plausible, the above arguments are not conclusive, because they assume without proof that the scattering matrix elements between the light and heavy bands are large. On a more subtle level, one may speculate that the difference between

Fe and Ni can be understood based on the relation between disorder broadening and spin splitting. At the given wavevector, the spectral function consists of delta-function peaks corresponding to majority and minority-spin states. In the presence of spin disorder, the spin states on neighboring sites are allowed to hybridize with random matrix elements, and the delta-function peaks broaden. At low temperature the broadening is small, and the peaks corresponding to different spins are well separated in energy from each other. However, at higher temperatures some of these peaks can merge and form common, “virtual-crystal-like” bands. Calculations of the paramagnetic spectral functions using the disordered local moment method indicate that in Fe the majority and minority-spin states remain separated through large portions of the Fermi surface even above  $T_c$  [35]. On the other hand, in Ni the majority and minority-spin states are mixed in the paramagnetic state [35]. Therefore, at certain temperature below  $T_c$  there is a crossover from separated to mixed-spin bands. The lifetime is expected to decrease as the bands merge, which again explains the upturn of spin-disorder resistivity from the straight line in Figure 5.6b.

## 5.4 Effect of magnetic short-range order

As mentioned above, short-range order can sometimes have a significant effect on resistivity. In this section we analyze the effect of the magnetic short-range order on the spin-disorder resistivity in Fe and Ni. In particular, it is important to check whether the large disagreement with experiment for Ni found in Section 5.3 can be due to the use of the mean-field approximation which neglects the magnetic short-range order. This is especially interesting because a strong magnetic short-range order in Ni has been suggested by some experiments [36, 17] and theories [18, 19].

We studied the effect of the magnetic short-range order on the spin-disorder resistivity using the Monte Carlo method for the classical Heisenberg model with nearest-neighbor exchange interaction on bcc and fcc lattices (for Fe and Ni, respectively). For a given temperature we built a Monte Carlo supercell of the size of the disordered region (FM(D)). For Fe the lateral size of the FM(D) was mainly  $4 \times 4$  while for Ni we used both  $4 \times 4$  and  $3 \times 3$  lateral sizes. On the other hand, the thickness of FM(D) was varied in order to determine the resistivity as described above. Monte Carlo simulations were performed on such created supercells using periodic boundary conditions and standard Metropolis algorithm [37, 38]. Care was taken to equilibrate the system (usually 20000 Monte Carlo steps per site was discarded for equilibration) and subsequently several independent spin configurations (the spin configurations were usually 10000 Monte Carlo steps per site apart) were produced. These spin configurations, which contain magnetic short-range order, were then used to calculate the spin-disorder resistivity as described above. In order to reduce FM(O)/FM(D) interface resistance (and thus the variance of the resistance) we rotated the magnetization of the disordered spin structures to have the same direction as in the ordered region (FM(O)). Similarly as in the case of the mean-field approximation the linear

Table 5.2: Spin-spin correlators  $C_{0i}$  for the first three shells of nearest neighbors ( $i = 1, 2, 3$ ), the local correlator ( $i = 0$ ), and the effective temperature are shown for Fe and Ni for each considered temperature in Monte Carlo (MC) simulations and for reverse Monte Carlo (RMC) method. The values of spin-disorder resistivity are compared with mean-field approximation (MFA) results corresponding to the same  $M^2$ . The listed uncertainties are due to the limited disorder sampling.

Metal, cross-section	$T/T_c$	$T_{eff}/T_c$	$C_{0i} = \langle \mathbf{e}_0 \mathbf{e}_i \rangle - \langle \mathbf{e}_0 \rangle \langle \mathbf{e}_i \rangle$				$\rho_{mag}, \mu\Omega \cdot \text{cm}$	
			$i = 0$	$i = 1$	$i = 2$	$i = 3$	MC or RMC	MFA
Fe, $4 \times 4$	$\infty$	$\infty$	1	0	0	0	$101.9 \pm 1.0$	$101.9 \pm 1.0$
Fe, $4 \times 4$	1.217	1.177	1.000	0.184	0.110	0.073	$96.6 \pm 1.9$	$101.9 \pm 1.0$
Fe, $4 \times 4$	0.974	0.958	0.871	0.206	0.144	0.111	$81.6 \pm 2.1$	$88.1 \pm 0.5$
Fe, $6 \times 6$	0.974	0.965	0.882	0.209	0.144	0.112	$81.4 \pm 2.3$	$88.9 \pm 0.5$
Fe, $4 \times 4$	0.852	0.848	0.703	0.156	0.107	0.079	$69.6 \pm 1.8$	$71.3 \pm 0.4$
Fe, $4 \times 4$	0.730	0.724	0.564	0.126	0.087	0.066	$54.6 \pm 1.8$	$57.5 \pm 0.3$
Fe, $4 \times 4$	0.487	0.482	0.352	0.083	0.059	0.045	$33.8 \pm 0.7$	$35.8 \pm 0.2$
Fe, $4 \times 4$	RMC	RMC	1.000	0.309	0.167	0.060	$88.2 \pm 1.3$	$101.9 \pm 1.0$
Ni, $3 \times 3$	$\infty$	$\infty$	1	0	0	0	$34.9 \pm 0.4$	$34.9 \pm 0.4$
Ni, $3 \times 3$	1.269	1.234	1.000	0.146	0.071	0.052	$33.1 \pm 0.8$	$34.9 \pm 0.4$
Ni, $4 \times 4$	1.269	1.262	1.000	0.140	0.064	0.045	$33.6 \pm 0.7$	$34.9 \pm 0.4$
Ni, $3 \times 3$	1.110	1.063	1.000	0.205	0.129	0.104	$29.5 \pm 1.3$	$34.9 \pm 0.4$
Ni, $4 \times 4$	1.110	1.089	1.000	0.190	0.110	0.087	$30.8 \pm 1.2$	$34.9 \pm 0.4$
Ni, $3 \times 3$	0.952	0.943	0.833	0.172	0.104	0.086	$22.9 \pm 0.9$	$22.4 \pm 0.6$
Ni, $4 \times 4$	0.952	0.947	0.841	0.175	0.106	0.085	$19.9 \pm 1.3$	$22.7 \pm 0.6$
Ni, $4 \times 4$	RMC	RMC	1.000	0.335	0.140	0.114	$25.8 \pm 0.8$	$34.9 \pm 0.4$

dependence of resistance as a function of thickness of FM(D) was observed.

In order to study the effect of the magnetic short-range order on the spin-disorder resistivity we needed to compare the results obtained in mean-field approximation with those found from Monte Carlo, for the same values of the long-range order parameter ( $M^2(T)/M(0)$ ). However, since relatively small supercells were used in the Monte Carlo simulations, the corresponding magnetization is not well defined. In particular, it changes quite appreciably as we increase the thickness of FM(D) keeping the same temperature. There are two reasons for this behavior. First, by varying the length of the supercell we essentially change the cut-off for correlations which change the behavior of the system. Second, in the case of Heisenberg model in zero magnetic field the average magnetization is actually zero and instead we calculate square root of average magnetization square [37]. It can be shown that this root mean square magnetization differs from the actual magnetization by the term of the order of  $1/N$  where  $N$  is the number of atoms in the supercell. Consequently,  $M^2(T)/M(0)$  determined from Monte Carlo simulations changes with length of the supercell. Due to above ambiguities we follow a different route to determine a long-range order param-

eter from Monte Carlo simulations. We made an ansatz that for any temperature, the spin-disorder resistivity is entirely determined by the first few disconnected correlators  $\langle \mathbf{e}_0 \cdot \mathbf{e}_i \rangle$ . This is a very plausible assumption because long-distance correlation between spins are suppressed due to finite mean-free path and cancelations in Fermi surface integration [10]. Since disconnected correlators are local quantities, as far as we are away from the critical region, they don't change significantly as we increase the length of the supercell which makes them well defined quantities. The long-range order parameter can be then found from value obtained from the infinite lattice limit corresponding to the same disconnected correlators. More specifically, for a  $L \times L$  lateral size of the supercell and for a given temperature we found first three disconnected correlators from the Monte Carlo simulations on a  $L \times L \times L$  cubic supercell. For all considered temperatures we found that these correlators were very close to the ones obtained for the same temperature from supercells of different lengths from spin configurations that were actually used in transport calculations. This is due to the fact that none of the considered temperatures were in immediate proximity of the critical point. For the same reason these correlators were just slightly larger from the infinite lattice correlators corresponding to the same temperature (both for bcc and fcc lattices the infinite lattice correlators were obtained from  $12 \times 12 \times 12$  supercell for which we found that correlators are already saturated for all considered temperatures). Nevertheless, we accounted for this small difference by defining an effective temperature for which first three correlators calculated from  $12 \times 12 \times 12$  supercell are equal to the corresponding correlators obtained from a  $L \times L \times L$  supercell for the actual temperature (the effective temperature obtained from different correlators in most cases agreed, if there was small difference we chose the effective temperature as obtained from the first correlator). In all cases the effective temperature was just slightly smaller than the actual temperature. Finally, we found the value of  $M^2(T)/M(0)$  corresponding to the effective temperature. First we found  $T_c$  using the fourth order cumulant method [38]. If the effective temperature is above  $T_c$  then the magnetization was set to zero, otherwise we found the value of magnetization using finite-size scaling. Since we are away from the critical region, we assumed in most cases a simple scaling form  $M_L^2(T)/M(0) = M_\infty^2(T)/M(0) + A/N$  where  $N$  is a number of atoms and  $A$  is some constant. Using  $L = 8, 10, 12, 14$  for both bcc and fcc lattices we found that this scaling form holds.

Figure 5.6 shows the dependence of the spin-disorder resistivity as a function of the onsite correlator  $(1 - M^2(T)/M(0))$  obtained using Monte Carlo method. In addition, the magnitude of magnetic short-range order is illustrated in Table 5.2 where the connected spin-spin correlators for the first three shells of nearest neighbors are shown. In general, Monte Carlo results for spin-disorder resistivity are very close to mean-field approximation results corresponding to the same magnetization, in spite of the presence of magnetic short-range order in the Monte Carlo model. This is especially true for Fe where the effect of magnetic short-range order is almost negligible and only at higher temperature where magnetic short-range order is larger we can observe slight decrease of spin-disorder resistivity due to magnetic short-range

order. In the case of Ni magnetic short-range order also leads to rather small decrease of spin-disorder resistivity which is however noticeably larger than for Fe. Note that in general magnetic short-range order in nearest-neighbor Heisenberg model is weaker for fcc lattice than for bcc (see Table 5.2) due to larger coordination number of fcc lattice. This indicates that while the effect of magnetic short-range order on spin-disorder resistivity remains small in Ni it is stronger than in the case of Fe. We also performed additional calculations for Fe with larger cell cross-sections ( $6 \times 6$ ) in order to check whether there are any other effect due to relatively small size of the supercells. In this case the effective temperature is equal to the actual temperature and magnetization doesn't change so strongly as we vary the thickness of FM(D) region. The results is shown as an empty triangle in Figure 5.6a. Since in this point is very close to the critical temperature, the magnetization was determined assuming  $M \propto N^{-\beta/\nu}$  where critical exponents were taken from Ref. [39]. Even though in this case, the magnetic short-range order is quite large as seen in Table 5.2, its effect on the spin-disorder resistivity remains small.

These results clearly show that the magnetic short-range order characteristic for the nearest-neighbor Heisenberg model has very small effect on the spin-disorder resistivity in Fe and Ni. While the magnetic short-range order in the nearest-neighbor Heisenberg model for the close-packed lattices considered here is not strong, it is seen that its effect on the spin-disorder resistivity is much smaller even compared with the values of the nearest-neighbor spin-spin correlators. This insensitivity is likely due to the averaging over all the electronic states on the Fermi surface [10], which should be very effective in destroying the interference from scattering at different sites in transition metals with complicated Fermi surfaces. In fact, this averaging is also responsible for the small standard deviation of the local DOS from its mean (Figure 5.4) and justifies the disordered local moment approach for transition metals.

The spin-spin correlation function in real materials may be more complicated than in the nearest-neighbor Heisenberg model. However, if the interaction has a longer range while remaining mainly ferromagnetic, the magnetic short-range order must be *weaker* compared to the nearest-neighbor model [41]. First-principles calculations for both ferromagnetic and paramagnetic nickel show that the exchange parameters beyond nearest neighbors, while being much smaller than the dominant the nearest-neighbor exchange, stay mainly ferromagnetic [42, 20]. Interaction of this kind can not support stronger a magnetic short-range order compared to the nearest-neighbor Heisenberg model.

Nevertheless it is of interest to study whether the magnetic short-range order that is stronger than in nearest-neighbor Heisenberg model can have more pronounced effect on the spin-disorder resistivity. For this purpose we used the reverse Monte Carlo method [43] to produce a set of spin configurations with zero magnetization and deliberately targeting strong the magnetic short-range order in the nearest-neighbor shell. Due to geometrical constraints, the spin-spin correlators in different neighbor shells are not independent. We found it quite difficult to produce strongly correlated nearest neighbors and at the same time avoid unphysical artifacts in the long-range

behavior of the correlation function. The spin-spin correlators for the first three shells of neighbors in our reverse Monte Carlo model are listed in Table 5.2. The corresponding values of the spin-disorder resistivity calculated for Fe and Ni with this set of spin configurations are also listed in Table 5.2 and shown by full and empty diamonds in Figure 5.6. Here we used  $4 \times 4$  supercells for both Fe and Ni and checked for finite-size effects using  $6 \times 6$  supercells for Fe (essentially no difference was observed compared to  $4 \times 4$  cells). As seen in Table 5.2, the magnetic short-range order in this model is significantly stronger compared to the nearest-neighbor Heisenberg model. The effect of this strong magnetic short-range order leads to larger decrease of spin-disorder resistivity as compared with Monte Carlo results however it is still relatively small; the spin-disorder resistivity is reduced compared to its mean-field approximation values by 12% for Fe and 22% for Ni.

## 5.5 The effect of the local moment reduction

Reduction of the local moment is a universal feature of itinerant magnets as revealed by spin fluctuations theories [17]. As discussed in Section 5.3, the local moment in Fe is very stable and changes only slightly in the paramagnetic state compared to zero temperature. Therefore, our calculations based on the ground-state value of the local moment agree well with experiment for Fe. Still, the spin-disorder resistivity is sensitive to the local moment, and a small reduction of it noticeably improved the agreement with experiment at higher temperatures. Since the spin-disorder resistivity was found to be insensitive to magnetic short-range order, it is reasonable to attribute the large overestimation of the high-temperature spin-disorder resistivity in Ni to the neglect of the local moment reduction. Here we study this issue in detail.

In the paramagnetic disordered local moment state the local moment in Ni vanishes [34], but it is partially restored by longitudinal spin fluctuations [17, 20]. Following the idea of separation of low and high-energy fluctuations, we assume that the current-carrying quasiparticles near the Fermi level experience the averaged exchange-correlation field generated by fast longitudinal spin fluctuations, and that this “mean field” is adequately represented by noncollinear DFT with disordered local moments constrained to their square-averaged values. The atomic potentials are therefore obtained using the fixed spin method [44] with the value of the constrained local moment treated as an adjustable parameter, which has a physical meaning and can be measured experimentally. Other approximations are, in principle, possible; for example, the longitudinal spin fluctuations can be explicitly included in the same noncollinear DFT approach, i.e., they can be considered to be “slow” rather than “fast.” Since the separation in slow and fast degrees of freedom is not well defined, we did not attempt to study the role of these additional fluctuations.

The calculated paramagnetic spin-disorder resistivity of Ni, as a function of the local moment, is shown in Table 5.3. As seen, the spin-disorder resistivity is very sensitive to the value of the local moment. Comparison with the experimental spin-

Table 5.3: Spin-disorder resistivity in  $\mu\Omega\cdot\text{cm}$  for paramagnetic Ni as a function of the fixed local moment.  $2 \times 2$  supercells and basis sets with  $l_{max} = 2$  and  $l_{max} = 3$  were used. Standard deviations of spin-disorder resistivity due to limited disorder sampling are included.

Local moment, $\mu_B$	0.66	0.5	0.4	0.3	Exp.[4]
$l_{max} = 2$	$34 \pm 0.6$	$27 \pm 0.5$	$21 \pm 0.4$		15
$l_{max} = 3$	$29 \pm 0.6^1$	$23 \pm 0.5$	$18 \pm 0.4$	$12 \pm 0.3$	15

disorder resistivity shows that our predicted value of the square-averaged local moment in paramagnetic state of Ni is equal to  $0.35\mu_B$  (using the more accurate basis set with  $l_{max} = 3$ ). Unfortunately, we are not aware of experimental measurements suitable for comparison with this prediction.

## 5.6 Discussion and conclusions

Numerous previous studies [6, 7, 8, 9, 10] based on the  $s$ - $d$  model concluded that spin-disorder resistivity in the paramagnetic state is essentially proportional to  $J_{sd}^2 S(S+1)$  where  $S$  is the spin of the partially filled  $3d$  shell. This dependence is easy to understand based on the Fermi golden rule with averaging over the initial states of the  $3d$  spin. In our treatment based on noncollinear DFT, the exchange-correlation field with randomized directions on different sites plays the role of the  $s$ - $d$  Hamiltonian. However, contrary to the  $s$ - $d$  model, the  $3d$  spin is treated classically, i.e.,  $\mathbf{S}$  is just a classical vector and not an operator. The Fermi golden rule in our case would give a paramagnetic spin-disorder resistivity proportional to  $J_{sd}^2 S^2$ . Thus, if the  $S(S+1)$  factor were correct, noncollinear DFT calculations would underestimate the paramagnetic spin-disorder resistivity by a factor  $(S+1)/S$ . This factor is close to 2 for Fe and more than 3 for Ni. In reality, the calculated spin-disorder resistivity agrees well with experiment for Fe and is *overestimated* for Ni (if the local moment reduction is not included). We believe that these results provide clear evidence against the  $S(S+1)$  factor which appears if the local moments are treated as local atomic spins. Instead, the classical description of the local magnetic fluctuations in the spirit of the disordered local moment approach is supported by our results. We suggest that the itinerancy of the  $3d$  electrons is crucial for this behavior. Qualitatively, one can argue that the low-energy fluctuations in Fe or Ni on the scale of  $kT$  (which the resistivity is most sensitive to) are similar to classical rotations of the local moments rather than quantum fluctuations of localized spins. It would be interesting to investigate this issue for magnets with a varying degree of localization, including rare-earth systems.

Some poorly controlled assumptions are involved in the extraction of  $\rho_{\text{mag}}$  from the experimental data [4]. First, it is assumed that  $\rho_{\text{mag}}$  is constant in the wide temperature range above  $T_c$  where the total resistivity is linear in  $T$ . This assumption implies that the local moments (or at least their mean-squared average) are constant in

this range. Spin fluctuation theories for itinerant metals show that the local moments may change with temperature above  $T_c$  [17, 20, 21]. Such change will contribute to the slope of  $\rho$  above  $T_c$ , and hence the separation of  $\rho_{\text{mag}}$  from the phonon contribution would be inaccurate.

On the other hand, it has been argued that the phonon contribution to the resistivity may be sensitive to spin disorder, because the latter may change the character of states at the Fermi level [1, 2]. In particular, in Ni the filled majority-spin  $d$  states may be lifted up to the Fermi level by spin disorder, thereby facilitating interband  $s$ - $d$  scattering by phonons. This effect may therefore introduce an unusual temperature dependence of the phonon contribution, which makes spin disorder and phonon effects non-additive, even if the scattering rates themselves obey Matthiessen's rule. Since we have not studied this effect here, our comparison of spin-disorder resistivity with experiment for Ni is incomplete. However, the phonon contribution can be expected to follow the Bloch-Grüneisen form above  $T_c$  with the electron-phonon scattering renormalized by spin disorder; therefore, the influence of spin disorder on the phonon contribution should not invalidate the procedure used for subtracting this contribution above  $T_c$ .

In conclusion, we have calculated the spin-disorder resistivity of Fe and Ni in the whole temperature range up to  $T_c$  using both the mean-field approximation and the nearest-neighbor Heisenberg model to represent the canonical ensemble of classical spin configurations. We found that spin-disorder resistivity is insensitive to the magnetic short-range order in Fe and Ni. The spin-disorder resistivity in Fe depends linearly on  $M^2(T)$  which implies that the main effect of spin disorder is to introduce scattering, which is proportional to the variance of the random potential. For Ni the calculated temperature dependence is more complicated; at elevated temperatures close to  $T_c$  the spin-disorder resistivity grows faster than expected. This faster increase of spin-disorder resistivity may be explained by the reduction of the exchange splitting which lifts the heavy bands up to the Fermi level, thereby increasing the scattering rate. The results for Fe are in very good agreement with experiment if the atomic potentials are taken from zero temperature and frozen, but for Ni the spin-disorder resistivity calculated in this way is strongly overestimated. This disagreement is attributed to the reduction of the local magnetic moment in Ni. Comparison with experimental spin-disorder resistivity leads to a value of  $0.35\mu_B$  above  $T_c$ , which may be compared with experiment.

# Bibliography

- [1] B. R. Coles, *Adv. Phys.* **7**, 40 (1958).
- [2] N. F. Mott, *Adv. Phys.* **13**, 325 (1964).
- [3] S. V. Vonsovskii, *Magnetism* (Halsted Press, New York 1974).
- [4] R. J. Weiss and A. S. Marotta, *J. Phys. Chem. Solids* **9**, 302 (1959).
- [5] A. Fert and I. A. Campbell, *Phys. Rev. Lett.* **21**, 1190 (1968); *J. Phys. F: Met. Phys.* **6**, 849 (1976).
- [6] T. Kasuya, *Progr. Theor. Phys.* **16**, 58 (1956).
- [7] P. G. de Gennes and J. Friedel, *J. Phys. Chem. Solids* **4**, 71 (1958).
- [8] I. Mannari, *Progr. Theor. Phys.* **26**, 51 (1961).
- [9] S. V. Vonsovskii and Yu. Izyumov, *Sov. Phys. Uspekhi* **5**, 547 (1963).
- [10] M. E. Fisher and J. S. Langer, *Phys. Rev. Lett.* **20**, 667 (1968).
- [11] J. B. Gibson, *J. Phys. Chem. Solids* **1**, 27 (1956).
- [12] P. L. Rossiter, P. Wells, *J. Phys. C: Solid St. Phys.* **4**, 354 (1971).
- [13] S. Alexander, J. S. Helman, and I. Balberg, *Phys. Rev. B* **13**, 304 (1976).
- [14] M. Kataoka, *Phys. Rev. B* **63**, 134435 (2001).
- [15] K. Akabli and H. T. Diep, *J. Appl. Phys.* **103**, 07F307 (2008).
- [16] D. A. Goodings, *Phys. Rev.* **132**, 542 (1963).
- [17] T. Moriya, *Spin fluctuations in itinerant electron magnetism* (Springer, Berlin, 1985).
- [18] V. P. Antropov, *Phys. Rev. B* **72**, 140406 (2005).
- [19] C. S. Wang, R. E. Prange, and V. Korenman, *Phys. Rev. B* **25**, 5766 (1982).

- [20] A. V. Ruban, S. Khmelevskiy, P. Mohn, and B. Johansson, Phys. Rev. B **75**, 054402 (2007).
- [21] A. L. Wysocki, J. K. Glasbrenner, and K. D. Belashchenko, Phys. Rev. B **78**, 184419 (2008).
- [22] A. L. Wysocki, K. D. Belashchenko, J. P. Velev and M. van Schilfgaarde, J. Appl. Phys. **101**, 09G506 (2007).
- [23] O. K. Andersen, Phys. Rev. B **12**, 3060 (1975).
- [24] B. L. Gyorffy, A. J. Pindor, J. Staunton, G. M. Stocks, and H. Winter, J. Phys. F: Met. Phys. **15**, 1337 (1985).
- [25] I. Turek, V. Drchal, J. Kudrnovský, M. Šob, and P. Weinberger, *Electronic Structure of Disordered Alloys, Surfaces and Interfaces* (Kluwer, Boston, 1997).
- [26] J. Kudrnovský, V. Drchal, C. Blaas, P. Weinberger, I. Turek, and P. Bruno, Phys. Rev. B **62**, 15084 (2000).
- [27] S. Datta, *Electronic Transport in Mesoscopic Systems* (Cambridge University Press, Cambridge, 1995).
- [28] M. van Schilfgaarde (unpublished).
- [29] V. Drchal, J. Kudrnovský, P. Bruno, P. H. Dederichs, I. Turek, and P. Weinberger, Phys. Rev. B **65**, 214414 (2002).
- [30] R. H. Brown, P. B. Allen, D. M. Nicholson, and W. H. Butler, Phys. Rev. Lett. **62**, 661 (1989).
- [31] I. Turek, J. Kudrnovský, V. Drchal, L. Szunyogh, and P. Weinberger, Phys. Rev. B **65**, 125101 (2002).
- [32] J. Banhart, H. Ebert, P. Weinberger, and J. Voithländer, Phys. Rev. B **50**, 2104 (1994).
- [33] Á. Buruzs, L. Szunyogh, and P. Weinberger, Phil. Mag. **88**, 2615 (2008).
- [34] J. B. Staunton and B. L. Gyorffy, Phys. Rev. Lett. **69**, 371 (1992).
- [35] J. Staunton, B. L. Gyorffy, A. J. Pindor, G. M. Stocks, and H. Winter, J. Phys. F: Met. Phys. **15**, 1387 (1985).
- [36] H. A. Mook, J. W. Lynch, and R. M. Nicklow, Phys. Rev. Lett. **30**, 556 (1973).
- [37] M. E. J. Newman, G. T. Barkema, *Monte Carlo Methods in Statistical Physics* (Clarendon Press, Oxford, 1999).

- [38] D. P. Landau, K. Binder, *A Guide to Monte Carlo Simulations in Statistical Physics* (Cambridge University Press, Cambridge, 2000).
- [39] K. Chen, A. M. Ferrenberg, and D. P. Landau, Phys. Rev. B **48**, 3249, (1993).
- [40] J. Crangle and G. M. Goodman, Proc. R. Soc. London, Ser. A **321**, 477 (1971).
- [41] The mean-field approximation criterion of validity is  $1/z \ll 1$  where  $z$  is the effective number of neighbors inside the interaction range.
- [42] V. P. Antropov, B. N. Harmon, and A. N. Smirnov, J. Magn. Magn. Mater. **200**, 148 (1999).
- [43] R. L. McGreevy, J. Phys.: Condens. Matter **13**, R877 (2001).
- [44] V. L. Moruzzi, *et. al.*, Phys. Rev. B **34**, 1784 (1986).

## PUBLICATIONS

### **Magnetism and phase transitions at the $\text{Cr}_2\text{O}_3$ (0001) surface**

A. L. Wysocki, Siqi Shi, and K. D. Belashchenko (to be published).

### **First-principles analysis of spin-disorder resistivity of Fe and Ni**

A. L. Wysocki, R. F. Sabirianov, M. van Schilfgaarde, and K. D. Belashchenko (submitted to Phys. Rev. B).

### **Magnetism of chromia from first-principles calculations**

Siqi Shi, A. L. Wysocki, and K. D. Belashchenko, Phys. Rev. B **79**, 104404 (2009).

### **Thermodynamics of itinerant magnets in a classical spin-fluctuation model**

A. L. Wysocki, J. K. Glasbrenner, and K. D. Belashchenko, Phys. Rev. B **78**, 184419 (2008).

### **Calculations of spin disorder resistivity from first principles**

A. L. Wysocki, K. D. Belashchenko, J. P. Velev, M. van Schilfgaarde, J. Appl. Phys. **101**, 09G506 (2007).

### **Interference effects in spin dependent transport through Aharonov-Bohm ring with quantum dots**

A. L. Wysocki, J. Barnaś, Acta Physicae Superficerum **9**, 177 (2006)